

Analysis of Photonic Crystals for Interaction with Near-Surface Emitters

VORGELEGT VON

M.Sc.

CARLO BARTH

GEB. IN DESSAU (SACHSEN-ANHALT)

VON DER FAKULTÄT IV — ELEKTROTECHNIK UND INFORMATIK
DER TECHNISCHEN UNIVERSITÄT BERLIN
ZUR ERLANGUNG DES AKADEMISCHEN GRADES

DOCTOR RERUM NATURALIUM

— DR. RER. NAT. —

GENEHMIGTE DISSERTATION

PROMOTIONS-AUSSCHUSS:

Vorsitzender: Prof. Dr. Dietmar Kissinger

Gutachter: Prof. Dr. Bernd Rech

Gutachterin: Prof. Dr. Christiane Becker

Gutachter: Prof. Dr. Oliver Benson

Tag der wissenschaftlichen Aussprache: 15. März 2018

Berlin 2018

©2017 – CARLO BARTH
ALL RIGHTS RESERVED.

ABSTRACT

The tailorable optical properties of photonic crystals enable a broad spectrum of applications beyond just the photonic bandgap. Leaky modes of photonic crystal slabs which couple to the external light field can facilitate light extraction from emitters located inside the slab or near the surface, known as the enhanced extraction effect. This effect can enhance light-emitting diodes or the output of light-emitting tags used throughout life science research and *in vitro* diagnostics. Moreover, the photonic crystal slabs can generate massively increased field energy densities. This allows for the enhancement of the emission rate of near-surface light emitters such as fluorescent dyes, molecules or quantum dots. This excitation enhancement effect makes the photonic crystal surface act as a wavelength-selective optical resonator and is widely used in the field of label-free biosensing. To design photonic crystals for applications that use excitation enhancement, the absolute increase in near-field energy must be taken into account *together* with the spatial distribution of the inducing fields. The huge parameter spaces and amounts of data that arise from these needs necessitate powerful numerical methods for the analysis and the systematic tailoring of such systems.

In this thesis numerical techniques based on simulations using a versatile and error-controlled finite element Maxwell solver are studied in view of the design and analysis of photonic crystal for the interaction with near-surface emitters. Related experiments are presented and analyzed numerically in order to explain the measured effects, also considering a novel approach of machine learning-based classification of photonic crystal mode profiles.

A numerical platform for the treatment of photonic crystals based on finite element simulations is created and optimized regarding accuracy and performance. Experimentally, the symmetry dependence of anticrossing phenomena in photonic crystal slabs, and fluorescence enhancement of lead sulfide quantum dots by excitation enhancement on a photonic crystal surface are presented. In the first experiment, the deactivation of band-anticrossing by restoring a symmetry of the system is demonstrated and traced back to the orthogonality properties of the corresponding modes. In the second experiment, the measured wavelength- and illumination direction-dependent fluorescence enhancement is compared to the numerically obtained field energy enhancement and 3D field distributions. For both experiments, a systematic analysis is conducted using a clustering technique that reduces the vast field distribution data to a minimal set of representative modes.

The set of tools that has been developed and evaluated allows for the optimization of photonic crystal slabs for virtually any application based on excitation enhancement. In biosensing, such applications are relevant for high sensitivity cancer biomarker

detection or for label-free high-resolution imaging of cells and individual nanoparticles, where the mentioned methods can be used to further increase the sensitivities. The techniques are potentially suited to systems designed for extraction enhancement, such as for light-emitting diodes, or a combination of excitation and extraction enhancement. Moreover, a proposal is made for a photonic crystal enhanced photochemical upconversion system relevant in various applications (e.g. solar energy harvesting or photodetectors).

ZUSAMMENFASSUNG

Die einstellbaren optischen Eigenschaften photonischer Kristalle ermöglichen ein breites Spektrum von Anwendungen über die photonische Bandlücke hinaus. Durch einen Effekt namens Extraktionserhöhung können Tunnelmoden (engl. *leaky modes*) photonischer Kristallmembranen, die an das externe Lichtfeld koppeln, die Lichtausbeute von Emittlern in der Membran oder auf deren Oberfläche erhöhen. Dieser Effekt kann genutzt werden um Leuchtdioden zu verbessern oder den Ertrag aus lichtemittierenden Tags zu erhöhen, welche in den Biowissenschaften und der In-vitro-Diagnostik breite Anwendung finden. Darüber hinaus können photonische Kristallmembranen enorme Erhöhungen in den Feldenergiedichten generieren. Dadurch kann die Emissionsrate oberflächennaher Lichtemitter erhöht werden, z.B. für fluoreszierende Farbstoffe, Moleküle oder Quantenpunkte. Durch diesen Anregungsverstärkungseffekt wirkt der photonische Kristall wie ein wellenlängenabhängiger optischer Resonator, weshalb er im Bereich der markierungsfreien Biosensorik häufig angewendet wird. Um photonische Kristalle für Anregungsverstärkungsanwendungen zu entwickeln, muss die absolute Erhöhung der Nahfeldenergie *und* die räumliche Verteilung der induzierenden Felder gleichermaßen berücksichtigt werden. Die riesigen Parameterräume und Datenmengen die durch diese Anforderungen entstehen, erfordern leistungsfähige numerische Methoden für die Analyse und die systematische Maßschneidung solcher Systeme.

In dieser Doktorarbeit werden numerische Verfahren für die Analyse und Entwicklung photonischer Kristalle für die Wechselwirkung mit oberflächennahen Emittlern untersucht, die auf einem vielseitigen und fehlerkontrollierten finite-Elemente Maxwelllöser basieren. Diesbezügliche Experimente werden präsentiert und durch numerische Analysen erklärt. Dabei wird auch ein neuartiger Ansatz für die Klassifizierung der Feldverteilungen photonischer Kristallmoden einbezogen, der auf maschinellem Lernen basiert.

Es wird eine numerische Plattform, basierend auf finite-Elemente Simulationen, für die Analyse photonischer Kristalle entwickelt und hinsichtlich ihrer Leistung optimiert. Experimentell wird (1) die Symmetrieabhängigkeit von Anticrossing in photonischen Kristallmembranen, und (2) die Fluoreszenzerhöhung von Bleisulfid-Quantenpunkten durch Anregungsverstärkung auf einer photonischen Kristalloberfläche behandelt. Für Experiment 1 wird das Verschwinden des Anticrossings zweier Bänder durch Symmetrisierung des Systems gezeigt und auf die Orthogonalitätseigenschaften der zugehörigen Moden zurückgeführt. Für Experiment 2 wird die gemessene wellenlängen- und beleuchtungsrichtungsabhängige Fluoreszenzerhöhung mit numerischen Feldenergieerhöhungen und 3D-Feldverteilungen verglichen. Für beide Experimente wird eine systematische Analyse durchgeführt, die durch eine

Clustering-Technik die riesigen Datenmengen der Feldverteilungen auf einen minimalen Satz repräsentativer Moden reduziert.

Die entwickelten und untersuchten Methoden erlauben die Optimierung photonischer Kristallmembranen für praktisch jede auf Anregungsverstärkung basierende Anwendung. Derartige Anwendungen sind in der Biosensorik für die Detektion von Krebs-Biomarkern mit hoher Empfindlichkeit und die markierungsfreie hochauflösende Bildgebung für Zellen und einzelne Nanopartikel relevant, wobei die genannten Methoden helfen können die Empfindlichkeiten weiter zu steigern. Die Techniken sind potentiell geeignet um Extraktionserhöhungssysteme zu verbessern, wie z.B. für Leuchtdioden, oder auch Systeme die Extraktionserhöhung und Anregungsverstärkung gleichzeitig verwenden. Außerdem wird ein konkreter Vorschlag dafür gemacht, wie photochemische Upconversion-Systeme durch photonische Kristalle verbessert werden könnten. Letztere sind relevant für eine Vielzahl von Anwendungen, unter anderem für Solarzellen und Photodetektoren.

FÜR LEVY UND YVONNE

Acknowledgments

MANY PEOPLE HAVE CONTRIBUTED IN DIFFERENT WAYS TO THIS THESIS, to whom I would like to express my gratitude in the following. First of all, I would like to thank my supervisors Prof. Dr. Christiane Becker and Prof. Dr. Bernd Rech for giving me the chance to work on this project in the Nano-SIPPE group at Helmholtz-Zentrum Berlin. Prof. Becker's continual support and the almost unlimited freedom, trust and interest really made this work possible. In the same way I thank Prof. Rech for having an open ear and great ideas whenever needed. Prof. Becker, Prof. Rech and Prof. Dr. Oliver Benson are further thanked for spending their precious time to evaluate this manuscript.

I express my gratitude to Prof. Dr. Frank Schmidt for giving me the opportunity to benefit from the expert knowledge of all members of his group at Zuse Institute Berlin and, moreover, to actually work in this fruitful environment. At ZIB, I would like to specially thank Dr. Martin Hammerschmidt for introducing me to the specifics of finite element Maxwell solvers, for being continuously open for all of my questions and for proofreading parts of the manuscript.

Besides these aspects of supervision and work environment, a number of people contributed to this thesis with actual results or measurements. Specifically, I would like to thank Dr. Grit Köppel and David Eisenhauer for photonic crystal sample fabrication using the NIL method. Dr. Florian Ruske and David Eisenhauer for investigations on surface thicknesses and roughnesses using ellipsometry. Prof. Dr. Christiane Becker and Dr. Klaus Jäger for performing ARR measurements. Sebastian Roder for performing the actual fluorescence enhancement measurements. Dr. Martin Hammerschmidt for performing the reduced basis optimization for the geometrical parameters of the fluorescence enhancement experiment sample. Carola Klimm for providing beautiful SEM images. Prof. Dr. Tobias Kraus and many members of his group at INM Saarbrücken, including Daniel Brodoceanu, Sebastian Beck and Robert Strahl, and furthermore Bruno Schäfer of INM, for quantum dot coating of the photonic crystal samples and characterizations using various techniques, including SEM, UV/Vis and ellipsometry.

All of the colleagues mentioned so far are moreover deeply thanked for countless invaluable discussions, which also applies to Prof. Kazuaki Sakoda, Jürgen Probst, Dr. Sven Burger, Dr. Lin Zschiedrich, Dr. Jan Pomplun, Dr. Daniel Lockau, Sven Herrmann, Philipp Gutsche, Dr. Jolly Xavier and Dr. Rowan MacQueen. Moreover, I would like to thank Dr. Phillip Manley for proofreading parts of the manuscript pertaining

to the English language.

I acknowledge funding provided by the German Federal Ministry of Education and Research within the program NanoMatFutur (No. 03X5520) the Einstein Foundation Berlin through ECMath within subproject OT9. Parts of the results have been obtained in the scope of the Berlin Joint Lab for Optical Simulations for Energy Research (BerOSE) of HZB, ZIB and Freie Universität Berlin.

I would like to thank the developers of the Scikit-learn Python library for providing a state-of-the-art, open-source and solid implementation of machine learning algorithms, without which the clustering results of this work would not have been obtained. The same holds for the active users and developers at news.povray.org, who guided me on the way to achieve a high quality animation of excitation enhancement using actual physical data.

Finally, I would like to thank the members of my family who supported me all these years, no matter which path I walked. Specifically, I cannot express the gratitude I feel for the support, love and patience that Yvonne found for me — *but I think you know*. We went through a wonderful, but hard time. Thank you Levy for making me laugh, and cry; for letting me finish this project although *you* deserve all of my attention; — and for being the first miracle I have ever laid eyes on.

Contents

1	INTRODUCTION	1
2	THEORY AND FUNDAMENTALS	7
2.1	Time-harmonic electromagnetics	7
2.1.1	The electromagnetic scattering problem	9
2.1.2	Derivation of the essential quantities	10
2.2	Photonic crystal slabs	12
2.2.1	The wave equation as an eigenvalue problem	14
2.2.2	Symmetries, point groups and the classification of modes	15
2.2.3	Continuous translational symmetry	16
2.2.4	Discrete symmetries, Bloch's theorem and the Brillouin zone	18
2.2.5	2D photonic crystals with hexagonal lattice	19
2.2.6	Photonic crystal slabs and leaky modes	22
2.2.7	Interaction with emitters	26
2.3	Aspects of machine learning	28
2.3.1	Introduction and motivation	28
2.3.2	Mathematical notation and general problem set	31
2.3.3	Supervised learning, unsupervised learning and clustering	31
2.3.4	k -means clustering	32
2.3.5	Clustering using Gaussian mixture models	33
2.3.6	Real-world scenarios	35
3	METHODS AND MATERIALS	39
3.1	Finite element method for the treatment of photonic crystals	40
3.1.1	Computational photonics in a nutshell	40
3.1.2	Basic principles	42
3.1.3	Boundary conditions	44
3.1.4	Error characterization	45
3.1.5	Adaptive techniques	46
3.1.6	Notes on 2D and 3D meshing	47
3.2	The nanohole array	47
3.2.1	System geometry and parameters	48
3.2.2	Meshing	50
3.2.3	Illumination using plane waves	51
3.2.4	Considered physical quantities	51

3.3	Properties of involved materials	54
3.3.1	Notes on the material assignment in simulations	54
3.3.2	Optical properties of dielectrics and their interpolation	55
3.3.3	Lead sulfide quantum dots	56
3.4	Experimental techniques	58
3.4.1	Angular- and wavelength resolved reflectance measurements	59
3.4.2	Measurement of fluorescence enhancement	60
3.5	Fabrication using nanoimprint lithography	61
4	CONVERGENCE AND PERFORMANCE OF FINITE ELEMENT SIMULATIONS	65
4.1	Notes on terminology	66
4.2	Fresnel refraction	67
4.2.1	Analytical solutions	67
4.2.2	Simulation setup, mesh parameters and quantity calculation	68
4.2.3	Convergence analysis	69
4.3	Mie scattering	71
4.3.1	Analytical solutions	72
4.3.2	Mesh parameters and numerical quantity calculation	73
4.3.3	Convergence analysis	75
4.3.4	Performance optimization	77
4.4	Nanohole array	78
4.4.1	System geometry, mesh parameters and quantities	79
4.4.2	Convergence analysis	81
4.4.3	Performance optimization	83
4.4.4	Verifying the convergence on a narrow peak	83
5	DISCOVERING SYMMETRY DEPENDENCE IN ANTICROSSING PHENOMENA	87
5.1	Background and guide to relevant sections	88
5.2	Sample design and numerical model	88
5.3	Reflectance and field energy enhancement analysis	90
5.4	Analysis of field distributions	91
5.5	Discussion	92
6	INCREASED FLUORESCENCE OF PBS QUANTUM DOTS	95
6.1	Sample geometry and quantum dot coating	96
6.2	Reflectance properties of the uncoated sample	97
6.3	Measured fluorescence enhancement	99
6.4	Numerical model for the coated photonic crystal	101
6.5	Comparison to numerical field energy enhancement maps	101
6.6	Selected field distributions and Q-factors	102
6.7	Discussion	103

7	CLASSIFICATION OF FIELD DISTRIBUTIONS USING MACHINE LEARNING	107
7.1	Justification of mode clustering	108
7.2	Clustering for the anticrossing experiment	109
7.2.1	Constructing the clustering data	110
7.2.2	Learning the field patterns for the symmetric case	110
7.2.3	Mode classification	111
7.2.4	Measuring the quality of the class assignments	112
7.3	Discussion (part 1)	113
7.3.1	Validating the clustering model	114
7.3.2	Cluster centers: the field pattern prototypes	116
7.4	Clustering for the fluorescence enhancement experiment	117
7.4.1	Specifics of the clustering procedure	117
7.4.2	Classification maps and silhouette analysis	119
7.4.3	Cluster centers	120
7.5	Discussion (part 2)	125
7.5.1	Systematic analysis of the clustering results	126
7.5.2	Summary and evaluation of the analysis method	129
8	CONCLUSION AND OUTLOOK	133
	OWN CONTRIBUTIONS	139
	Peer-reviewed articles	139
	Contributed talks	139
	Poster presentations	140
	Own master and bachelor theses and related publications	140
	Supervised master theses	140
	REFERENCES	140
	LIST OF FIGURES	151
	LIST OF ACRONYMS	153

1

Introduction

There are these two young fish swimming along and they happen to meet an older fish swimming the other way, who nods at them and says, “Morning boys. How’s the water?” And the two young fish swim on for a bit, and then eventually one of them looks over at the other and goes, “What the hell is water?”

— David Foster Wallace —

WHEN DAVID FOSTER WALLACE began his famous commencement speech at Kenyon College in 2005 with the story above, he wanted to stress a quite simple, yet essential fact about human life: — in his own words, “that the most obvious, ubiquitous, important realities are often the ones that are hardest to see [...]” These important realities, here represented by the water, are nothing less than the *foundation* of the fish’s lives; and overlooking them might be considered as careless, or even dangerous.

In fact, a point Wallace probably did not think of is that these fish could easily be affected by *changing* these realities. Let us rephrase Wallace’ little story with a minimum set of replacements, so that it reads:

There are these two young quantum dots shining along and they happen to meet an older quantum dot shining the other way, who nods at them and says, “Morning boys. How’s the light field?” And the two young quantum dots shine on for a bit, and then eventually one of them looks over at the other and goes, “What the hell is a light field?”

By doing so, the parable-ish story did not lose its figurative sense, — assuming the reader has a notion of what quantum dots are. But it now (surprisingly) communicates another, more physical meaning: suppose quantum dots, i.e. single two-level emitters, are stimulated by a surrounding light field to emit photons. The quantum dots may be

completely agnostic about the ambient light, just as the two fish are about the water. However the bottom line is: the only thing that really matters for the intensity of their emission is the strength of exactly this light field.

A clever scientist might now argue that this is a rather simple matter: if the emission of the quantum dots should be increased, why not just turn up the power of the light source? But what if we aim at an application for which the light source is fixed, such as in the case of sunlight? Or if we consider a portable, battery-driven system, that should consume as little energy as possible. In such cases, the light field can still be increased locally, — using *photonic crystals*. These periodic dielectric structures enable the tailoring of the optical properties of materials, and therefore the ability to affect the light field in the desired way [1, 2].

Suppose one of the two fish swims through a canyon and, without him noticing, the canyon narrows, causing the current to accelerate. Cold water from a nearby reservoir might cause additional turbulences and temperature fluctuations; — suddenly the fish is in a confusing situation that might make him easy prey. Although we did not change the *amount* of water in the sea in this fictitious situation, the *distribution* and the dynamics have been changed by the surroundings. In a similar way photonic crystals can exhibit resonances that accumulate light energy in specific volumes, either “inside” the photonic crystal itself, or on its surface. The latter is true in the case of *photonic crystal slabs*, which are quasi-2D photonic crystals composed of a thin nanotextured membrane. In consequence, it is possible to design photonic crystal slabs in a way that specific resonances can interact with *near-surface emitters*, such as quantum dots, atoms or molecules.

Photonic crystal slabs are comparatively easy to manufacture and offer a large number of possible applications. For example, the photonic band gap effect enables resonators [3] or waveguides [4, 5] to be built by introducing specific defects into the periodic lattice. Furthermore, photonic crystal lasers [6] and systems for quantum computing [7] have been proposed or even realized. However, photonic crystal slabs also exhibit a phenomenon called *leaky modes*, which are resonances that can be excited using external radiation (see e.g. [8–12]). These characteristics have been used to improve various applications (e.g. light trapping [13] and light-emitting diodes (LEDs) [14, 15]), but can also be utilized for affecting emitters, or more specifically fluorescent species. Especially in the life-sciences, the applications range from photonic crystal enhanced microscopy and single molecule detection to enhanced live cell imaging, DNA sequencing and gene expression analysis [16–19].

Principally, two mechanisms can increase the light yield of emitters on the surface of a photonic crystal slab: *extraction enhancement* and *excitation enhancement*. For extraction enhancement, leaky modes of the photonic crystal provide channels to improve the outcoupling of fluorescent light [9–11, 14, 21–26]. In contrast, excitation enhancement directly affects the stimulated emission rate of the emitters. This can be done

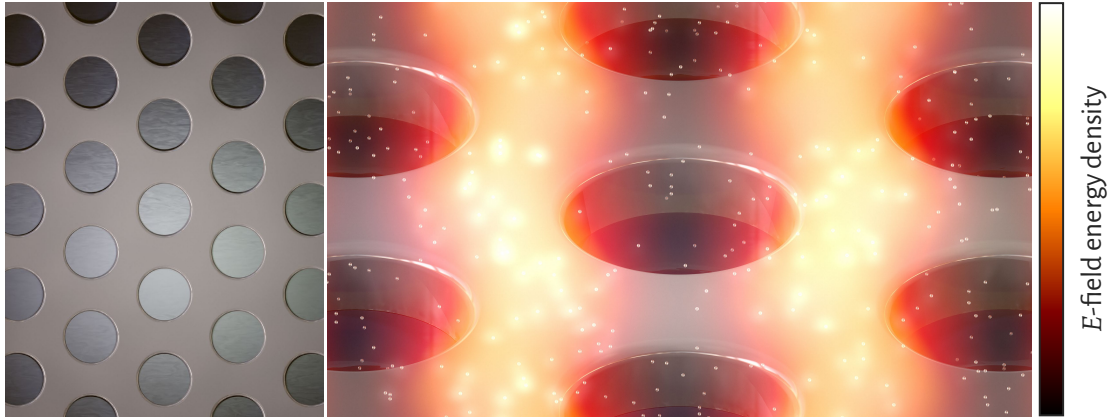


Figure 1: Artistic illustration of excitation enhancement. A photonic crystal slab with hexagonal lattice (left: top view of the structure only) is shown together with an actual computed field energy distribution, which is volume rendered with a heat color map. Emitters are depicted as semitransparent spheres with a glowing aura proportional to the field energy density at their respective positions. The figures were generated using a ray tracing software (POV-Ray [20]).

by utilizing leaky modes in the absorption wavelength range of the emitters that possess increased near-field energy densities [27], for instance. Figure 1 shows an artistic illustration of the excitation enhancement process. An actual simulated field energy distribution of the photonic crystal slab with hexagonal lattice is shown using a volume render with a heat color map. A random distribution of emitters is depicted by small spheres which have a glowing effect with an intensity proportional to their position in the field.

Generally, extraction enhancement is a well-investigated phenomenon and has been demonstrated for nitrogen-vacancy centers in diamond[25], DNA microarrays [17], molecules [22, 28] and quantum dots [23, 26, 29, 30]. Inducing extraction enhancement using photonic crystals, specifically, has been shown several times either, both for intrinsic fluorescence of the photonic crystal itself [24, 25] and for quantum dots embedded into the photonic crystal [22, 26] or on its surface [23]. Compared to the amount of investigations and demonstrated applications related to extraction enhancement, excitation enhancement is a rather unexplored field. A comparable effect has been used to increase the efficiency of quantum dot solar cells [31, 32] and the quantum yield of up-conversion devices [33–35]. However, considering emitters on a photonic crystal surface, excitation enhancement effects have been rarely demonstrated (e.g. in [18, 30]), but in combination with extraction enhancement. Moreover, these publications did not systematically investigate the excitation enhancement properties as a function of the incident radiation conditions, but rather for a single photonic crystal mode.

FOR THAT REASON, THE MAIN FOCUS OF THIS THESIS is to explore techniques for the design of photonic crystal slabs for the interaction with near-surface emitters by means of excitation enhancement. This will involve creating a set of tools which can be used to specifically design a system to increase the light yield of the emitters of choice. Such a tool has many applications, e.g. highly-sensitive biosensors. A portable sensor is conceivable which could detect a very specific molecule, — perhaps a cancer indicator, using an integrated low-power laser source. The techniques developed here should enable the system designer to determine the optimum geometrical parameters of a photonic crystal slab using an all-numerical approach, — based on the final known distribution of the target emitters and their absorption and emission properties only. In addition, the same techniques should facilitate the understanding of actual measurements performed in the development stage.

However, the presented investigations are not concerned with a specific application, but rather kept as general as possible. Quantum dots have been chosen as example emitters, because they are much simpler in their absorption and emission characteristics compared to biomolecules. They are moreover readily available with custom emission wavelength ranges. But the task stated above is complex, since a large number of parameters has to be considered. In a simplified view the design task comes down to these two steps:

1. Find a photonic crystal mode that has (a) the highest possible energy density, while having (b) an optimum field distribution under consideration of the spatial arrangement of the emitters.
2. Tweak the geometrical parameters of the photonic crystal to exhibit this mode at the desired wavelength.

From these steps, the second one is rather simple, supposing the wavelength of the identified mode is not too far from the target wavelength. It is merely a question of scanning over a finite set of geometrical parameters, such as the lattice constant or slab thickness [1]. For part (a) of step 1 a similar reasoning can be applied, and it has already been demonstrated that modes with largely enhanced fields can effectively be found using finite-element method simulations [27]. Moreover, the maximum possible increase in field strength is not unlimited if the line width of the excitation source is limited, as it is correlated to the band width (or rather the Q-factor) of the corresponding leaky mode. Just as it was demonstrated in [27], the determination of the integrated field enhancement must be restricted to the volume in which the emitters are supposed to be, preferring modes that exhibit strong fields in this volume.

Consequently, the crucial part in the steps given above is 1.(b), as it enforces effectively considering the 3D field distributions of all the potential photonic crystal resonances. This is a large parameter space, and reducing it to a feasible size necessitates the consideration of theoretical background knowledge on the expected behavior of

the modes, *and* powerful numerical evaluation techniques at the same time. As a standard method in computational photonics, the finite element method (FEM) was used throughout this thesis. Powerful libraries and commercial solvers that implement the FEM are readily available. These sophisticated solvers can deal with complex geometries and material properties, and they offer a large collection of post-processing and evaluation tools to determine the physical quantities of interest. The tasks above introduce the challenges of analyzing vast parameter spaces, caused by the geometrical and illumination condition parameters, and handling huge amounts of field distribution data. For the former challenge, an in-depth convergence study is used to optimize the FEM solver in view of performance, while assuring an adequate accuracy. In order to evaluate the thousands of field distributions a new approach is investigated in the scope of this thesis: the classification of photonic crystal modes using *machine learning*.

Machine learning is itself a rapidly evolving discipline which is being applied to all aspects of science and everyday-life, from medicine and economics to online security and insurance. In the field of photonic crystals specifically, machine learning strategies have not been explored widely, except for concepts of so-called inverse or computational design [36–40], which use algorithms to optimize the geometry of the systems for specific tasks (e.g. genetic algorithms). These concepts could in principle also be applied to solve tasks 1.(a) and 2. from above.

The novel approach in the present work was to use so-called *clustering* algorithms to reduce the large amount of field distribution data to a minimal set of typical distributions. This classification task was applied to two experiments which were published without the machine learning analysis, namely **(i)** the demonstration of symmetry dependence of anticrossing phenomena [41], and **(ii)** the increased fluorescence of quantum dots on a photonic crystal surface [42] indicated above. Experiment (i) shows fundamental effects which are directly related to symmetry properties of the photonic crystal modes. Since the theoretical assumptions that are supported using this experiment are crucial for the justification of the clustering approach, it can be seen as a “benchmark case”. The more complex issues of experiment (ii), which correspond to task 1.(b), are finally tackled using the same machine learning-based approach and widely explain the observed phenomena.

IN ORDER TO PRESENT THE INVESTIGATIONS related to the objectives discussed above, the thesis is organized in the following way. **Chapter 2** discusses the theoretical aspects of photonic crystal slabs after a brief consideration of the underlying physics from electromagnetics. Rather than giving a complete introduction to photonic crystals, the focus is on two different aspects: first, the origin of leaky modes and their application to emission enhancement of near-surface emitters; and second, the expected spatial properties of the photonic crystal modes that can be derived from fundamental

symmetry considerations. The latter is moreover a crucial point for the justification of the clustering approach, which is finally discussed in a detailed theoretical (and partly practical) introduction to the machine learning techniques in question. Afterwards, **chapter 3** deals with the numerical and experimental techniques relevant for the mentioned experiments, and gives information on the geometrical and material-specific properties of the related systems. It furthermore covers aspects of the fabrication process of the photonic crystals. As a “transitional” chapter between the methodical and the results-specific parts, **chapter 4** elaborates in detail on how the convergence of the FEM simulations has been guaranteed. The three subsequent chapters treat the results and related discussion of the experiments, as well as the corresponding numerical investigations outlined above. More precisely, in **chapters 5 and 6** the experiments (i) and (ii) are presented together with the first part of the numerical analysis, while **chapter 7** features the machine learning-based investigation of the same experiments. The thesis closes with a retrospective view on which of the initial objectives presented here were actually met, in **chapter 8**, and a collection of ideas of how to further develop the techniques and considered system designs.

“The formulation of the problem is often more essential than its solution, which may be merely a matter of mathematical or experimental skill.”

— ALBERT EINSTEIN —

2

Theory and Fundamentals

THE THEORETICAL FUNDAMENTALS that underlie the presented material spread across quite different disciplines: from standard electromagnetics and photonic crystals, to interaction of the latter with emitters and machine learning. As typical for a work with a focus on computational physics, the material is on the edge between theory and experiment; often trying to explain experimental results with the help of theoretical equations that are solved numerically. It is thus necessary to keep the treatise short wherever possible, while assuring that everything beyond “common knowledge” is explained – which in this case is basically everything related to photonics.

Based on these assumptions, the presentation of the electromagnetics, as well as the introduction of photonic crystals (PhCs), is concise. The focus is on the specific details that are relevant to understand the methods and results. An exception hereof is the part on symmetry of PhCs, as it is of specific relevance to legitimate the application of the methods based on machine learning.

Furthermore, the machine learning part is another exception, as it is a rather uncommon technique in the field of photonics. Therefore, an introduction using a simple example and a motivation for the application in this thesis is put in front of the actual theoretical treatment. The example will be consulted frequently to assist the comprehension of the rather condensed fundamentals.

2.1 Time-harmonic electromagnetics

The principle theoretical description of photonic crystals is based on the Maxwell equations, i.e. the fundamental theory of electromagnetism. However, since all problems studied in this work belong to the class of electromagnetic scattering problems on dielectric objects, a number of simplifications can be applied and the treatment can be

restricted to time-harmonic fields. The general (point form) Maxwell equations can be stated as [43]

$$\nabla \cdot \mathbf{B} = 0, \quad \nabla \cdot \mathbf{D} = \rho, \quad \nabla \times \mathbf{E} + \frac{\partial \mathbf{B}}{\partial t} = 0, \quad \nabla \times \mathbf{H} - \frac{\partial \mathbf{D}}{\partial t} = \mathbf{J}, \quad (2.1)$$

with \mathbf{E} and \mathbf{H} being the electric and magnetic fields, \mathbf{D} and \mathbf{B} the electric and magnetic flux densities, respectively, and \mathbf{J} the electric current density. It is assumed that the electromagnetic solution fields exhibit a harmonic time dependence, i.e.

$$\widehat{\mathbf{E}}(\mathbf{r}, t) = \widehat{\mathbf{E}}_0(\mathbf{r})e^{-i\omega t}, \quad (2.2)$$

$$\widehat{\mathbf{H}}(\mathbf{r}, t) = \widehat{\mathbf{H}}_0(\mathbf{r})e^{-i\omega t}, \quad (2.3)$$

where hats denote complex-valued fields and ω is the angular frequency. The physical fields are recovered from these fields by taking the real part, as usual, so that the hat notation will only be used to avoid ambiguities from now on. Moreover, it is assumed that in most cases a time average of the form

$$\bar{A}(t) = \frac{1}{\tau} \int_t^{t+\tau} A(t') dt', \quad (2.4)$$

over a characteristic period $\tau = 2\pi/\omega$ is required. Using the time-harmonic ansatz the time derivatives in the Maxwell equations (2.1) can be executed, obtaining the time-harmonic Maxwell equations

$$\nabla \cdot \mathbf{B} = 0, \quad \nabla \cdot \mathbf{D} = \rho, \quad \nabla \times \mathbf{E} - i\omega \mathbf{B} = 0, \quad \nabla \times \mathbf{H} + i\omega \mathbf{D} = \mathbf{J}. \quad (2.5)$$

Flux densities and fields are connected via the material equations

$$\mathbf{D}(\mathbf{r}, t) = \epsilon_0 \mathbf{E}(\mathbf{r}, t) + \mathbf{P}(\mathbf{r}, t), \quad (2.6)$$

$$\mathbf{B}(\mathbf{r}, t) = \mu_0 \mathbf{H}(\mathbf{r}, t) + \mathbf{M}(\mathbf{r}, t), \quad (2.7)$$

with the free-space permittivity $\epsilon_0 \approx 8.854 \cdot 10^{-12} \text{ F m}^{-1}$ and free-space permeability $\mu_0 = 4\pi \cdot 10^{-7} \text{ H m}^{-1}$, connected to the speed of light in vacuum via $c_0 = (\epsilon_0 \mu_0)^{-1/2}$. We can further define the vacuum impedance

$$Z_0 = \sqrt{\frac{\mu_0}{\epsilon_0}} \approx 376.7303 \Omega. \quad (2.8)$$

The vector functions $\mathbf{P}(\mathbf{r}, t)$ and $\mathbf{M}(\mathbf{r}, t)$ in equations (2.6) and (2.7) are the polarization and magnetization of the material, respectively. The treatment is further restricted to

linear materials, where these functions can be represented by linear-response expressions

$$\mathbf{P}(\mathbf{r}, t) = \epsilon_0 \int_0^\infty \chi_e(\mathbf{r}, \tau) \mathbf{E}(\mathbf{r}, t - \tau) d\tau, \quad (2.9)$$

$$\mathbf{M}(\mathbf{r}, t) = \mu_0 \int_0^\infty \chi_m(\mathbf{r}, \tau) \mathbf{H}(\mathbf{r}, t - \tau) d\tau \quad (2.10)$$

with the electric and magnetic susceptibilities χ_e and χ_m . In many cases this is further simplified by considering nondispersive materials, yielding material equations in the form of

$$\mathbf{D}(\mathbf{r}, t) = \epsilon_0 \epsilon(\mathbf{r}) \mathbf{E}(\mathbf{r}, t), \quad (2.11)$$

$$\mathbf{B}(\mathbf{r}, t) = \mu_0 \mu(\mathbf{r}) \mathbf{H}(\mathbf{r}, t). \quad (2.12)$$

Here, the relative permittivity $\epsilon(\mathbf{r})$ and relative permeability $\mu(\mathbf{r})$ have been introduced, which are scalar functions in the case of isotropic materials. One can further define the often considered refractive index $n = \sqrt{\mu\epsilon}$ from these functions.

2.1.1 The electromagnetic scattering problem

Using Fourier transformations the time dependence in the electric and magnetic fields can be replaced by a frequency dependence, i.e. $\mathbf{E}(\mathbf{r}, t) \rightarrow \mathbf{E}(\mathbf{r}, \omega)$ and $\mathbf{H}(\mathbf{r}, t) \rightarrow \mathbf{H}(\mathbf{r}, \omega)$, known as frequency domain. Especially when considering numerical methods for solving the Maxwell equations, it is often useful to derive a wave equation which only depends on one of the fields, \mathbf{E} or \mathbf{H} .

The exclusive type of problem considered in this thesis is the *scattering problem*, which is the interaction of an incident electromagnetic field with a scatterer located within an area of interest located away from any source currents. Here, we usually deal with non-magnetic, dielectric, dispersive materials for which the permeability is unity $\mu(\mathbf{r}, \omega) = 1$, but the permittivity may have spatial and spectral dependence $\epsilon = \epsilon(\mathbf{r}, \omega)$. For this case (and slowly varying ϵ) the wave equations can be written as [44]

$$\nabla^2 \mathbf{E}(\mathbf{r}, \omega) + \epsilon(\mathbf{r}, \omega) k_0^2 \mathbf{E}(\mathbf{r}, \omega) = 0, \quad (2.13)$$

$$\nabla^2 \mathbf{H}(\mathbf{r}, \omega) + \epsilon(\mathbf{r}, \omega) k_0^2 \mathbf{H}(\mathbf{r}, \omega) = 0, \quad (2.14)$$

where $k_0 = \omega/c_0$ is the wave number in vacuum. The most important simplification for the case of finite element simulations is to further consider homogenous media, for which the material functions have no spatial dependence ($\mu \neq 1$ is included here for generality). This case is important because, as will be shown later, these simulations utilize a piecewise constant ϵ (and μ) referred to as patches, so that the wave equations can further be reduced to the Helmholtz equations

$$\nabla^2 \mathbf{E}(\mathbf{r}) + k_0^2 \mu \epsilon \mathbf{E}(\mathbf{r}) = 0, \quad (2.15)$$

$$\nabla^2 \mathbf{H}(\mathbf{r}) + k_0^2 \mu \epsilon \mathbf{H}(\mathbf{r}) = 0. \quad (2.16)$$

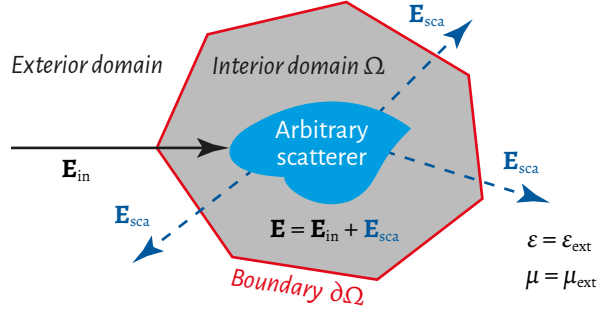


Figure 2: Illustration of the electromagnetic scattering problem. An electromagnetic field \mathbf{E}_{in} incident from the exterior domain interacts with an arbitrary scatterer, which is entirely inside the interior domain Ω with boundary $\partial\Omega$. The total field \mathbf{E} results from the superposition of \mathbf{E}_{in} and the scattered field \mathbf{E}_{sca} , which radiates away from the scatterer. The permittivity ϵ and permeability μ have constant, scalar values ϵ_{ext} and μ_{ext} in the exterior domain.

A severe mathematical description of the scattering problem will be omitted here, but can be found in many places, such as textbooks [44], journal articles [45] and theses [46, 47]. The main idea, however, is to divide the problem into an infinite, homogeneous exterior domain with constant permittivity ϵ_{ext} and permeability μ_{ext} ; and a finite interior domain Ω surrounding the scatterer; a sketch of this situation is depicted in figure 2. All sources are located in the exterior domain, so that an incident field (e.g. in the electric case) \mathbf{E}_{in} enters the interior domain at the boundary of Ω . The interaction of \mathbf{E}_{in} with the scatterer generates a scattered field \mathbf{E}_{sca} which is therefore strictly outgoing. The total field is then simply the superposition of the partial fields $\mathbf{E} = \mathbf{E}_{\text{in}} + \mathbf{E}_{\text{sca}}$. Loosely speaking, the problem is then defined by demanding that the partial fields satisfy the Maxwell equations together with appropriate boundary conditions; most prominently the Silver-Müller radiation condition, stating that the scattered field is asymptotically approaching a transversal plane wave traveling radially away from the scatterer. This is known as Maxwell's scattering problem, and it can similarly be described for the Helmholtz-equations [44].

2.1.2 Derivation of the essential quantities

After having introduced the underlying equations and formulated the general problem, a few quantities which are essential for the description of the considered systems and their analysis in later chapters will be derived.

As before, the treatment is restricted to time-harmonic fields (2.2) and (2.3). One is often interested in the energy which the electromagnetic field, or only one of the two parts, holds in a specific volume. This can be obtained from a volume integral over the electromagnetic energy density

$$\bar{w}(\mathbf{r}) = \frac{1}{4} \Re (\mathbf{H}_0 \cdot \mathbf{B}_0^* + \mathbf{E}_0 \cdot \mathbf{D}_0^*), \quad (2.17)$$

or over one of the electric and magnetic parts of the energy density

$$\bar{w}_e(\mathbf{r}) = \frac{1}{4} \Re(\mathbf{E}_0 \cdot \mathbf{D}_0^*), \quad (2.18)$$

$$\bar{w}_m(\mathbf{r}) = \frac{1}{4} \Re(\mathbf{H}_0 \cdot \mathbf{B}_0^*), \quad (2.19)$$

respectively. Here, the bar denotes the time average, which is of interest in the time harmonic case. For scattering problems it can also be of interest how much energy flows from one domain into another, i.e. the energy flux. This can be derived from a surface integral of the energy flux density, given by the Poynting vector. In the general form the Poynting vector is defined as

$$\mathbf{S}(\mathbf{r}, t) = \mathbf{E}(\mathbf{r}, t) \times \mathbf{H}(\mathbf{r}, t), \quad (2.20)$$

or for the time average

$$\bar{\mathbf{S}}(\mathbf{r}) = \frac{1}{2} \Re(\mathbf{E} \times \mathbf{H}^*). \quad (2.21)$$

For the special case of plane waves defined by

$$\begin{aligned} \mathbf{E}(\mathbf{r}, t) &= \mathbf{E}_0 e^{i(\mathbf{k} \cdot \mathbf{r} - \omega t)}, \\ \mathbf{B}(\mathbf{r}, t) &= \mathbf{B}_0 e^{i(\mathbf{k} \cdot \mathbf{r} - \omega t)}, \end{aligned}$$

the electric and magnetic fractions of the energy density are equal, so that the magnetic field can be eliminated from the time averaged Poynting vector, yielding [48]

$$\bar{\mathbf{S}}(\mathbf{r}) = \frac{1}{2} \sqrt{\frac{\epsilon \epsilon_0}{\mu \mu_0}} |\mathbf{E}_0|^2 \frac{\mathbf{k}}{k}. \quad (2.22)$$

When dealing with complex-valued permittivity functions, a fraction of the electromagnetic energy may be absorbed in the medium. Consequently, when optimizing optical systems in view of efficiency it is often the task to minimize absorption effects, necessitating to calculate the absorption in a specific volume. In order to derive this quantity, the work rate by an electric field $\mathbf{E}(\mathbf{r})$ on a static current distribution $\mathbf{J}(\mathbf{r})$ in a volume V [43] is considered, given by

$$\frac{dW}{dt} = \int_V \mathbf{J} \cdot \mathbf{E} dV.$$

Assuming time harmonic fields and substituting the expression for \mathbf{J} from the Maxwell equations (2.5), one can obtain the integral representation of Poynting's theorem on the conservation of energy

$$\frac{1}{2} \int_V \mathbf{J}^* \cdot \mathbf{E} dV = \frac{1}{2} \int_V [-\nabla \cdot (\mathbf{E} \times \mathbf{H}^*)] dV + \frac{1}{2} \int_V [-i\omega (\mathbf{H} \cdot \mathbf{B}^* + \mathbf{E} \cdot \mathbf{D}^*)] dV, \quad (2.23)$$

where the vector identity $\nabla \cdot (\mathbf{U} \times \mathbf{V}) = \mathbf{V} \cdot (\nabla \times \mathbf{U}) - \mathbf{U} \cdot (\nabla \times \mathbf{V})$ was used. Substituting the Poynting vector (2.21) and (complex forms of) the electric and magnetic energy densities (2.18) and (2.19) in equation (2.23), we finally obtain (compare [43])

$$0 = \frac{1}{2} \int_V \mathbf{J}^* \cdot \mathbf{E} \, dV + 2i\omega \int_V (w_e - w_m) \, dV + \int_{\partial V} \bar{\mathbf{S}} \cdot \mathbf{n} \, d\mathbf{f} \quad (2.24)$$

with ∂V being the surface enclosing V , \mathbf{n} the surface normal and $d\mathbf{f}$ the surface element. For scattering simulations the first addend in equation (2.24) vanishes, because all sources are in the exterior domain by definition. When applying Stokes' theorem to the surface integral and taking the real part on both sides to gain the physical energy conservation, we find

$$\int_V \nabla \cdot \bar{\mathbf{S}} \, dV = -2\omega \int_V [\Im(w_e) - \Im(w_m)] \, dV.$$

The left side is essentially a volume integral over the divergence of the Poynting vector, i.e. over sources/sinks of the energy flux density. This means that, if the right side is positive, its value is the net energy loss in the volume V , giving a definition for the absorption in volume V

$$A_V := -2\omega \int_V [\Im(w_e) - \Im(w_m)] \, dV \quad (2.25)$$

or alternatively for non-magnetic materials

$$A_V = -2\omega \Im(\widehat{W}_e^V), \quad (2.26)$$

where $\widehat{W}_e^V = \int_V w_e \, dV$ denotes the total, complex-valued electric energy in volume V . It is further recognized that the absorption is indeed caused by the imaginary parts of the energy densities only, and may thus exclusively occur for materials with $\Im(\epsilon) \neq 0$ and (or) $\Im(\mu) \neq 0$.

2.2 Photonic crystal slabs

PhCs are dielectric structures with a spatially periodic permittivity, usually on scales comparable to the wavelength of the incident light. They are, therefore, the generalization of the multi-layer stack that was first described by Lord Rayleigh in 1887 [49], which is effectively a 1D PhC. The idea for the extension to two and three dimensions, however, took 100 years – when Yablonovitch and John both published according material in 1987 [50, 51]. Until then, PhCs have been intensely studied, so that the fundamentals have appeared in a large number of textbooks, e.g. the excellent introduction given by Joannopoulos *et al.* [1].

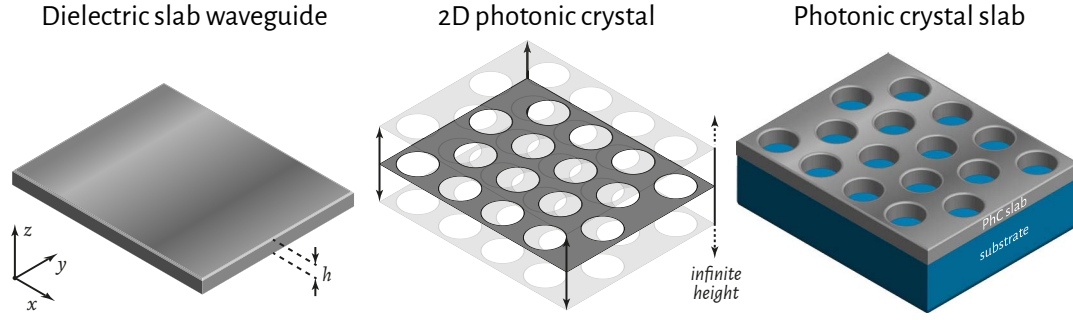


Figure 3: Sketch of a photonic crystal slab and the two limiting cases: the dielectric slab waveguide and the 2D photonic crystal. (Left) The dielectric slab waveguide, i.e. a dielectric membrane of thickness h . **(Center)** The 2D photonic crystal counterpart of the photonic crystal slab, with infinite extension in z -direction. **(Right)** The photonic crystal slab with hexagonal lattice and an optional substrate. All systems are considered as infinite in x - and y -direction.

In the theoretical treatise given here, the focus is on PhC slabs and their treatment by means of symmetries. PhC slabs are essentially a mixture of a 2D PhC and a dielectric waveguide, that is to say thin dielectric membranes with a 2D-periodic patterning, optionally having additional substrates or coatings. Just as before, *thin* means comparable to the related wavelength scale. The aspects of interest here are the mode properties of specific PhC slabs, especially in the case of external radiation. There are basically two objectives in this section: (1) to justify the application of the machine learning-based classification of modes presented in chapter 7, which necessitates to consider conclusions that basically follow from a group-theoretical treatment of the symmetry properties of PhC modes. And (2), to derive the properties of leaky modes, which are the essential feature for the experiments and numerical results of the results chapters 5 and 6. The presented material is almost exclusively derived from the book by Joannopoulos *et al.* [1] mentioned above and the book by Sakoda [2], where the latter focusses on symmetry. Additional sources are cited where needed. The essential terms and concepts are introduced as implications of the symmetric surroundings affecting the solutions to the Maxwell equations, or rather the wave equations.

The actual physical system of interest – the nanohole array – will be described rigorously in section 3.2. Until then, it is considered more generally as a PhC slab with thickness h and a hexagonal lattice of cylindrical holes with radius r . As a convention, the plane of periodicity is considered the xy -plane, while the finite thickness of the slab is in z -direction. Figure 3 shows a sketch of this PhC slab with an optional substrate at right hand side. This system can be seen as a special case of the respective 2D system with infinite extension in z -direction (center sketch in figure 3), i.e. 2D being the case of $h \rightarrow \infty$. A second special case is the (unpatterned) dielectric slab waveguide, i.e. for $r \rightarrow 0$ (left sketch in figure 3). Both of these simple cases are discussed first to introduce the concepts that can partly be applied to the patterned slab.

Afterwards, the PhC slab with hexagonal lattice is treated and the differences from the limiting cases are discussed. The restrictions that arise from the discrete symmetry in the slab plane are studied, followed by a discussion of the separation of modes in two orthogonal polarizations. After that, the most important aspect of PhC slabs is considered: the leaky modes. It is shown that leaky modes alter the reflection and transmission properties of the system and can generate highly increased energy densities close to the surface. Finally, it is discussed how leaky modes can interact with near-surface emitters. Therefore, the two prominent mechanisms enhanced extraction and enhanced emission are explained.

2.2.1 The wave equation as an eigenvalue problem

PhCs can be treated in much the same fashion as electronic crystals (see e.g. [52]), and many of the approaches are in fact identical to those in solid-state physics. We therefore begin by deriving an eigenvalue equation comparable to the one of quantum mechanics, where the Hamiltonian acts on the wave function.

As PhCs are dielectrics, we restrict the treatment to nonmagnetic materials with $\boldsymbol{\mu}(\mathbf{r}, \omega) = 1$. The wave equations in frequency domain have already been given in equations (2.13) and (2.14), for the case of slowly varying ϵ . Omitting this limitation, we can write these equations in the form

$$\nabla \times \nabla \times \mathbf{E}(\mathbf{r}, \omega) = \left(\frac{\omega}{c_0}\right)^2 \epsilon(\mathbf{r}, \omega) \mathbf{E}(\mathbf{r}, \omega) \quad (2.27)$$

$$\nabla \times (\epsilon^{-1}(\mathbf{r}, \omega) \nabla \times \mathbf{H}(\mathbf{r}, \omega)) = \left(\frac{\omega}{c_0}\right)^2 \mathbf{H}(\mathbf{r}, \omega), \quad (2.28)$$

where the wave number was replaced using $k_0 = \omega/c_0$. Again, both of these equations are independent descriptions of the problem, so that only one of them needs to be considered. In the following, the equation for the magnetic field is used, as it is mathematically more convenient in certain cases.

In the presented form, the wave equations can be interpreted as eigenvalue problems. By introducing a linear, Hermitian operator \mathcal{L} by its action on the magnetic field, i.e.

$$\mathcal{L} \mathbf{H}(\mathbf{r}, \omega) := \nabla \times (\epsilon^{-1}(\mathbf{r}, \omega) \nabla \times \mathbf{H}(\mathbf{r}, \omega)), \quad (2.29)$$

equation (2.28) can be written as

$$\mathcal{L} \mathbf{H}(\mathbf{r}, \omega) = \left(\frac{\omega}{c_0}\right)^2 \mathbf{H}(\mathbf{r}, \omega). \quad (2.30)$$

Here, $\mathbf{H}(\mathbf{r}, \omega)$ can be identified as an eigenvector, and operating with \mathcal{L} on that eigenvector gives the same vector multiplied by a constant $(\omega/c_0)^2$, denoted as the eigenvalue. The eigenvectors $\mathbf{H}_i(\mathbf{r}, \omega)$ are called harmonic modes. Since \mathcal{L} is Hermitian

and positive semi-definite, the eigenvalues, and hence the frequencies ω^2 , are real and nonnegative. Eigenvectors with different eigenvalues are orthogonal, while those with identical eigenvalues are not necessarily orthogonal and called degenerate. From the linearity of \mathcal{L} it moreover follows that any linear combination of modes with the same frequency is again an eigenvector.

2.2.2 Symmetries, point groups and the classification of modes

The possible solutions to the eigenvalue problem (2.30) can be narrowed down using the symmetries of the PhC, defined by the symmetries of the spatial permittivity distribution $\epsilon(\mathbf{r})$. (For simplicity, the notation of the frequency dependence is dropped in the following.) For a formal discussion – although with limited mathematical rigor – some aspects of group theory are explained first, together with explanations on the notation^{*}.

A point group \mathcal{P} , for our purposes, is a set of symmetry operations R_i

$$\mathcal{P} = \{\mathcal{R}_0, \mathcal{R}_1, \dots, \mathcal{R}_n\}, \quad n \in \mathbb{N}, \quad (2.31)$$

which, mathematically speaking, has a group structure with composition as group operation, i.e. is closed under composition. This means that applying two symmetry operations subsequently will give a symmetry operation again, and this operation is as well part of the group. Moreover, the composition is associative and each operation has an inverse \mathcal{R}^{-1} . Each operation \mathcal{R} can be represented by an orthogonal matrix which we denote by $\tilde{\mathcal{R}}$. A symmetry operation can be described using the operator formalism. It must be distinguished if the operator \mathcal{R} acts on a *scalar* field f or a *vector* field \mathbf{F} . In the former case, the spatial coordinates are transformed by the inverse operation

$$\mathcal{R}f(\mathbf{r}) = f\left(\tilde{\mathcal{R}}^{-1}\mathbf{r}\right). \quad (2.32)$$

In contrast, the action of \mathcal{R} on a vector field can be evaluated by

$$\mathcal{R}\mathbf{F}(\mathbf{r}) = \tilde{\mathcal{R}}\mathbf{F}\left(\tilde{\mathcal{R}}^{-1}\mathbf{r}\right), \quad (2.33)$$

i.e. by evaluating the vector field on the inversely transformed spatial coordinates and subsequently transforming the resulting vector field.

Establishing a relation to PhCs, it can be said that the periodicity of the PhC causes the system to be invariant under certain symmetry operations. The totality of these operations is called its point group. Conventional notations of these groups and their properties can be found in appropriate textbooks, e.g. [54, 55]. To stay general a little

^{*}The approach presented here is partly based on the accompanying publication on numerical characterization of symmetry properties [53]. However, the results presented there are not part of this thesis.

longer, let us assume that the arbitrary symmetry defined by the operator \mathcal{R} describes a valid symmetry of the PhC. This means that in equation (2.30), the operator can be replaced as

$$\mathcal{L} = \mathcal{R}^{-1} \mathcal{L} \mathcal{R}, \quad (2.34)$$

that is performing the symmetry operation, applying the operator \mathcal{L} , and then undoing the symmetry operation using its inverse. Recall from quantum mechanics [56], that the commutator of two operators is defined as

$$[\mathcal{A}, \mathcal{B}] := \mathcal{A}\mathcal{B} - \mathcal{B}\mathcal{A}. \quad (2.35)$$

Therefore, operating with \mathcal{R} from the left on equation (2.34) and subtracting $\mathcal{L}\mathcal{R}$ yields

$$[\mathcal{R}, \mathcal{L}] = 0,$$

i.e. \mathcal{R} is a valid symmetry operation of the PhC if it commutes with \mathcal{L} . The commutator is itself an operator and operating on a harmonic mode \mathbf{H} of the PhC yields

$$\begin{aligned} [\mathcal{R}, \mathcal{L}] \mathbf{H} &= \mathcal{R} (\mathcal{L} \mathbf{H}) - \mathcal{L} (\mathcal{R} \mathbf{H}) = 0 \\ \implies \mathcal{L} (\mathcal{R} \mathbf{H}) &= \mathcal{R} (\mathcal{L} \mathbf{H}) = \left(\frac{\omega}{c_0}\right)^2 (\mathcal{R} \mathbf{H}). \end{aligned} \quad (2.36)$$

This is an important result, as it says that whenever a symmetry operator \mathcal{R} commutes with \mathcal{L} , simultaneous eigenvectors of both operators can be constructed. It is hence possible to classify the harmonic modes of the PhC – which are eigenvectors of \mathcal{L} – using the symmetry properties of \mathcal{R} .

2.2.3 Continuous translational symmetry of the dielectric waveguide

A system which is uniform in a specific direction can also be said to have *continuous* translational symmetry along this direction. To express this sentence in more formal terms, we can first define an operator $\mathcal{T}_{\mathbf{d}}$ that shifts the dielectric function by \mathbf{d} , i.e.

$$\mathcal{T}_{\mathbf{d}} \epsilon(\mathbf{r}) = \epsilon(\mathbf{r} - \mathbf{d}). \quad (2.37)$$

If a system is uniform in x -direction, for instance, we could state that the operator $\mathcal{T}_{x\hat{\mathbf{e}}_x}$, which shifts in the direction of the unit vector in x -direction $\hat{\mathbf{e}}_x$, would leave the permittivity of the system unchanged

$$\mathcal{T}_{x\hat{\mathbf{e}}_x} \epsilon(\mathbf{r}) = \epsilon(\mathbf{r} - x\hat{\mathbf{e}}_x) = \epsilon(\mathbf{r}).$$

Let us now consider the dielectric slab waveguide of thickness h (figure 3, left), which is the limiting case of $r \rightarrow 0$ of the patterned PhC slab, as stated above. The slab is homogenous in the xy -plane and of finite thickness in z -direction, so that the permittivity

(neglecting dispersion) can be described as

$$\epsilon(\mathbf{r}) = \epsilon(z) = \begin{cases} \epsilon_1 & \text{if } |z| \leq h/2, \\ \epsilon_2 & \text{else} \end{cases}, \quad \epsilon_1 > \epsilon_2. \quad (2.38)$$

This function is hence constant for all vectors $\boldsymbol{\rho}$ parallel to the xy -plane (or rather perpendicular to the plane normal, which is the z -axis). Just as mentioned before in general, it can be concluded that the translation operator \mathcal{T}_ρ commutes with \mathcal{L} , i.e. $[\mathcal{T}_\rho, \mathcal{L}] = 0$. This has the benefit that the modes of the system can be classified according to their in-plane wave vectors $\mathbf{k}_{\text{ip}} = k_x \hat{\mathbf{e}}_x + k_y \hat{\mathbf{e}}_y$, allowing to separate the z -dependence

$$\mathbf{H}_{\mathbf{k}_{\text{ip}}}(\mathbf{r}) = e^{i\mathbf{k}_{\text{ip}} \cdot \boldsymbol{\rho}} \mathbf{h}(z, \mathbf{k}_{\text{ip}}). \quad (2.39)$$

Here, $\mathbf{h}(z, \mathbf{k}_{\text{ip}})$ denotes the z -dependence of the magnetic field, while the exponential is a plane wave describing the xy -dependence. Exploiting the rather simple condition of translational symmetry, thus, allowed us to reduce the problem from a completely general solution, to modes which only have an unspecified behavior in z -direction.

To go even further, we can divide the k -vector into components parallel and perpendicular to the xy -plane, so that

$$|\mathbf{k}| = \sqrt{k_{\parallel}^2 + k_{\perp}^2},$$

i.e. $k_{\parallel} = |\mathbf{k}| \sin \theta$ with θ being the angle between \mathbf{k} and the plane normal. For reasons that will shortly be clear, we divide the solution space (i.e. the spectrum) into parts which are above and below the so-called light line $\omega = c_0 k_{\parallel}$. The frequency $\omega = c_0 |\mathbf{k}|$ can only have values smaller than $c_0 k_{\parallel}$ if k_{\perp} is imaginary. But this means that the corresponding modes are evanescent in the direction away from the slab, and therefore confined to it – a solution well known from ray optics, known as total internal reflection or index-guiding. We say that these modes – the guided modes – are spatially bounded. In contrast to the solutions above the light line – the radiation modes – resemble the plane waves of free space if going farther away from the slab.

It can be shown mathematically, that for a Hermitian eigenvalue problem like equation (2.30), the solutions form a discrete set when the eigenvectors are spatially bounded (see [57], chapter 6). In consequence, the modes below the light line form a set of continuous bands, which we can number by ascending frequency order with the so-called band number n . The totality of all the (uncountably infinite number of) bands is known as the band structure of the system. Above the light line, the modes form a continuum, which is usually denoted as the light cone. (Actually, this is also part of the band structure, but with non-negative real numbers $n \in \mathbb{R}_0$, instead of integers $n \in \mathbb{N}_0$.)

These results are as well of great importance here, because the situation is very similar for PhC slabs, as will be shown below after the treatment of 2D PhCs. The PhC slabs,

which have discrete rather than continuous symmetries, form guided modes below the light line as well. Above the light line, however, a different situation is met. And moreover, each discrete symmetry gives another property that can be used to classify the modes, as discussed in the following.

2.2.4 Discrete symmetries, Bloch's theorem and the Brillouin zone

The continuous translational symmetry discussed in the previous section is valid if the system can be translated by infinitesimal steps dr , e.g. $\epsilon(\mathbf{r} + dr) = \epsilon(\mathbf{r})$. PhCs rather have discrete translational symmetry, for which the dielectric function can only be translated by lattice vectors \mathbf{R} , which can be expressed as a linear combination of the primitive lattice vectors \mathbf{a}_i , hence $\mathbf{R} = \sum_i^N m_i \mathbf{a}_i$. Here m_i are integers and N is given by the dimension of the system – e.g. there are typically three primitive lattice vectors in a 3D system. Accordingly, the complete space can be “tiled” by a finite volume known as the unit cell. It is further possible to define a reciprocal lattice using reciprocal lattice vectors \mathbf{G} , which itself can be expressed by primitive reciprocal lattice vectors \mathbf{b}_i , so that $\mathbf{G} = \sum_i^N m_i \mathbf{b}_i$. The \mathbf{b}_i can be derived from the \mathbf{a}_i by demanding $\mathbf{a}_i \cdot \mathbf{b}_j = 2\pi\delta_{ij}$. This approach is well-known from solid state physics and more information can be found in [52], chapter 4, or [1], appendix B.

As in the case of continuous translational symmetry, the discrete translation operators $\mathcal{T}_{\mathbf{R}}$ which relate to the lattice vectors \mathbf{R} must all commute with \mathcal{L} , allowing to decouple the modes in the following way

$$\mathbf{H}_{\mathbf{k}}(\mathbf{r}) = e^{i\mathbf{k}\cdot\mathbf{r}} \mathbf{u}_{\mathbf{k}}(\mathbf{r}), \quad (2.40)$$

where $\mathbf{u}_{\mathbf{k}}(\mathbf{r}) = \mathbf{u}_{\mathbf{k}}(\mathbf{r} + \mathbf{R})$ is a lattice-periodic function. This is known as Bloch's theorem and the modes $\mathbf{H}_{\mathbf{k}}(\mathbf{r})$ are called Bloch states or Bloch modes. And just as it is sufficient to consider the unit cell in order to describe the system in real space, it is sufficient to consider wave vectors in a “reciprocal unit cell”, commonly known as the first Brillouin zone. The wave vectors \mathbf{k} can therefore be replaced by Bloch wave vectors $\mathbf{k} = \sum_i^N k_i \mathbf{b}_i$, i.e. by a superposition of the primitive reciprocal lattice vectors, and these vectors can be restricted to the Brillouin zone. As will be shown shortly, this region can further be reduced to a so-called irreducible Brillouin zone if the lattice has more symmetries, such as rotational symmetry.

Finally, we can again reason that the modes of the eigenvalue problem equation (2.30) are spatially bounded, this time to the unit cell of the PhC. For 3D PhCs, the modes are bounded in all three directions, causing the spectrum to be fully discrete. The band structure then does not have a light cone, but is completely composed of continuous bands $\omega_n(\mathbf{k})$ that can be labeled by a band number n . Moreover, this band structure must only be considered in the irreducible Brillouin zone, because the frequencies are as well Bloch periodic: $\omega_n(\mathbf{k}) = \omega_n(\mathbf{k} + \mathbf{G})$ for all reciprocal lattice vectors \mathbf{G} . The same

holds for 2D PhCs, because the continuous translational symmetry in the uniform direction causes the same spatial boundedness as for the slab waveguide.

2.2.5 2D photonic crystals with hexagonal lattice

Until now, only *translations* have been considered. Discrete translational symmetry is a key property of any periodic lattice, as it defines the unit cell and the first Brillouin zone. However, the unit cell itself can exhibit additional symmetries, which therefore also apply for the complete system.

It was already shown in section 2.2.2, that any symmetry operator \mathcal{R} of the point group \mathcal{P} (2.31) of the system commutes with \mathcal{L} , therefore $[\mathcal{R}, \mathcal{L}] = 0$. For a system with discrete translational symmetry as discussed in the previous section, this means that any transformed Bloch mode $\mathcal{R} \mathbf{H}_{\mathbf{k}}$ of equation (2.40) satisfies the eigenvalue problem (2.30) with the same eigenvalue as the initial Bloch mode (compare equation (2.36)). Further, it can be shown that this is actually the *same* Bloch mode with a transformed wave vector $\mathcal{R} \mathbf{k}$. But this means, that the eigenvalues ω , and therefore the band structure $\omega_n(\mathbf{k})$, possesses the same symmetry as the point group \mathcal{P} . It is therefore sufficient to consider the band structure in the irreducible Brillouin zone, which is the smallest part of the Brillouin zone with nonredundant \mathbf{k} vectors.

C_{6v} point group and hexagonal Brillouin zone

After these very general statements, we will discuss the properties of the lattice of interest for this thesis: the hexagonal lattice. The first Brillouin zone of this lattice is the hexagon shown in figure 4 (left). The hexagonal lattice itself is shown at the right of the same figure, illustrated by a center point and its six nearest neighbors. To describe the symmetries of this system, we introduce a notation often used in group theory. We denote rotations of $2\pi m/n$ around the origin with C_n^m , e.g. a rotation around $60^\circ = 1 \cdot 2\pi/6$ is C_6 . Obviously, the hexagonal lattice can be rotated by any angle which is a multiple of 60° , as shown by the blue arrows in figure 4. Also, a mirror reflection on the x - or y -axis leaves the lattice unchanged. These reflection are denoted as $\sigma_{x/y}$ and marked using red arrows in the figure. There are even more planes for which these mirror flips can be performed, but these are the same operations as $\sigma_{x/y}$ if the coordinate system is changed, and therefore marked with primes and called conjugate operations. The same is true for the clockwise rotations, which are also shown in the figure and marked with a superscript of -1 . Together with the identity operation E , we can therefore find the symmetry operations

$$\{E, C_6, C_6^{-1}, C_3, C_3^{-1}, C_2, \sigma_x, \sigma'_x, \sigma''_x, \sigma_y, \sigma'_y, \sigma''_y\}. \quad (2.41)$$

If we combine the conjugate operations and add them as factors, we find the so-called C_{6v} point group

$$C_{6v} = \{E, 2C_6, 2C_3, C_2, 3\sigma_x, 3\sigma_y\}. \quad (2.42)$$

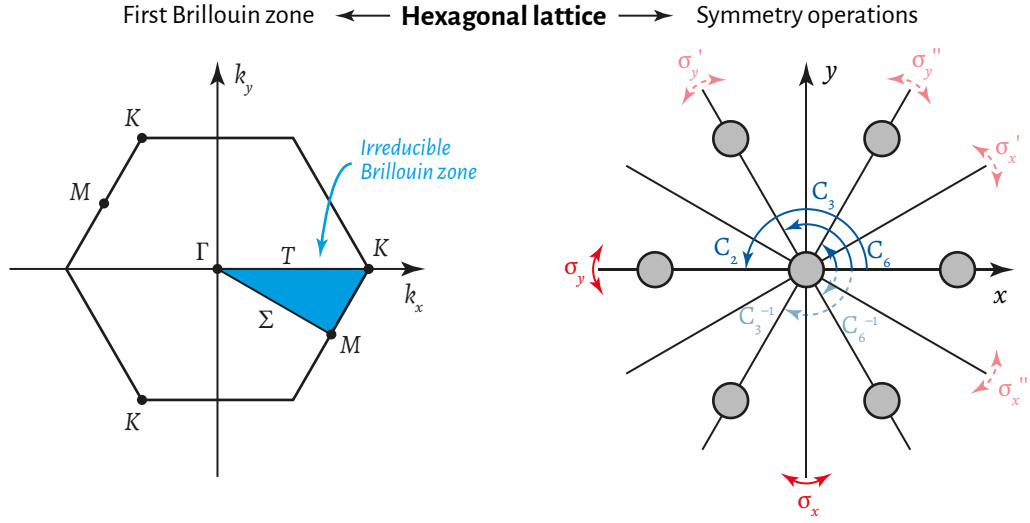


Figure 4: Symmetry properties of the hexagonal lattice. (Left) First Brillouin zone (in k -space) and irreducible Brillouin zone (cyan) with high symmetry points Γ , M , and K , as well as named intermediate points T and Σ . (Right) Symmetry operations of the hexagonal lattice (in real space). Rotations C_n^m are shown in blue, while mirror flips $\sigma_{x/y}$ are shown in red. Operations which are conjugate to other operations appear faded and with dashed lines. (Freely adopted from [2].)

Taking into account these symmetries yields the irreducible Brillouin zone shown by the cyan-hued triangle in figure 4. The corners of this triangle are points of particularly high symmetry – therefore called high symmetry points – termed Γ , M and K .

Symmetry of modes and irreducible representations

Let us recapitulate that the *system*, i.e. the dielectric function of the 2D PhC with hexagonal lattice (figure 3, center), has the C_{6v} point group defined in equation (2.42). So far, the previous considerations have been preparations for the conclusions that will be discussed in the following – because the important question for this work is: What can we learn about the properties of the *modes* from symmetry?

Since it is beyond the scope of this thesis to give a profound treatment, the following aims at motivating the idea of irreducible representations (see [2, 53, 55, 58] for more information). If we solve for the modes of the PhC for a specific direction of incidence of the light source, the corresponding wave vector \mathbf{k} can be regarded as the position in the irreducible Brillouin zone shown in figure 4. At normal incidence, for example, we are at the Γ -point and the system shows its full symmetry, i.e. C_{6v} . If we are a little off the Γ -point, the symmetry is reduced, that is why Γ is called a high symmetry point.

\mathbf{C}_{6v}	\mathbf{E}	$2\mathbf{C}_6$	$2\mathbf{C}_3$	\mathbf{C}_2	$3\sigma_y$	$3\sigma_x$
\mathbf{A}_1	+1	+1	+1	+1	+1	+1
\mathbf{A}_2	+1	+1	+1	+1	-1	-1
\mathbf{B}_1	+1	-1	+1	-1	+1	-1
\mathbf{B}_2	+1	-1	+1	-1	-1	+1
\mathbf{E}_1	+2	+1	-1	-2	0	0
\mathbf{E}_2	+2	-1	-1	+2	0	0

Table 2.1: Character table of the C_{6v} point group. Each row lists the characters χ for an irreducible representation (denoted as A_i , B_i and E_i) respective the symmetry operations of the C_{6v} point group (the identity operation E , rotations C_n^m and mirror flips $\sigma_{x/y}$; compare equation (2.42)). The characters of the representation types A and B only take values of ± 1 , while the higher dimensional E type can take all values $-2, -1, \dots, 2$.

At other special points, lower symmetries are found, which can be summarized as

$$\begin{aligned}
\mathcal{P}_\Gamma &= C_{6v}, \\
\mathcal{P}_K &= \{E, 2C_3, 3\sigma_y\} = C_{3v}, \\
\mathcal{P}_M &= \{E, C_2, \sigma_y'', \sigma_x''\} = C_{2v}, \\
\mathcal{P}_T &= \{E, \sigma_y\} = C_{1h}, \\
\mathcal{P}_\Sigma &= \{E, \sigma_x''\} = C_{1h}.
\end{aligned} \tag{2.43}$$

That is, the point group \mathcal{P}_K at the K point is called C_{3v} and has a lower symmetry than C_{6v} , because it is composed of only six symmetry operations; and similar for the other points.

Let us now consider a non-degenerate mode of the PhC at the Γ -point. It can be shown, that this mode always exhibits the symmetry of one of the so-called irreducible representation of the C_{6v} point group. To understand this concept, consider that the mirror flip operator σ_x acts on a function $f(x)$, described by the eigenvalue problem $\sigma_x f(x) = \chi f(x)$ with an eigenvalue χ . No matter how $f(x)$ looks like, a second application of σ_x will restore $f(x)$ to its original state, so the eigenvalues χ can only be ± 1 . This eigenvalue is therefore known as the character of $f(x)$ respective the symmetry operation σ_x .

The same can be done for the PhC modes and all the symmetry operations of the point group. A result from group theory [55] is now that not all combinations of these characters χ can occur, but only a distinct number, which are the irreducible representations \mathcal{I} of the point group. In the case of C_{6v} , these are six combinations labeled A_1, A_2, B_1, B_2, E_1 and E_2 . It is common to specify these representations in so-called character tables, which list the values of the characters χ , as shown in table 2.1 for C_{6v} .

The reason for showing this table here in detail is to make absolutely clear, that an irreducible representation is nothing but a set of specific symmetry properties. For ex-

ample, the irreducible representation A_1 defined by the first row in table 2.1, transforms even under all symmetry operations, i.e. with a character χ of $+1$. The representation types A and B can have characters of only ± 1 , while the higher dimensional E type can take all values $-2, -1, \dots, 2$. Only these six symmetry types can occur for the modes of a PhC with hexagonal lattice at the Γ -point, and they can be classified easily from the field distributions by consulting this table. It will be explained in the following, that far-reaching conclusions can be drawn from these simple considerations. And in the end, the finite number of these types and the knowledge on how they behave will justify the machine learning approach used in later chapters.

Consequences for the photonic band structure

To relate these results to the photonic band structure, we repeat that at the Γ -point, any mode of the PhC can be assigned to one of these irreducible representations and that this is moreover a conserved quantity [55]. It can further be shown, that any non-degenerate mode is of A - or B -type, while degenerate modes are of type E . So whenever two bands cross at the Γ -point, which also means that they are orthogonal eigenvectors which can not couple, it can be concluded that both have a symmetry of E -type. In contrast, bands that show anticrossing – i.e. which couple and show a frequency splitting, are either A - or B -modes.

Although it is not shown here explicitly, very similar conclusions can be drawn for the other high symmetry points, and we can moreover find so-called compatibility relations which tell us how the mode symmetry evolves between these points. As an example, a mode which is of type A_1 at Γ , will be of type A when moving along the path $\Gamma - K$ in the Brillouin zone (figure 4), and will therefore be mirror symmetric with respect to the x -axis.

In consequence, when considering mirror and rotational symmetry, a photonic band will either (i) keep its symmetry respective a certain symmetry operation when moving from one high symmetry point to another, or it will (ii) flip its symmetry on the way between these points. We do not expect any drastic or sudden changes in the symmetry. These results are of major importance, as in later sections machine learning will be used to classify the bands between high symmetry points based on their field distribution. This approach would not make any sense, if we did not know that the bands have these continuous symmetry properties. In consequence, these theoretical results justify the classification of field distributions into a rather small number of types between two high symmetry points, as it will be done in chapter 7.

2.2.6 Photonic crystal slabs and leaky modes

The photonic crystal slab with hexagonal lattice can now be treated as a combined case of the 2D counterpart and the dielectric waveguide (compare figure 3). All the concepts have already been introduced, and are often repeated in the PhC literature. The band

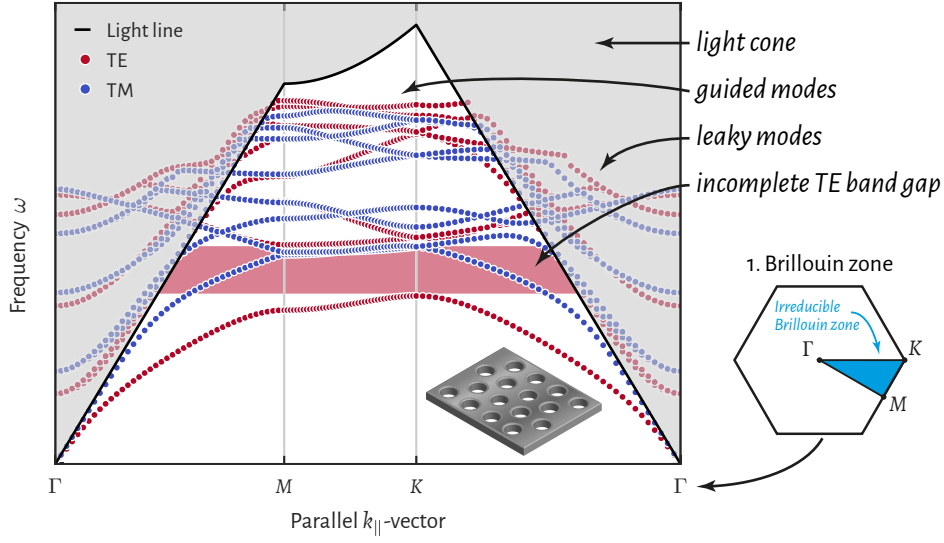


Figure 5: Example of a band structure for a photonic crystal slab with hexagonal lattice. Band structure[†] $\omega_n(k_{||})$ for the first 8 TE (red circles) and TM (blue circles) bands, respectively, solved along the edge of the irreducible Brillouin zone (cyan area in the shown 1. Brillouin zone) with markings for the high symmetry points Γ , M and K (see also figure 4, left). The inset shows a sketch of the PhC slab, which is surrounded by air. The black line and the gray area denote the light line $\omega = c_0 k_{||}$ and the light cone; the latter is the region of the leaky and radiation modes. The TE bands exhibit a band gap (red-shaded area) for the guided modes, but not for the leaky modes, so that it is said to be incomplete.

structure features discrete modes which can be classified by their irreducible representations, but the finite thickness in z -direction introduces a light cone, just as for the uniform dielectric slab.

An example of a band structure for a PhC slab without substrate is shown in figure 5[†] (see the inset for a sketch of the structure). The band structure $\omega_n(k_{||})$ has been solved along the edge of the irreducible Brillouin zone (cyan area in the shown 1. Brillouin zone; or figure 4, left) for the first eight transverse-electric (TE) (red circles) and transverse-magnetic (TM) (blue circles) bands, respectively. TE and TM refer to different polarization types, as will be explained in the next paragraph. The light line $\omega = c_0 k_{||}$ (black line) separates the domain of the guided modes (white area) from the light cone (gray area). The latter, which is of special interest in the case of external radiation, is the domain of radiation modes and so-called leaky modes. This is in contrast to the dielectric slab discussed in section 2.2.3, for which the light cone is composed of a continuum of radiation modes only. The leaky modes, however, are discrete modes – just as the guided modes – and will be discussed after the polarization types. Another

[†]The band structure in figure 5 was computed using MIT Photonic Bands (MPB) [59] for a constant relative permittivity of $\epsilon = 12$ without substrate. The computation uses a supercell in z -direction and it is known that MPB does not yield correct results above the light line in this case.

feature of the band structure is the incomplete TE band gap denoted by the red-shaded area. A band gap is a frequency range without any allowed modes (usually for a specific polarization), which in the case of PhC slabs is only possible for guided modes – hence it is incomplete. Therefore, this phenomenon is only relevant if the excitation occurs inside the slab, i.e. below the light line.

Separation of TE and TM modes

If we consider the 2D PhC with hexagonal lattice a last time, the C_{6v} point group describes the symmetry in the xy -plane, but in z -direction the system is uniform. This means that the PhC has mirror symmetry with respect to the xy -plane for *any* choice of origin. Calling the related symmetry operator σ_z , it can again be reasoned that $[\sigma_z, \mathcal{L}] = 0$; and from this it again follows that the parallel Bloch vectors possess the same mirror symmetry, i.e. $\sigma_z \mathbf{k}_{\parallel} = \mathbf{k}_{\parallel}$.

All of these considerations are analog to the line of reasoning of the previous section. The modes can therefore be classified by their character $\chi(\sigma_z)$, which can take values of ± 1 depending on whether the fields are even or odd with respect to that symmetry. The mirror symmetry is a special case, because electric and magnetic fields transform differently under this transformation. Without going into detail, this is because \mathbf{E} is a vector, while \mathbf{H} is a so-called pseudovector [43]. This causes that the modes can be classified by their polarization characterized by the non-zero field components, which can either be (E_x, E_y, H_z) – denoted as TE – or (H_x, H_y, E_z) – denoted as TM.

In the case of general 3D PhCs, this separation does only apply under very specific conditions and is therefore irrelevant (a proof can be found in chapter 3 of [1]). However, for the case of PhC slabs the separation holds by approximation if the slab is thin compared with λ , i.e. the modes are mostly polarized in that case (see [1], chapter 7). Since this condition is met in many cases of interest for this thesis, the concept of TE- and TM-modes is used – most of the time as if it held exactly. Nevertheless, one should be aware of the fact that it is an approximation and that the polarizations are not perfectly orthogonal.

Anything that breaks the $z = 0$ mirror plane of the slab deteriorates the orthogonality of the polarizations. In the present case, this is e.g. the substrate material or the conical shape of the holes (see section 3.2). The more pronounced the conical shape gets, or the more the refractive index of the substrate material approaches the one of the slab, the worse will be the orthogonality. These aspects must also be kept in mind when the terms TE and TM are used, and they will be reconsidered in later discussions.

Leaky modes and their link to reflection, transmission and near-field enhancement

The actual system with which this thesis is concerned is called the nanohole array, and it is introduced in detail in section 3.2 and figure 9 on page 49 (material properties are discussed in section 3.3). It is a silicon PhC slab with a hexagonal lattice of holes

on a glass substrate. This system has the C_{6v} point group in the xy -plane for z -values inside the slab. If the substrate and superstrate materials are identical, the system has $C_{1h} = \{E, \sigma_z\}$ symmetry with respect to the z -axis, so that the total symmetry can be denoted as $D_{6h} = C_{6v} \times C_{1h}$.

The eigenmodes of such a system can be classified by their irreducible representations, but as noted above and explained in section 2.2.3 for the dielectric waveguide, there is also a light line dividing the photonic band structure into two parts. As shown in figure 5, the modes below the light line form discrete bands, which are called the guided modes. Since these modes are confined to the slab, they can only be excited by the zeroth-order forward- and backward-diffracted waves of an external source. Consequently, they are of minor interest for this thesis.

For the dielectric waveguide, it was stated that the region above the light line is composed of a continuum of modes: the radiation modes. However, in the case of a PhC slab the situation is quite different, although this is often neglected in textbooks on PhCs which mainly deal with guided modes – or at least not optimally communicated. The reason for this “negligence” is mainly that the situation is rather complex. Fortunately, the publication of Hu & Menyuk [60] gives an in-depth overview of this specialized topic, so that it is sufficient to cover selected conclusions here.

We can therefore state that the PhC slab possesses another type of modes above the light line: the leaky modes. These modes can be seen as quasi-eigenmodes, which – in contrast to the guided modes – have finite lifetimes (see also [2, 12, 58]). Unlike for the dielectric waveguide, the continuum of radiation modes above the light line contains sharp Lorentzian peaks at k_z -values which are close to the $k_{||}$ wave vector components of the guided modes. The widths of these Lorentzian peaks, which can also be expressed by Q-factors, correspond to the lifetimes of the leaky modes.

From the in-plane periodicity it is therefore possible to excite the leaky modes using higher (evanescent) orders of the external radiation by phase-matching [11, 30]. The spectral bandwidth for which this is possible depends on the Q-factor of the leaky mode. These modes, which can be defined by a complex propagation constant, are diffracted in both the forward and the backward directions, so that they change the reflection and transmission properties of the PhC. More specifically, from studying the interference it can be shown that an externally excited leaky mode causes zero transmission at the resonance wavelength, i.e. 100 % reflection, in the case of a perfectly periodic, infinite and lossless system [8]. The leaky modes can therefore be observed using e.g. reflectance measurements (see section 3.4.1) [9, 10].

It must however be noted, that there are further restrictions for the excitation of modes, imposed by the symmetry match between the light source and the irreducible representation of the mode. This means that the leaky modes may not *all* be excited using e.g. external plane waves, so that the bands observed like this do not cover the complete band structure. (More details can again be found in [2, 12].)

Finally, from the spatial boundedness of the leaky modes during their finite lifetimes, it follows that they can locally induce very high energy densities [30]. This effect will be referred to as “near-field (energy) enhancement”, especially for the case that the energy densities of e.g. the electric field are higher than those of the incident field (which is usually assumed as a plane wave excitation having a uniform energy density, here).

From these theoretical thoughts it is obvious that a proper design of PhC slabs facilitates to change the reflectance properties of this material, as well as to manufacture systems which possess strongly increased field energies for specific illumination conditions. As a final section in this theoretical treatise of PhC slabs, it will be discussed how these characteristics can be applied to the interaction with emitters.

2.2.7 Interaction with emitters by enhanced extraction and enhanced emission

The effects of leaky modes on the general optical properties of PhC slabs have been outlined in the previous section. As it is of major relevance for the results presented in chapter 6, it will now be discussed how these features can be used to affect the interaction with near-surface emitters, which can be thought of as two-level systems here. The two effects of interest are extraction enhancement and excitation enhancement, of which the latter directly changes the emission rate, while the former improves the outcoupling of the generated light.

Extraction enhancement

Suppose a two-level system emitting a single photon in free space. The photon will be emitted in an arbitrary direction with a frequency corresponding to the energy separation of the two levels via $E = hf$. If there are many emitters emitting many photons, the directional characteristic will not favor a specific direction, so that half of the radiation will be emitted to the upper half space. If, in contrast, these emitters are *in the center* of a dielectric slab waveguide (section 2.2.3), a large fraction of the radiation will couple to the guided modes of the waveguide – typically around 80 % to 90 %, depending on the refractive index – so that only 5 % to 10 % are radiated to the upper half space [14].

However, if the emitters are not inside the slab waveguide, but only very *close to the surface*, the effect is still relevant, because the guided modes are still present, although exponentially decreasing away from the slab. Similar problems are massively deteriorating the extraction efficiency of light-emitting diodes (LEDs) [11], which mainly struggle with the outcoupling of the light that is generated in the emission zone. As it was stated in the previous section, in the case of PhC slabs the in-plane periodicity changes this behavior. This is basically because the PhC folds the guided modes at the Brillouin zone boundaries, so that the phases between the guided modes match those of the radiation modes above the light line. These quasi-guided modes have been introduced as leaky modes.

Consequently, light from external sources is scattered out of the PhC plane, which can as well enhance the extraction of light from near-surface emitters. This effect is denoted as extraction enhancement, or enhanced extraction, and it was studied intensively [9–11, 14, 21–26]. Extraction enhancement requires the emitters to match the resonance frequency of a leaky mode in the range of its bandwidth. Or more generally, if the emitters have a distribution of emission wavelengths, leaky modes must cross this wavelength range. In contrast to the effect which will be studied in the following, leaky modes of all symmetry types, polarizations and k -vectors come into consideration for this effect, assumed that the emitted light of a single emitter has arbitrary polarization and emission direction.

Excitation enhancement

A completely different approach to increase the emission of a near-surface emitter is given by excitation enhancement. Suppose the absorption and stimulated emission induced in a two-level emitter interacting with a monochromatic electromagnetic wave, just as taught in fundamental textbooks on lasers, e.g. Svelto [61]. The interaction can be understood as to happen between the electric dipole moment of the emitter and the electric field. In this simplified picture, it turns out that the transition rate W of stimulated emission is of the form

$$W \sim \rho g(\lambda - \lambda_0), \quad (2.44)$$

where the energy density ρ of the wave is proportional to the square of the electric field amplitude: $\rho \sim E_0^2$; and the function $g(\lambda - \lambda_0)$ is the Lorentzian with center wavelength λ_0 . From these basic considerations, it can be seen that the (stimulated) emission of a two-level system increases quadratically with the field strength at the position of the emitter.

It was also mentioned in the section on leaky modes of section 2.2.6, that these modes can exhibit locally enhanced field energy densities. This was also shown experimentally, reaching multiple orders of magnitude [27]. It is therefore obvious, that the emission of an emitter in the proximity of the PhC slab surface can be increased if it is in the region of leaky mode-enhanced field energy, as demonstrated in [30, 42]. We denote this mechanism as excitation enhancement, or enhanced excitation. As a side note, this effect should not be confused with the Purcell effect [62], which is basically caused by a high density of states in a specific volume, while excitation enhancement in this case is caused by a single mode. Unfortunately, the nomenclature in respective publications is inconsistent. Therefore, to achieve excitation enhancement,

- the PhC slab must exhibit a leaky mode that spectrally overlaps with the absorption profile of the emitter, and
- the emitter position must coincide with a region of increased field of the mode profile.

Consequently, this effect is caused by leaky modes present at the specific wavelength λ_{in} , wave vector k_{in} and polarization of the incident radiation, – in contrast to extraction enhancement, where leaky modes must be present at the emission wavelengths of the emitters, but for *any* k -vector and polarization.

2.3 Aspects of machine learning

Machine learning is a huge and rapidly developing subfield of computer science, which deals with algorithms that can learn from data and even make predictions on it. It is sometimes difficult to distinguish machine learning from the related fields of artificial intelligence, pattern recognition, computational statistics or data mining, which partly overlap and share many of their methods. The application areas of machine learning are numerous and as well growing, today occupying all fields of science and everyday-life from medicine, biology, linguistics and economics to online security, advertising and insurance, to name only a few.

Due to this suggested complexity it is inevitable to restrict the treatise in this thesis to a minimum, concentrating on the parts which have been utilized for the results in later sections. More complete introductions to the field can be found in related textbooks, such as [63, 64] for the mathematical background, or [65] with a focus on applications.

However, since machine learning is yet far from being a standard tool in physics, it is assumed that the reader might not have a sound knowledge in this field. Therefore, a short introduction with a basic example is given before the actual theoretical treatment, which also tries to motivate how machine learning can be of use for the work at hand. Afterwards, the general task of machine learning will be introduced in brief, followed by a summary of the relevant clustering techniques and implied methods of result evaluation.

2.3.1 Introduction and motivation

Illustrating the principles and abilities of machine learning is best achieved using an example. In this case, it will be necessary to already use some key terms, which will more stringently be defined in the following sections, but which might appear intuitive to some extent.

The method exclusively relevant for this thesis is classification. In order to introduce this method, a standard example data set has emerged, which is the so-called iris data set from the field of plant taxonomy. It goes back to E. Anderson, who did the actual measurements, and Fisher, who published them in 1936 [66]. Irises are flowering plants for which Anderson measured four characteristics, namely the sepal length, sepal width, petal length and petal width, – i.e. properties of specific leaves. These measurements have been performed for 50 plants of each of the three species *I. setosa*,

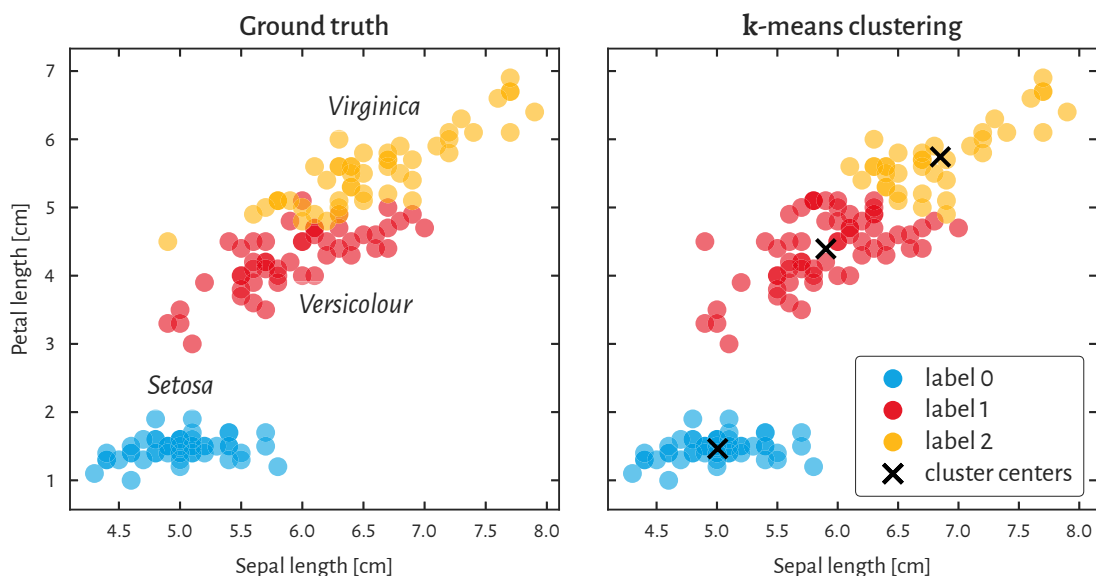


Figure 6: Clustering of the iris data set. The 150 samples of the iris data set are plotted against their sepal and petal lengths. **(Left)** The ground truth, i.e. the correct assignment of the data points to the three species *virginica*, *versicolour* and *setosa*; using a different color for each class (semitransparent). **(Right)** *k*-means clustering result using corresponding colors for each cluster. The black crosses mark the positions of the cluster centers.

I. versicolour and *I. virginica*. Fisher tried to find out how the species could be determined from the four leaf properties.

We say that this data set has 150 *samples* (the 3×50 measured plants) and 4 *features* (the different leaf lengths); and it can be divided into 3 *classes*. For this specific data set, the correct assignments to the different classes are known, which is referred to as the ground truth. One aspect of classification would be to let the machine *learn* how to assign the features to the classes, e.g. using half of the data set, and then to let the machine *predict* the right classes for the other half. However, the problem of interest for this thesis is even more sophisticated: can the machine divide the data set into three classes without any help, i.e. without giving any example of a correct assignment? This is the task of clustering.

One of the most simple, but powerful clustering algorithms is called *k*-means, and it will be introduced in detail in section 2.3.4. The *k*-means algorithm takes two inputs: (i) the measured leaf lengths for each plant, and (ii) the number of clusters into which the data should be partitioned. The results of this process are summarized in figure 6 and have been obtained using the open-source Python library Scikit-learn [67], as for all the machine learning-based results in this thesis. The four measurements for each plant can be considered as a point in a four-dimensional space. For visualization purposes this is reduced to 2D by plotting only against petal and sepal length. The left-hand plot shows the ground truth, using different colors for each species. When plotted like this,

each species forms a point cloud, where *virginica* and *versicolour* are less well separated than *setosa*. Although the 2D depiction is a simplification that in fact neglects information, the full-4D situation is quite analog. (Partly because petal length and petal width are highly correlated, so that the data set is basically 3D.) The right-hand plot shows the *k*-means result, where each point was assigned to a cluster labeled 0, 1 or 2. The algorithm tried to find a proper grouping of the data points based on their inter-distances in the 4D space, forming clusters of points which “may” belong to the same group. Doing so, the algorithm managed to group all samples of *setosa* correctly, and also most of the other two species. Problems, or rather ambiguities, arise at the border between *virginica* and *versicolour*, where *k*-means is unable to assign all samples correctly due to the small distance between the clusters.

Obviously, a technique like this can indeed be useful to find “meaning” in data sets, at least if the user is able to interpret the labeling. For the iris data set, which has few samples and only four feature dimensions, the same result may have been achieved using traditional techniques or by clever visualization. But when it comes to large, high-dimensional data sets, clustering can become indispensable.

This is where the method becomes interesting for photonics. In chapters 5 and 6, specific effects of PhCs will be studied in large ranges of wavelengths and incident angles of the incoming radiation. When, for example, emitters are placed on the PhC surface, their emission can be influenced by the local field strength. From the field enhancement *integrated* over a specific volume in which the emitters are supposed to be, experimental data may be understood to some extent. However, to gain insight into the fine details, the *exact* field distribution for all combinations of incident angles and wavelengths is relevant. Without any additional knowledge this would necessitate to visualize and interpret thousands of 3D field distributions.

This problem can be simplified by taking into account the theoretical consideration that the field distributions are not unique for each radiation condition. It was shown in section 2.2 that PhCs have a band structure, and that these bands have typical field distributions corresponding to their symmetry properties. The fields in the regions between the bands are also not expected to be “wild”. So it may be possible to classify these field distributions and to only look at very few typical fields, which are sufficient to understand the observed phenomena.

Machine learning seems to be ideally suited to meet this objective. If we consider e.g. the electric field at specific positions as the features, just like the leaf lengths in the iris example above, and the different radiation conditions as the samples, which have been the specific plants before, the problem can be clustered in just the same way. Only the problem size differs a lot: suppose we are interested in 500 different incident angles and 500 wavelengths, we end up with 250 000 samples. To achieve a reasonable resolution for the 3D field values, we might use at least 25 points in each direction, resulting in 15 625 features, i.e. 15 625 dimensions.

Coming back to the iris example again, the k -means algorithm yielded another result, despite from the assignment of the measurements to classes. If we consider all samples in one cluster, the *average* sepal length could be considered as the *typical* sepal length. The same holds for the other features, and these are the so-called “cluster centers”. These centers are marked using black crosses in section 2.3.4, and they lie rather good in the center of each point cloud. In the same way, the PhC field clustering would yield typical modes of the field. And just as mentioned above, these average field distributions will be used to explain the actual experiments in chapter 7.

2.3.2 Mathematical notation and general problem set

After the descriptive introduction in the previous section, it is from now on tried to give a more stringent treatment. The general goal of machine learning is to construct a prediction rule which connects a set of *samples*, represented by an input vector X , to a set of outputs, represented by an output vector Y . The input vector is composed of N_s samples X_i with $i = 0, \dots, N_s - 1$ and each sample can itself consist of N_f *observations* x_j with $j = 0, \dots, N_f - 1$. Here the subscripts s and f stand for “samples” and “features”, respectively. The observed quantities for each sample are denoted as *features*. The input vector is thus a matrix of size $N_s \times N_f$.

The output or response vector can itself consist of N_r output variables Y_m with $m = 0, \dots, N_r - 1$, where the subscript r stands for “response”. The output measurements corresponding to each sample X_i are denoted as y_i , so that the output matrix is of size $N_r \times N_s$. The treatment will be restricted to the very common case of $N_r = 1$, so that the output vector Y is a column vector of length N_s : each sample X_i corresponds to one specific output y_i . These outputs can either be quantitative, i.e. ordered, numerical values, or qualitative, i.e. unordered, categorical values. The former case is referred to as regression, while the latter is known as classification. Just as stated in the introduction, the treatise will be restricted to the problem of classification. The general task of machine learning is then to construct a prediction rule in a way that, given a sample vector X_i , a “good” prediction for the output \hat{y}_i is made. Here, the hat distinguishes the predicted output from the actual output y_i [63].

2.3.3 Supervised learning, unsupervised learning and clustering

Machine learning is usually subdivided into the tasks of supervised and unsupervised learning. For supervised learning the process starts with a training set, which is a set of N_t samples X_i with known outputs y_i . In the iris example (section 2.3.1), this would be the case if the algorithm is trained using N_t leaf lengths sets with known species. Once the algorithm is trained, it can be used to predict the species \hat{y}_k of other plants X_k . A main advantage of supervised learning is that a direct measure of success is available, as there is always a set of known outputs. The training set can therefore be divided

into a smaller training set and a test set, so that the predictions based on the reduced training set can be checked against known results.

With unsupervised learning, the situation is different in the way that there are no known outputs. The input matrix X represents a set of N_s points in a N_f -dimensional, abstract feature space. Unsupervised learning algorithms can further be categorized according to their task. The clustering approaches, which are of interest here, try to find regions of the X -space which can be “clustered” to distinct types of observations, therefore to find classes in the X -space that are valid approximate representations of the complete data space. These classes are usually referred to as centroids or cluster centers. Other unsupervised learning approaches are for example descriptive statistics, with the principle components analysis as a frequently used algorithm, and many more [63].

Due to the lack of a direct measure of success, it is difficult to ascertain the validity of the determined cluster centers. It is in consequence a crucial step to validate the solutions using “external” knowledge about the problem itself, i.e. to compare it to the expectation. In addition, there are also mathematical tools to rate the clustering, of which the silhouette coefficients will be considered in section 2.3.6.

2.3.4 k-means clustering

A specific algorithm for solving the task of clustering is k -means. This method is very popular for being robust and versatile, while having rather simple core ideas, which be outlined in the following. It is noted that there are many other algorithms, each having its pros and cons. A well-grounded comparison of k -means to other methods for the problems at hand is beyond the scope of this thesis, as well as giving a detailed explanation of such methods. As a second, more complex example, Gaussian mixture models will briefly be covered afterwards, which have been applied to the clustering of a more complicated data set in section 7.4.

As stated before, the goal of the clustering approach is to partition a N_f -dimensional data set X with N_s samples X_0, \dots, X_{N_s-1} into some number N_k of clusters. A cluster comprises a group of data points whose inter-point distances are small compared with the distances to points outside of the cluster [64]. This can be formalized by introducing a set of N_f -dimensional vectors μ_k , where $k = 0, \dots, N_k - 1$ and μ_k is the centroid of the k -th cluster. In order to find the optimum solution, the algorithm must find an assignment of data points to clusters, and a set of centroids $\{\mu_k\}$, such that the sum of squares of the distances of each data point to its closest vector μ_k is a minimum.

The assignment of data points X_i to a cluster k can be described by a corresponding set of binary indicator variables $r_{ik} \in \{0, 1\}$, so that if X_i is assigned to the cluster center k then $r_{ik} = 1$, while $r_{ij} = 0$ for $j \neq k$. The sum of squares of the Euclidian distances of

each data point X_i to its assigned centroid $\boldsymbol{\mu}_k$ is then given by

$$J = \sum_{i=0}^{N_s-1} \sum_{k=1}^{N_k} r_{ik} \|X_i - \boldsymbol{\mu}_k\|^2, \quad (2.45)$$

where $\|\dots\|$ denotes the Euclidian vector norm

$$\|\mathbf{v}\| = \sqrt{\sum_i v_i^2}, \quad (2.46)$$

so that the general Euclidian point distance between two vectors \mathbf{v} and \mathbf{u} , which is just a generalization of the Pythagorean formula, is

$$\|\mathbf{v} - \mathbf{u}\| = \sqrt{\sum_i (v_i - u_i)^2}. \quad (2.47)$$

The task of the k -means algorithm is to minimize J , which is in general done by optimizing for r_{ij} and $\boldsymbol{\mu}_k$ alternately in successive optimization steps.

The k -means algorithm always converges, but is prone to fall into local minima. This behavior drastically depends on the initialization, i.e. the initial choice of the centroids $\boldsymbol{\mu}_k$. To address this problem, k -means is in general executed multiple times with different initializations. An additional approach is to use advanced seeding techniques such as the k -means++ algorithm [68], which was also used in this thesis.

2.3.5 Clustering using Gaussian mixture models

The k -means algorithm presented before is a very simple and robust method, but it also has its disadvantages. Simply speaking, it assumes that the clusters are circular, i.e. representable by a (hyper-)sphere in feature space. The center of this sphere defines the cluster center, while the radius acts as a hard boundary used to decide which samples belong to the cluster. For that reason, k -means is often called a *hard* clustering method, in contrast to *soft* methods such as the one based on Gaussian mixture models (GMMs) presented here [63]. A rigorous treatise of the GMM clustering is rather involved and can be found e.g. in [64], so that this method is only outlined here.

Starting with a 2D analog, it may be intuitively clear that a sum of Gaussian distributions of the form

$$\mathcal{N}(x) = \frac{1}{\sqrt{2\pi\sigma^2}} \exp\left(-\frac{(x-\mu)^2}{2\sigma^2}\right) \quad (2.48)$$

can fit almost any continuous function $f(x)$ if only enough Gaussians are used. Here, μ is the mean of the distribution and σ^2 is the variance (the square root σ being the standard deviation). This Gaussian function of the scalar variable x can easily be extended

to a multivariate Gaussian distribution, taking the form

$$\mathcal{N}(\mathbf{x}) = \frac{1}{(2\pi)^{D/2}} \frac{1}{|\tilde{\Sigma}|^{1/2}} \exp\left(-\frac{1}{2}(\mathbf{x} - \boldsymbol{\mu})^T \tilde{\Sigma}^{-1}(\mathbf{x} - \boldsymbol{\mu})\right) \quad (2.49)$$

for a D -dimensional vector \mathbf{x} . Here, $\boldsymbol{\mu}$ is now a D -dimensional mean-vector and $\tilde{\Sigma}$ is a $D \times D$ covariance matrix with determinant $|\tilde{\Sigma}|$ [64].

Just as reasoned above for the Gaussian function, a superposition of N multivariate Gaussian distributions of the form

$$p(\mathbf{x}) = \sum_{i=1}^N c_i N_i(\mathbf{x}) \quad (2.50)$$

can be used to approximate almost any continuous density to arbitrary accuracy. Equation (2.50) is called a Gaussian mixture, the $N_i(\mathbf{x})$ are called components of the mixture, and the c_i are weight factors. Coming back to the task of clustering, the multivariate Gaussians give a much more flexible representation of clusters than in the case of k -means, where it was mentioned that the clusters are assumed to be circular.

A GMM can therefore represent much more complex data sets and can be seen as a generalization of the k -means algorithm for non-circular clusters. One can imagine that it would be straightforward to fit the multivariate Gaussians to a data set for which the labels are known. With unlabeled data the case is more difficult, and enforces to take into account another step. In the literature, this problem is commonly denoted as to find out which (latent) component is “responsible” for a certain sample, – which is somehow a different way of asking to which cluster the sample belongs. But it underlines that the GMM clustering is a probabilistic approach, because it calculates the probability that the sample was generated by cluster i for *all* clusters. These probabilities, which are also called responsibilities, are simply the weight factors c_i of equation (2.50). This is another advantage over the k -means method, as samples near the boundary of two clusters have non-zero probabilities for both clusters, e.g. in the case of being exactly at the boundary of cluster i and j , the probabilities would be $c_i = c_j = 0.5$.

In the implementation that was utilized in section 7.4, the cluster assignment is solved using a method known as expectation-maximization [69, 70]. This rather complex statistical algorithm starts with a random Gaussian mixture (i.e. random components), which is typically initialized using a prior application of k -means to improve the convergence. In the next step it determines for each sample the probability of being generated by each component of the mixture. Based on these probabilities, the parameters of the Gaussian distributions are fitted to give the best approximation of the data by maximizing the so-called likelihood [64]. This process is executed iteratively and is guaranteed to converge to a local optimum.

The advantages of the greater flexibility of this method in view of the cluster shape are inevitable for the clustering in section 7.4. It should be noted that the GMM approach has further advantages which are yet not used, e.g. an alternative implementation that uses a variational Bayes model to automatically predict the optimum number of clusters. This approach was tested but did not lead to satisfying results, most probably because the considered input data is in fact not “generated” using a mixture of Gaussians. Further thoughts on these issues are discussed in the concluding remarks of chapter 8.

2.3.6 Real-world scenarios

Both of the presented clustering algorithms RE completely agnostic about the nature of the input data and, hence, the user must take care to apply it to reasonable data in a real-world scenario. This means, at first, that the data should be expected to actually feature classes and one should have an interpretation of what these classes are. Once this basis is set, the remaining task is to acquire and preprocess suitable data, run the chosen algorithm and to assess the solution. To address the remaining tasks of this listing, a brief note on preprocessing will be given next, followed by an explanation of the mathematical approach that was used to assess the clustering results.

Standardization

As already pointed out in section 2.3.1, in the scope of this thesis the data acquisition comes down to generating field distribution data using electromagnetic simulations. Since the absolute values of the field strengths can vary by large amounts, it is crucial to standardize the field data, as it is typical for a clustering problem. There are numerous possible standardization techniques, e.g. scaling the data to fixed minimum and maximum values or to a common mean and unit variance. A common operation in clustering, specifically, is to normalize the data, which means to scale each sample to unit norm individually. This technique was used throughout the thesis, as it performed best in numerous tests.

Solution quality rating using silhouette coefficients

Once the clustering is done, the quality of the solution must be validated in some way. Aside from comparing the results to the expectation, there are also mathematical ways for this assessment, namely the silhouette coefficients [71]. Both of the considered clustering algorithms expect the number of clusters N_k to be specified. This enforces to have a guess for the approximate range of possible N_k -values beforehand. The silhouette coefficients provide a way to assess the initial choice of the number of clusters, *and* how well the samples lie in their respective clusters, at the same time.

In simple terms, the silhouette coefficient rates how well a sample fits into its own cluster. If it is far away from all other clusters and very close to the cluster center, the sample gets a positive rating. If the distances to a different cluster and its own cluster are comparable, it is rated with values close to zero. Finally, if it is much closer to a different cluster, a negative rating is assigned.

To give a definition of this measure, let X_i^k be a sample that was assigned to the cluster k and $a(i)$ be the average dissimilarity of X_i^k to all other members $X_{j \neq i}^k$ of this cluster. The measure for the dissimilarity is usually the Euclidian distance (2.47). Let $d(i, m)$ be the average dissimilarity of X_i^k to all members of the cluster $m \neq k$ and $b(i)$ be the minimum of $d(i, m)$ for these clusters, i.e.

$$b(i) = \min_{m \neq k} d(i, m).$$

The cluster m for which this minimum is obtained is called the neighboring cluster of X_i . If the number of clusters is > 1 , we can define the silhouette coefficient $s(i)$ for the sample X_i by

$$s(i) = \frac{b(i) - a(i)}{\max\{a(i), b(i)\}} = \begin{cases} 1 - a(i)/b(i), & \text{if } a(i) < b(i) \\ 0, & \text{if } a(i) = b(i) \\ b(i)/a(i) - 1, & \text{if } a(i) > b(i) \end{cases} \quad (2.51)$$

From this definition it is seen that the silhouette coefficient is in the range $-1 \leq s(i) \leq 1$. Values near 1 indicate that the sample is far away from the neighboring cluster and accordingly fits well into its own cluster. A value of 0 indicates that the sample is on or very close to the boundary between its own and the neighboring cluster, and negative values indicate that it might have been assigned to the wrong cluster.

A sorted diagram of all silhouette coefficients can thus be used to visualize the representation quality of a clustering. Explanations on how to use these diagrams will be provided in the corresponding sections, for instance in section 7.2 (figure 32). In addition, the average silhouette coefficient for all samples – usually denoted as “silhouette score” – can be used to compare the representation quality for different clusterings, e.g. using different N_k -values. It hence even provides a single numeric value for solution quality assessment.

Considering the iris example of section 2.3.1 a last time, figure 7 repeats the k -means clustering result of figure 6. This time, different markers are used for the labels 0, 1 and 2, while the color represents the silhouette coefficient $s(i)$ for the corresponding sample. The color map covers the complete range of the silhouette coefficient, and is chosen in a way that (i) greenish colors show good fits ($s(i) \approx +1$), (ii) reddish colors show samples close to the boundary of the neighboring cluster ($s(i) \approx 0$), and (iii) blueish colors show samples which are misclassified. Obviously, there are no bluish markers, which is a good sign for a well-clustered result. The *setosa* samples with label

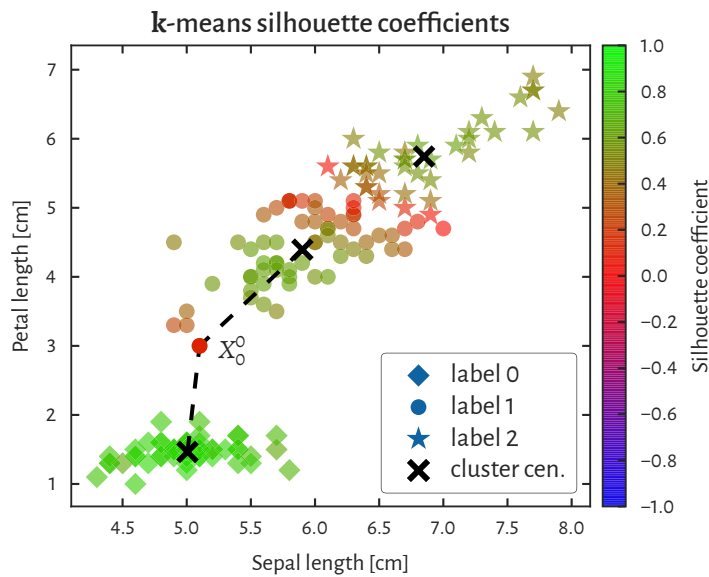


Figure 7: Silhouette coefficients of the iris data k -means clustering. The result of the k -means clustering of figure 6 is shown again using different markers for the labels, color-coded by the silhouette coefficient $s(i)$. Dashed lines mark the distances to the two nearest cluster centers for an exemplary sample X_0^o with a silhouette coefficient of $s(0) \approx 0.14$.

0 have silhouettes very close to one, due to the isolation of the cluster. At the boundary of *versicolour* and *virginica* with labels 1 and 2, there are many reddish points, just as it is expected from the bad separation between these clusters. Also, even the highest silhouette coefficients of both of these clusters are only moderately positive, i.e. for each sample there is still a probability that it may belong to the neighboring cluster. Another sample which is at a boundary is marked in the figure with X_0^o . It has a silhouette coefficient of $s(0) \approx 0.14$. The dashed lines illustrate that this sample is effectively closer to the neighboring cluster center, although only in the simplified 2D plot. In the same way, the silhouette technique can be used to interpret more complex situations, as will be shown in section 7.2.

“No method nor discipline can supersede the necessity of being forever on the alert.”

— HENRY DAVID THOREAU —

3

Methods and Materials

THE PRESENTATION OF THE RELEVANT METHODOLOGICAL ASPECTS will be given in this chapter and is divided into three logical parts: (1) the numerical methods, (2) a description of the idealized photonic crystal (PhC) system, and (3) the aspects of the real system and related experiments.

Part 1 is covered in section 3.1 and gives an overview of computational photonics to motivate the choice for the method that was actually used: simulations using a finite element method (FEM) Maxwell solver. The mathematical background is outlined and important practical aspects are discussed. As an exception, the machine learning-based methods are not described in their own methodical section, but were basically given in the treatment of the fundamentals in section 2.3. Remaining details of the actual techniques are given in the relevant places of chapter 7, in order to facilitate the comprehension of the rather complex results.

A transitional part between numerical and experimental sections is realized with part 2, which deals with the nanohole array system in section 3.2. The general geometry is described and details on the numerical treatment and the derivation of the physical quantities of interest are presented.

Finally, part 3 spreads across three sections that cover the involved materials (section 3.3), the experimental techniques (section 3.4) and the fabrication of the PhC samples (section 3.5). These sections also treat issues of the quantum dots (QDs) in some detail, which have been an important component of the fluorescence enhancement experiment, whose results are presented in chapter 6.

3.1 Finite element method for the treatment of photonic crystals

As explained in chapter 2, the physics behind any aspect of photonics and, thus, also behind photonic crystals, come down to the Maxwell equations (2.1). This could be regarded as a beautiful simplicity of the complete discipline, if there would not be the drawback that the Maxwell equations can only be solved analytically for *very* simple cases. This situation gave rise to numerical methods being vastly employed for photonic crystals, especially because the conditions are rather good: the material properties are at hand and the length scales are not too small [1].

The Maxwell equations are a set of coupled differential equations including both partial and full derivatives. A variety of specialized methods has evolved [44] to solve certain cases of the Maxwell equations, often given by the wave or Helmholtz equations and with different spatial discretizations. The totality of these techniques is often considered as a standalone discipline referred to as computational photonics.

It is the purpose of this section to give a brief overview of the available techniques with a focus on their specific application areas and their strengths and weaknesses. Finally, the important aspects of the FEM, which was utilized for the numerical results of this thesis, will be discussed and the choice for this specific method will be motivated.

3.1.1 Computational photonics in a nutshell

According to the generalities given by Joannopoulos *et al.* [1], there are different ways to categorize the methods in computational photonics, e.g. by the (i) nature of the problem which is solved or by the (ii) discretization approach. When categorizing by (i) we can basically subdivide the approaches into

- frequency-domain eigenproblems,
- frequency-domain responses, and
- time-domain simulations.

The frequency-domain techniques typically deal with steady state solutions of the Maxwell equations, i.e. with a time-dependence $\exp(-i\omega t)$, and solve the problem for a single frequency ω or rather wavelength λ . They generally involve linear-algebra techniques to solve a certain matrix equation. **Frequency-domain eigenproblems** address the very specialized field of band structure computations, which means to solve for the electromagnetic fields and the frequencies $\omega(\mathbf{k})$ as a function of the wave vector k . The inverse problem, i.e. solving for \mathbf{k} for given ω is known as on-shell band structure computation. The related algorithms, such as the plane wave method used in the popular open-source implementation MIT Photonic Bands (MPB), are usually limited to infinitely periodic systems.

The **frequency-domain responses**, in contrast, are specifically designed for finite systems and need special implementations to deal with infinite regions. The common task is to find the electromagnetic fields as a response to a given current density

$\mathbf{J}(\mathbf{r})e^{-i\omega t}$, or in the case of the scattering problem an incident field \mathbf{E}_{in} , by rewriting the problem as a matrix equation of the form $Ax = b$ and solve for x . These methods are, therefore, generally well suited for scattering simulations, where the focus is on near-field or far-field properties of non-periodic or realistic systems.

Time-domain simulations directly solve for the time evolution of the electromagnetic fields for a present time-dependent current source $\mathbf{J}(\mathbf{r}, t)$ or an external field. This has the advantage to solve for the system response at multiple frequencies, but with the drawback that typically a large number of time-steps needs to be executed until the sources have decayed. A benefit when being in time-domain is that such simulations can directly be linked to phenomena beyond electromagnetics, for instance molecule kinetics or diffusion[44].

Another aspect, as stated above, is the reduction of the infinite number of points in space to a finite one, i.e. the spatial **discretization** (ii). Important approaches are

- finite differences,
- finite elements, and
- boundary-element methods.

The most simple approach is **finite differences**, where a uniform (typically Cartesian) grid is used to discretize the fields and their derivatives in form of differences at discrete points. The greatest advantage of e.g. the most commonly used implementation, the finite-difference time-domain (FDTD) method, is its simplicity. The Maxwell equations are solved *as is*, without any further complex assumptions, allowing to study all characteristics of the field evolution *in situ* [44]. This comes at the cost to update the field components at each point in space and at each time step, without the possibility to update regions of interest. Moreover, the uniform grid always gives a bad representation for any curved geometries (although it can be improved using subpixel-smoothing [72]).

Most of these drawbacks are greatly improved when considering **finite elements**, where the space is divided into finite geometric elements such as triangles or tetrahedra in 2D or 3D, respectively. The corresponding grid allows to use very different scales for the elements and, hence, can be adjusted to the actual physical situation. Also, curves can be represented much more naturally. The general approach is to approximate the fields by low-degree polynomials defined on each element.

Finally, **boundary-element methods** only discretize the boundaries, while treating the homogenous regions in between analytically. These semi-analytical methods can be advantageous when dealing with very different length scales, since the thickness of analytically treated layers does not influence the computation time. A similar approach is used in the transfer-matrix method and the rigorous coupled-wave analysis (RCWA). The main disadvantages are typically the necessary slicing, e.g. in the case of curved geometries [73].

Motivating the choice of FEM

From all the possibilities listed in the previous section, the finite element frequency-domain approach was utilized for all numerical results in this work; implemented in the finite element solver JCMSuite, which is specialized on the Maxwell equations. The choice of a specific numerical technique can always be subject to debates, and attaining an *unbiased* recommendation can be difficult (or it necessitates to perform suitable benchmarks for the desired problem). That said, there are good reasons to use finite element Maxwell solvers for the systems in question, which will be given in the following. Section 3.1.1 gave an overview of the available computational methods for the treatment of the considered systems. Although this overview is (necessarily) incomplete, it might be sufficient to narrow down the possible techniques to the ones which are appropriate for the case at hand.

It was already stated that the problem of interest is the scattering simulation, and that this problem is characterized by an electric field that can be split into a finite interior and an infinite exterior part. The interior can moreover be infinitely periodic in certain dimensions. When considering the possibility of time-domain simulations, it must be stated that the interest here is not in the time-evolution of the fields, but on characteristic quantities in steady-state, e.g. on reflectance or field energy distributions. From the first categorization approach in the previous section, the frequency domain methods are the natural choice.

When considering the discretization, it will be shown in section 3.2 that the target system includes rounded objects, and that the involved length scales are comparable (except for e.g. upper and lower half-spaces). In consequence, boundary-element methods are disadvantageous due to the slicing approach and there is no expected benefit from the parts that are treated analytically. Finite-differences techniques are not preferable as well for the same reason, leading to the preference for the finite element discretization.

Altogether the FEM appears to be well-adapted to the problems in question. It must be noted that there are of course many, sometimes highly specialized methods, which are not listed above. But when compared, an ultimate advantage of the FEM is often the well-established convergence theory (see e.g. [74], and [75] for the example of the RCWA). Due to the vast number of application areas of the FEM, complex approaches for error-control, error-estimation and adaptive improvement have emerged, which are often absent in specialized techniques.

3.1.2 Basic principles

In the following, it is tried to give a *notion* of the FEM as used for this thesis, explaining the basic intentions and important parameters. It is refrained from giving a detailed mathematical description, as it is not essential for the understanding of the results and necessitates to consider rather involved mathematical constructs. Substantiated

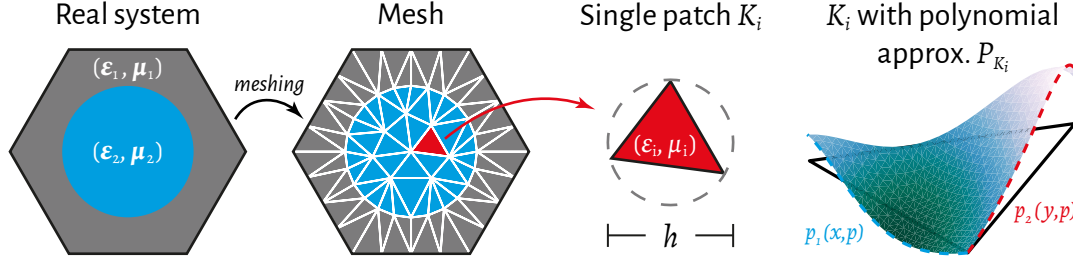


Figure 8: Illustration of the finite element method principle. The real system with spatially dependent material functions ϵ, μ is partitioned into patches K_i (here: triangles) with constant material functions ϵ_i, μ_i . The patches have a typical size of h , e.g. defined by their circumference; and each patch holds a local part of the solution, basically represented by polynomials P_{K_i} of degree p . The right most sketch shows an illustrative local solution using two polynomials $p_1(x, p)$ and $p_2(x, p)$.

presentations of the matter can be found in e.g. [44, 74, 76].

To realize the FEM, the Maxwell (2.5) or Helmholtz (2.15) equations are converted into a so-called weak form [74], and a discrete solution space V_h is constructed, which must be a reasonable approximation of the exact solution space V . This solution space is obtained from a discretization of the computational domain into a finite number of patches K , with a typical size of h , and by assigning a set of polynomials P_K up to the polynomial order p to each patch. This situation is illustrated in figure 8, where the real system on the left is subdivided into triangular patches K_i (center right) that form the mesh (center left); generated in a process called meshing. In 3D, the patches are itself 3D fields, for example tetrahedra. Each patch K_i represents a finite part of the physical system with homogenous material parameters, $\epsilon, \mu = \text{constant}$. The polynomials are used to approximate the part of the global solution which is located on the patch K_i , as indicated on the right of figure 8. In a simplified view, a patch K_i together with its polynomial approximation P_{K_i} are called a finite element.

To give a notion of how to solve a system like this numerically, we follow the reasoning given by Burger *et al.* [77] (rigorous derivations can be found in [47, 74]). The Maxwell equations are transformed to a weak form, which is a single equation for the electric field \mathbf{E} of the form

$$g(\varphi, \mathbf{E}) = f(\varphi), \quad (3.1)$$

where g and f are integral expressions and φ are test functions of the solution space V . In the finite element discretization the test functions φ are restricted to a finite dimensional subspace V_h of dimension N , as noted above. Denoting this with the subscript h , equation (3.1) becomes

$$g(\varphi_h, \mathbf{E}_h) = f(\varphi_h). \quad (3.2)$$

This problem can be linearized by introducing basis functions b_i to express the dis-

cretized field vectors and test functions, i.e.

$$\mathbf{E}_h = \sum_{i=1}^N c_i b_i, \quad \varphi_h = \sum_{i=1}^N \varphi_i b_i,$$

where the c_i are unknown expansion coefficients. In the case of a Galerkin method, the basis functions are chosen from the same space V_h as the test functions. To solve for the unknown expansion coefficients, a linear system of equations is obtained by testing with the b_i

$$\sum_{i=1}^N g(\varphi_j, \varphi_i) c_i = f(\varphi_j), \quad j = 1 \dots N. \quad (3.3)$$

The $N \times N$ matrix $\mathcal{G} = g(\varphi_j, \varphi_i)$ is sparse, i.e. has mostly zero entries, and can be solved efficiently using numerical techniques. Finally, the polynomials of degree p defined on a single patch at a time (as mentioned above) are used to construct the basis.

3.1.3 Boundary conditions

It was so far tried to give a notion of how the FEM problem is solved in the *interior* domain, but without specifying what happens on the boundaries of the computational domain. Besides the simple periodic and reflecting cases, transparent boundaries are of great importance, while at the same time being a rather complex subject. Each time one desires to model a region which is extending to infinity, e.g. a half-space of homogenous material, transparent boundaries must be applied. This is typically the case in scattering simulations.

From the numerous strategies for the implementation of transparent boundaries, the perfectly matched layers (PMLs), first proposed by Berenger [78], are among the most commonly used. Technically speaking, the PML is rather an additional layer with special properties than an absorbing boundary condition; modeling a material which continues virtual to infinity. Inside the PML it is tried to attenuate the electromagnetic waves to zero before they may enter the interior domain again after a possible reflection on the “actual” computational domain boundary. This is mathematically achieved using a coordinate transformation that converts oscillating waves to exponentially decaying waves.

From the reasoning above it may be obvious that the PML itself requires parameters to be set in order to reach the goal of being a transparent boundary, such as the extension of the PML elements. In the actual FEM implementation utilized for this thesis, this step is redundant due to the implementation of adaptive PMLs, which use the self-consistently described physical situation present in the FEM. Details can be found e.g. in [46, 79].

3.1.4 Error characterization

Today, one typically does not need to care about the *minutiae* of the FEM when using a modern code such as JCMsuite. When treating complex physical situations, one often relies on the mathematical part being implemented as a “black box”. However, except from defining the system geometry and post-processes, there are still points left the end-user needs to care about – and these have mainly to do with convergence.

Estimating the convergence of the finite element method rigorously may depend on very specific characteristics, such as on the sharpness of geometrical elements or the choice and implementation of boundary conditions. When being on the “application side” of the finite element method, one thus depends on a number of approximate rules, a reliable implementation of the elaborate techniques and a conscientious convergence study which mostly involves a parameter scan. Advanced matter on the convergence properties can be found in [74, 76, 80].

However, the dominating determining factors of the accuracy are the meshing, or in a simplified view the patch size h , and the finite element polynomial degree(s) p . The shape of the patches plays a minor role, although later in section 4.4 it will be discussed in some detail that patches with high aspect ratios should be avoided. Also, too small angles or angles larger than 90° should be circumvented, which is typically done by defining a minimum mesh angle and using patch geometries that automatically assure angles $< 90^\circ$.

In the general case, the near-field error \mathcal{E} satisfies the proportionality

$$\mathcal{E}_{\text{general}} \propto \left(\frac{nh}{\lambda_0} \right)^p, \quad (3.4)$$

where n is the refractive index of the local material and λ_0 is the vacuum wavelength of the exciting source. The error can thus be reduced by refining the mesh and by increasing the polynomial degree p , the latter being favorable as it decreases the error exponentially. Consequently, it is appropriate to choose h “as large as possible and as small as necessary”, i.e. $h = h_{\text{max}}$, while increasing p until the desired error limit is reached. However, an exact expression for h_{max} is hard to find, as it also depends on the actual field solution [81, 82]. (When arguing from an engineering point of view, it is at least necessary to comply with the implications of the Nyquist–Shannon sampling theorem [83].) As a starting point for scattering problems, we hence use the approximate rule that the maximum patch size should be of the size of the wavelength in the given material

$$h_{\text{max}}(\lambda_0, n) \approx \frac{\lambda_0}{n} \quad (3.5)$$

Nonetheless, care must be taken if singularities arise in the solution, e.g. at sharp corners in the geometry, because the error is then bound by h^k , with $k < p$ being the

number of possible continuous differentiations of the solution, and is better described by

$$\mathcal{E}_{\text{singularities}} \propto C_0 \frac{nh}{\lambda_0} + C_\infty \left(\frac{nh}{\lambda_0} \right)^p, \quad (3.6)$$

with local constants C_0 and C_∞ . Mathematically, this is related to the so-called regularity of the actual field solution [74]. In such cases the mesh needs to be refined at the crucial spots in order to benefit from increasing p and it is thus of great importance to assure appropriate meshing [81].

3.1.5 Adaptive techniques

In JCMSuite specifically, a number of adaptive and refinement techniques try to provide a convenient way to reach the desired target accuracy. Mathematically, these utilize that the particular FEM is implemented in the hp -formulation [74, 77], which means that it supports variable patch sizes h and variable polynomial degrees p . These techniques try to adaptively find an optimum choice for one or both of these parameters and can be divided in *a priori* and *a posteriori* approaches.

For the *a priori* approaches the solution is completely unknown and in consequence they depend on appropriate error estimation techniques. Besides the simple and less interesting approach to preresolve the mesh, the initial p -adaption-technique can be very useful [74]. This approach tries to estimate the near-field error for each patch based on the illumination set-up and material properties and sets the polynomial degrees p individually for each patch. The aim is to achieve a specified target precision of the near-field solution with minimum problem size, i.e. minimum number of polynomials. Whether this precision is reached depends on the quality of the mesh and the specific geometry.

The *a posteriori* approaches or post-refinement techniques estimate the error based on an initial complete solve, which circumvents the problem of the unknown solution. The error can therefore be estimated from an approximate field solution. The problem is then solved consecutively while changing the mesh or the p -setup. Besides uniform transformations, i.e. subdividing each patch or increasing p globally, JCMSuite again provides adaptive techniques which either refine the mesh or increase p on specific, optimally chosen patches. These approaches allow to reach the desired precision with certainty. However, they suffer from large computational costs since the solving needs to be done over and over again, and the previous solutions need to be stored in memory – effectively causing multiples of CPU times and memory usage. They are thus unfavorable when going for an optimum performance.

3.1.6 Notes on 2D and 3D meshing

It was already pointed out that meshing is one of the most crucial steps in the FEM. A well-designed mesh is necessary to represent the actual physical system as accurately as possible, while using as few elements as possible to keep the problem size small. The specifics of this process must be highly parameterized, so that the user can vary all aspects by, for example, restricting lengths or angles – optimally independently for each subdomain.

In 2D geometries, irregular triangles are the most commonly used patches and there are established algorithms for dividing areas that way, e.g. using Delaunay triangulation [84]. For 3D meshes, there are on the one hand a number of possibilities how to “describe” the 3D mesh, and on the other different patch geometries. The universal case is to partition the full 3D system, e.g. described by constructive solid geometry [85], into tetrahedra. But 3D geometries can also be achieved by *rotating* or *extruding* 2D geometries, which is sometimes simpler and can speed up the meshing process. The case of rotation only applies if the system is rotationally symmetric (this will be used in section 4.3 to model Mie scattering). With extrusion, however, complex systems can be described; – especially if parameters of the initial 2D mesh can be varied from one extrusion layer to the next. If the triangles in the xy -plane are extruded into z -direction, the result is a prismatoidal mesh. This approach will be used for the nanohole array (see section 3.2).

Without going into too much detail, the extrusion process starts with the description of a primitive 2D system in the xy -plane, e.g. a circle in a square computational domain. In the 2D case, domain IDs are used to identify the different parts, for instance to assign material properties. Suppose the computational domain in figure 8 gets the ID 1, while the circle gets 2. If we describe the extrusion of the 2D plane in z -direction, we introduce layers and layer interfaces. The layers are the actual extruded regions with a finite thickness t_i in z -direction. For each layer i , local domain IDs can be mapped to the global ones, e.g. to set different material properties for the “circle” domain in each layer. On layer interfaces, parameters of the 2D primitives can be varied, for instance the radius of the circle can be changed to achieve a conical shape, rather than a cylindrical shape. The total extent of the system in z -direction is finally the sum of all layer thicknesses $\sum_i t_i$.

3.2 The nanohole array

The main investigations of this thesis are carried out using a common PhC design, for which the name “nanohole array” will be used. This section gives a detailed description of the system geometry and the illumination conditions, together with specifics of the meshing for FEM simulations. It thus acts as a reference section which defines every aspect of relevance for later sections and chapters. This is completed with a list of the

parameters of the specific samples used to obtain results and an overview of the physical quantities of interest. Note that the general geometry description considered here is not about specific materials, which are covered in section 3.3.

3.2.1 System geometry and parameters

The nanohole array is a quasi-2D PhC, i.e. a PhC slab, which is composed of a hexagonal lattice of holes in dielectric on a planar substrate. The upper row of figure 9 shows the geometry without superspace in three different views (from left to right): a top view from $+z$ -direction, a cross section through the x -center of a hole, and an isometric view. The top view depicts a hole together with its six nearest neighbors, having a distance of a known as the lattice constant. As seen from the cross section, the holes can have a conical shape defined by the side-wall angle α , so that $\alpha = 0^\circ$ corresponds to the case of cylindrical holes. The radius r of the holes is therefore measured at the z -center of the slab, i.e. at a distance $h_{\text{phc}}/2$ from the slab-substrate interface, where h_{phc} is the height of the slab.

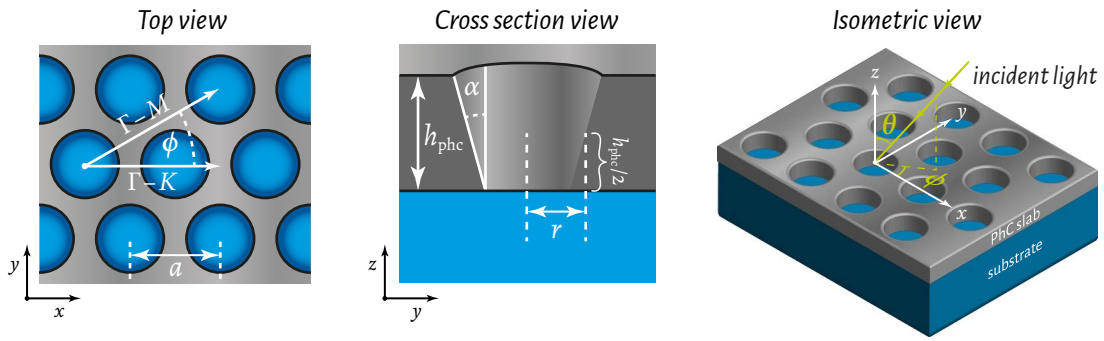
In the top view, there are also markings for the high-symmetry directions $\Gamma - M$ and $\Gamma - K$, related to the high-symmetry points of the reciprocal lattice defined in section 2.2.5 and figure 4. When illuminating the system using plane waves, the direction of incidence will be described using the angles of spherical coordinates θ and ϕ , i.e. the azimuthal and polar angle, respectively. It is seen that the high-symmetry direction can be selected using an appropriate azimuthal angle ϕ , or specifically

$$\Gamma - K : \phi = 0^\circ, 60^\circ, 120^\circ, \dots, \quad \Gamma - M : \phi = 30^\circ, 90^\circ, 150^\circ, \dots \quad (3.7)$$

The isometric view gives a 3D-impresion of a part of the system and depicts an incident ray (greenish), or rather the wave vector \mathbf{k} of the incident plane wave. It moreover defines the polar angle θ , which is the angle between \mathbf{k} and the z -axis; and defines ϕ as the angle between the x -axis and the projection of \mathbf{k} to the xy -plane. If ϕ is fixed according to equation (3.7), increasing the polar angle moves the \mathbf{k} -vector from one high-symmetry point to the other in reciprocal space. Normal incidence, i.e. $\theta = 0^\circ$, is thus analog to the Γ -point, while larger angles move further to K or M .

As mentioned before, these illustrations omit the superspace, which in this case means the volume above the slab. In most cases, the superspace has the same material which also fills the holes, so that the term ‘‘superspace material’’ will mostly include the interior volumes of the holes. The subspace means the volume below the slab and is usually occupied by the substrate in the physical counterpart. Unless otherwise indicated, both the subspace and superspace will be assumed as semi-infinite, i.e. half-spaces.

Geometry and illumination



Example meshes

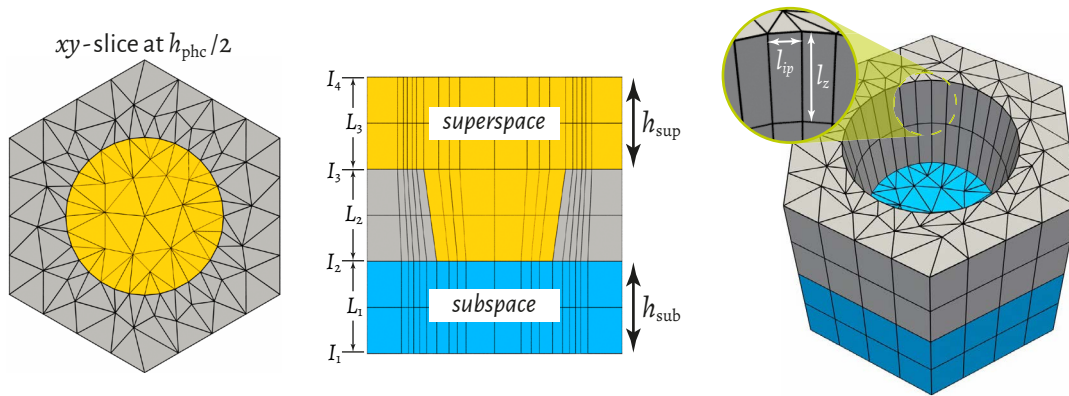


Figure 9: Overview of the nanohole system's geometry and exemplary meshes. (Upper row) Illustrative views of the geometry without superspace. Lattice constant a and high-symmetry directions $\Gamma - M$ and $\Gamma - K$ (compare figure 4) are marked in the top view, as well as the azimuthal angle ϕ of the incident radiation. The cross section depicts markings for the slab height h_{phc} , the side-wall angle α ($= 0$ for cylindrical holes) and the hole radius r measured at $h_{\text{phc}}/2$. The angles θ and ϕ of the incident plane waves are further defined in the isometric view. **(Lower row)** Example FEM meshes for the same view types as in the upper row. Subspace (cyan) and superspace (yellow) are denoted in the cross section mesh, together with the corresponding heights h_{sub} and h_{sup} of the fractions which lie in the (interior) computational domain. Additional labels L_i and I_i mark the layers and layer interfaces, respectively. The zoomed area in the isometric mesh defines the lengths l_z and l_{ip} considered to define the z -ratio mesh control parameter in section 4.4.

3.2.2 Meshing

In addition to the illustrative views of the geometry, the lower row of figure 9 shows FEM meshes of the computational domain of the nanohole simulation. The 3D-layout is obtained using an extrusion of the triangular mesh in the xy -plane, as depicted on the left in figure 9. (Details on the extrusion process are given in section 3.1.6.)

The 2D mesh is composed of a circle inside a hexagonal computational domain. The meshing is basically controlled using side length constraints (SLCs), which limit the maximum side length of the triangular patches, and angle restrictions to set e.g. a lower limit for the inner angles of each triangle. Since the circle is internally represented by a polygon, another important mesh parameter is the number of edges N_p of this polygon. This is crucial as it controls the representation quality of the actual physical system, as will be shown in section 4.3. The actual parameter used to control the number of edges is called circle refinement, which will be denoted as “refine all circle (RAC)” to comply with the JCMSuite nomenclature. The number of edges is given by

$$N_p = 4 \cdot 2^{\text{RAC}}. \quad (3.8)$$

The center mesh of figure 9 shows a cross section through the full-3D, extruded mesh. It shows markings of the four layer interfaces I_i and the three layers L_i . The initial 2D mesh is defined at the layer interface I_1 and in case of a conically shaped hole, i.e. $\alpha \neq 0^\circ$, the circle radius is varied at layer interface I_3 . The layer thicknesses t_i assigned to the layers L_i model the heights h_{phc} , h_{sub} and h_{sup} of the PhC slab and the fractions of the subspace and superspace which are in the interior computational domain, respectively. As outlined in section 3.1.6, domain ID mappings are used to assign the primitive domains of the 2D mesh to the respective 3D domains marked by the different colors.

As illustrated by the isometric view of the 3D mesh at right in figure 9, the computational domain has eight faces: two faces parallel to the xy -plane, and six vertical faces that correspond to the extruded sides of the primitive hexagon. Periodic boundaries are applied to the six vertical faces to model the infinite periodicity of the hexagonal lattice, while transparent boundaries are used for the top and bottom faces to model the half-spaces (see section 3.1.3).

Finally, as seen from the cross section and the isometric mesh, the layers L_i can further be partitioned to restrict the maximum side length in z -direction, or rather to influence the aspect ratio of the extruded, prismatic patches. JCMSuite provides the possibility to set upper, lower and intermediate side length constraints in z -direction for each layer. The isometric mesh features a zoom defining the side lengths l_z and l_{ip} which are used to define the z -aspect ratio as a secondary, more adaptive mesh parameter, which will further be defined and considered in section 4.4.

3.2.3 Illumination using plane waves

The illumination of the nanohole array scattering simulation uses plane wave sources with an electric field of the form

$$\mathbf{E}_{\text{pw}}(\mathbf{r}, t) = \mathbf{E}_0 e^{i(\mathbf{k} \cdot \mathbf{r} - \omega t)}. \quad (3.9)$$

The wave vector \mathbf{k} defines the direction of propagation and is related to the vacuum wavelength λ_0 and the refractive index n of the surrounding medium by $|\mathbf{k}| = 2\pi n/\lambda_0$. As already mentioned above, we can distinguish between the high-symmetry directions $\Gamma - M$ and $\Gamma - K$ using the azimuthal angle ϕ and move between these points with the polar angle θ , both defined in figure 9. The k -vector can therefore be obtained by the appropriate rotations of the wave vector $\mathbf{k}_z = 2\pi n/\lambda_0 \hat{\mathbf{e}}_z$, with the unit vector in z -direction $\hat{\mathbf{e}}_z$, in the form

$$\mathbf{k}_{\theta, \phi} = \mathcal{R}_z^\phi \mathcal{R}_y^\theta \mathbf{k}_z \quad (3.10)$$

with the rotation matrices

$$\mathcal{R}_z^\phi = \begin{pmatrix} \cos \phi & \sin \phi & 0 \\ -\sin \phi & \cos \phi & 0 \\ 0 & 0 & 1 \end{pmatrix}, \quad \mathcal{R}_y^\theta = \begin{pmatrix} \cos \theta & 0 & \sin \theta \\ 0 & 1 & 0 \\ -\sin \theta & 0 & \cos \theta \end{pmatrix}. \quad (3.11)$$

The Maxwell solver provides the possibility to solve for multiple sources in a single run. To understand why the numerical effort is reduced when doing so, we recall the matrix form of the FEM problem stated in equation (3.3). Computationally, the greatest effort is in inverting the sparse matrix \mathcal{G} . However, the sources are included into the vector \mathbf{g} , so that once the matrix is composed, the results for different sources can be obtained from simple matrix multiplications with \mathcal{G}^{-1} and, hence, causes very limited computational cost. The orthogonal polarizations transverse-electric (TE) and transverse-magnetic (TM) (see section 2.2.6) can thus be treated in a single simulation by using two different sources. The k -vector is equal for both sources and defined by equation (3.10). The polarization can be set by altering the amplitude vector \mathbf{E}_0 as follows

$$\mathbf{E}_0^{TE} = \mathcal{R}_z^\phi \mathcal{R}_y^\theta \hat{\mathbf{e}}_y, \quad \mathbf{E}_0^{TM} = \mathcal{R}_z^\phi \mathcal{R}_y^\theta \hat{\mathbf{e}}_x. \quad (3.12)$$

3.2.4 Considered physical quantities

For the nanohole system a number of quantities is determined which are either relevant for the specific study, or accessible via experiments and, therefore, suitable for experiment-vs.-simulation comparisons. Here, the commonly examined quantities are presented, while additional ones will be explained as needed in later sections. Table 3.1 gives an overview of the quantities and respective symbols discussed in the following, additionally listing the kind of post-process from which they are computed and the defining equations.

Quantity	Symbol	Post-process	Equations
Reflectance	R	Fourier transform $+z$	(3.13)
Transmittance	T	Fourier transform $-z$	(3.14)
Absorptance	A	Density int. over $\bar{w}_e(\mathbf{r})$	(2.18), (2.26) and (3.15)
Electric field energy enhancement	E_+	Density int. over $\bar{w}_e(\mathbf{r})$	(2.18) and (3.17)

Table 3.1: Overview of the common output-quantities of the nanohole system. The quantities are listed together with their symbols and the respective post-process from which they are derived in the FEM simulation. The last column lists the references to the equations relevant for their definition.

Reflectance and transmittance

Reflectance and transmittance are very useful quantities, as they can directly be accessed by standard measurements (see section 3.4.1). They are thus useful to oppose simulation and experiment and therefore to test or improve the numerical model. Moreover, plotting the reflectance versus the source's direction of incidence and wavelength reveals photonic bands, as explained in section 2.2.6.

Numerically, two Fourier transform post-processes are used for the calculation, one in $+z$ -direction for the reflectance and one in $-z$ -direction for the transmittance. The Fourier transform requires a homogenous material in a half-space above the plane for which it is computed. As the nanohole array is periodic in two dimensions (compare section 2.2.5), the Fourier spectrum is always fully discrete, which means it results in N diffraction modes. For each diffraction mode i the wave vector \mathbf{k}_i and the electric field strength \mathbf{E}_i is calculated by the post-process, from which the reflectance can be derived as

$$R = \frac{1}{k_0 \|\mathbf{E}_0\|^2} \sum_{i=1}^N |\mathbf{k}_i \cdot \hat{\mathbf{e}}_z| \cdot \|\mathbf{E}_i\|^2, \quad (3.13)$$

where $\|\dots\|$ denotes the vector norm, i.e.

$$\|\mathbf{a}\| = \left(\sum_i |a_i|^2 \right)^{1/2},$$

and \mathbf{E}_0 and k_0 are the field amplitude and norm of the wave vector of the incident plane wave (equation (3.9)). The transmission is derived in almost the same way, but it additionally depends on the refractive index contrast n_\downarrow/n_\uparrow of the subspace and superspace materials

$$T = \frac{n_\downarrow}{n_\uparrow k_0 \|\mathbf{E}_0\|^2} \sum_{i=1}^N |\mathbf{k}_i \cdot \hat{\mathbf{e}}_z| \cdot \|\mathbf{E}_i\|^2. \quad (3.14)$$

Moreover, if critical angles are reached for $n_{\uparrow} > n_{\downarrow}$ (Brewster angle) the Fourier transform does not return any diffraction orders ($T = 0$).

Absorptance

If complex permittivities are set for any domains, absorption occurs. The absorption in a domain j can be calculated from the imaginary part of the total electric energy W_e^j , as obtained from the density integration post-process. To find the total absorptance A of the system, we thus have to sum over all (absorbing) domains (see also section 2.1.2 and equations (2.25) and (2.26))

$$A = -\frac{2\omega}{P_{\text{in}}} \sum_{\text{domains } j} \Im(W_e^j), \quad (3.15)$$

with the incident power

$$P_{\text{in}} = \frac{n_{\uparrow} \cos \theta}{Z_0 F} \|\mathbf{E}_0\|^2. \quad (3.16)$$

Here, F is the area of the computational domain (in the xy – plane in this case), which for the hexagon with lattice constant a is $F_{\text{hex}} = 3\sqrt{3}a^2/8$. It is noted that the sum $R + T + A$ can be used as a validity check for the computation, as it should be unity to satisfy energy conservation.

Electric field energy enhancement

Finally, this work often focusses on near-field enhancement, i.e. on the gain of electric field energy close to the PhC surface with respect to the incident energy. As this effect is interesting in the region above the PhC, the energy enhancement is only considered in the superspace domains of the computational domain, that is the volume inside the hole plus the volume with height h_{sup} above the PhC (see figure 9 on page 49). We denote this specific volume as V_{sup} , so that the electric field energy enhancement is defined as

$$E_+ = \frac{1}{E_{\text{pw},V_{\text{sup}}}} \int_{V_{\text{sup}}} \bar{w}_e dV_{\text{sup}}, \quad (3.17)$$

with the energy of the plane wave in volume V_{sup} being

$$E_{\text{pw},V_{\text{sup}}} = \frac{\epsilon_0}{4} n_{\uparrow}^2 V_{\text{sup}} \|\mathbf{E}_0\|^2.$$

3.3 Properties of involved materials

It is a fact that the numerical results in the field of photonics can only be as good as the underlying data for the optical properties, – which could similarly be stated for any discipline in physics that deals with simulations. Every simulation approach needs input of actual physical data, and these are limiting factors which are often forgotten when trying to increase the numerical accuracy more and more. In fact, when dealing with thin films, the tabulated material data for metals and dielectrics can even be inadequate as they are usually determined using bulk material.

This section gives an overview of the material data that was used in this thesis. The involved dielectrics are not “too thin”, so that values are obtained from standard sources. Greater attention is paid to the lead sulfide (PbS) QDs, which are part of the system investigated in chapter 6. For these emitters the absorption and emission properties, as well as the optical properties, will be covered in detail. Moreover, specifics of the QD coating layer will be discussed.

3.3.1 Notes on the material assignment in the nanohole array simulation

The system for which actual measurements have been performed is the nanohole array, described in section 3.2. In the mentioned section, the geometry was described in general, i.e. without a specification of the materials. Especially the mesh shown at center in the lower row of figure 9 illustrated that the model is basically composed of three domains:

1. subspace (half-space),
2. PhC, or rather a patterned membrane, and
3. superspace (half-space).

The latter is further divided into the volume inside the hole (yellow part between layer interfaces I_2 and I_3 in the mentioned figure), and the half-space above the slab (yellow part above I_3 , infinitely extending). For these three domains, denoted as domains 1/2/3 in the following according to the enumeration above, materials are assigned in the FEM simulation.

The relevant optical property here is the complex-valued permittivity $\epsilon(\mathbf{r}, \lambda)$, or rather the refractive index $\mathbf{n}(\mathbf{r}, \lambda)$ (see section 2.1). In the present case, the refractive index is assumed to have no spatial dependency when defined on a domain, so that \mathbf{n} becomes a scalar function of the wavelength $\mathbf{n}(\mathbf{r}, \lambda) = n(\lambda)$. Moreover, as a frequency domain technique, the utilized FEM code uses a single fixed wavelength per simulation, so that n becomes a scalar complex number. Although it can be seen as a drawback that wavelength-dependent investigations using the FEM always require a parameter scan, it though means that wavelength-dependent properties are modeled naturally: a parameter scan using complex-valued data $n(\lambda)$ automatically considers dispersion and wavelength-dependent absorption.

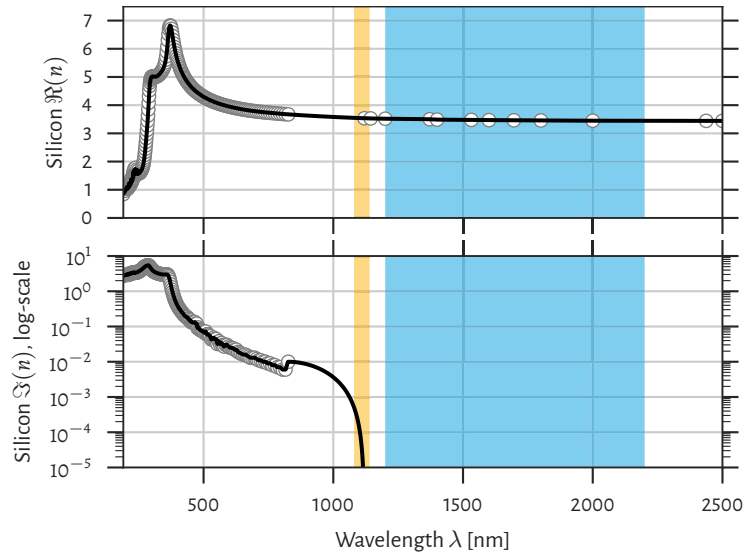


Figure 10: Refractive index properties of silicon. (Upper row) The real part of the refractive index $\Re(n)$ of silicon is shown in a broad wavelength range. Circles mark actual data points, while the black line represents the interpolated curve. (Lower row) The imaginary part of the refractive index $\Im(n)$ is shown in the same wavelength range, but using a logarithmic scale. The colored regions mark the wavelength ranges relevant for the results in chapters 5 and 6.

3.3.2 Optical properties of dielectrics and their interpolation

Unless otherwise mentioned, the nanohole array system will be treated as having the following composition: a crystalline silicon (Si) PhC slab (domain 2) on a glass substrate (domain 1) with an air superspace, including the volume inside the holes.

As a side note it is mentioned that the actual physical samples have a number of deviations from the idealized composition described above. These have mainly to do with the manufacturing process, which is based on nanoimprint lithography (NIL). Besides fabrication tolerances, the real system features an additional sol-gel layer between the glass substrate and the PhC, for example, which is neglected because of its refractive index being almost identical to the one of glass. These fabrication-related specifics are covered in section 3.5, and in more detail in [27].

Crystalline silicon is a massively investigated material and, thus, the optical properties are well documented over a large wavelength range. Figure 10 shows the real (upper plot) and imaginary (lower plot, logarithmic scale) part of the refractive index of silicon as tabulated by Aspnes [86] and Palik [87] in a large wavelength range. The circles mark points for which actual data is present, while the black lines show interpolated curves. The data is interpolated using shape-preserving piecewise cubic interpolation [88], which has no overshoots even for the non-smooth data. This is important in order to have no deviations from the actual data points, which can be the case when using spline-interpolation, for instance. In addition, figure 10 features highlighted

data ranges (yellowish, cyan), which are the relevant ranges for the results in chapters 5 and 6. It is obvious that silicon has an almost flat refractive index and is only weakly absorbing for $\lambda > 1100$ nm. For $\lambda < 500$ nm it becomes considerably absorbing and features sharp peaks in the refractive index. However, in the marked ranges of interest dispersion and absorption are almost absent.

The used glass is a Corning EAGLE XG [89], which is an alkaline earth boro-aluminosilicate glass. The data sheet provided by the manufacturer only lists refractive index data up to a wavelength of 643.8 nm. As this is below the mentioned wavelength ranges of interest, this value is assumed to be constant over the complete range, i.e. $n_{\text{glass}}(\lambda) = n_{\text{glass}}(\lambda = 643.8 \text{ nm}) = 1.5078$. This assumption is reasonable since comparable glasses, e.g. Schott N-BK7 [90], typically show a very small wavelength dependency in the considered range. The glass does not show a relevant absorption.

3.3.3 Lead sulfide quantum dots

Quantum dots (QDs) are semiconductor entities that use the quantum confinement effect to form a quasi two-level system [91, 92]. These objects of only a few nanometers in size trap the electrons in a zero-dimensional potential, so that the separation of their valence and conduction bands can be set in the fabrication process. For that reason, QDs composed of all kinds of semiconductors and with a multitude of emission wavelengths are readily available, making them well-suited as an example system for emitters on a PhC surface.

Specifically, spherical lead sulfide (PbS) QDs* were used to demonstrate fluorescence enhancement by excitation enhancement on a PhC surface, as described in chapter 6 and [42]. These QDs have a narrow diameter distribution of (5.6 ± 0.8) nm and are initially dispersed in toluene. Their surface is shielded by an oleic acid (OA) ligand to prevent particle agglomeration. The rather complex composition of these emitters, together with the coating process using the convective assembly technique† [93], necessitate to study their properties carefully in order to understand the experiments. This section will therefore comment on the fluorescence and absorption properties, as well as on the refractive index and further specifics of the final coating layer.

Fluorescence and absorption

A single QD with its oleic acid surface group is sketched on the left of figure 11. The two black lines inside the quantum dot mark the two primary energy levels (belonging to the conduction and valence bands), which define the center emission wavelength. The actual energy level structure is more complicated, causing e.g. Lorentz broadening of

* CANdots Series C org; manufactured by: Center for Applied Nanotechnology (CAN) GmbH

† Coating using the convective assembly technique was performed in the group of Prof. Dr. Tobias Kraus at INM Saarbrücken.

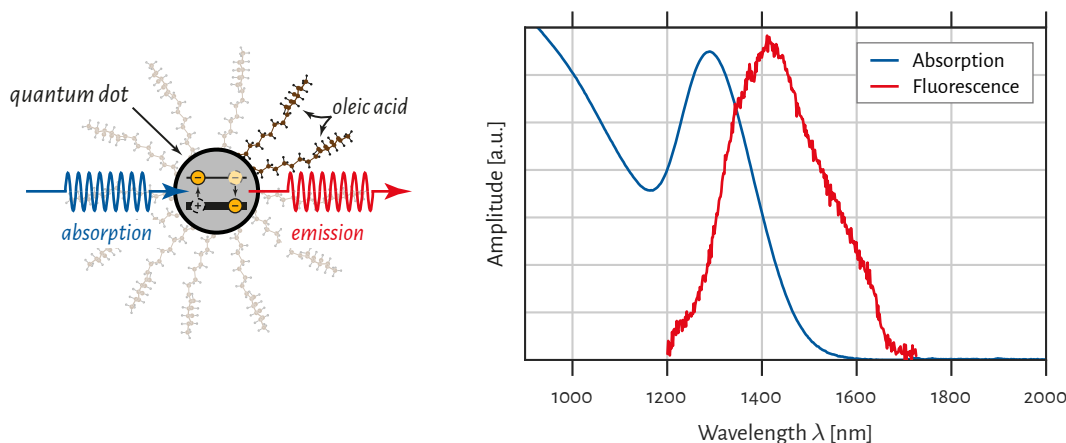


Figure 11: PbS quantum dots and their absorption and fluorescence. (Left) Sketch of a simplified PbS quantum dot with two energy levels. The arrows illustrate exciton generation by absorption (blue, electron raised to upper level) and emission by recombination (red, electron relaxes to ground level). The surface is shielded by an oleic acid ligand. (Right) The blue curve shows the measured absorption of the lead sulfide quantum dots measured using a UV-Vis-NIR spectrophotometer using QDs dispersed in toluene (normalized to pure toluene). Absolute values are omitted as they are not comparable to the considered experiments. The red curve depicts a fluorescence peak of the QDs on a planar silicon sample (without toluene).

the emission line and the ability to absorb photons in a much broader range at higher energies. The absorption (blue) of a photon generates an electron-hole pair (exciton), whose recombination leads to fluorescence (red).

On the right of figure 11 the measured absorption and fluorescence properties are shown using arbitrary units. The QDs can be pumped efficiently in a large spectral range from the visible up to about 1500 nm, while the fluorescence peak is centered at about 1400 nm. The absorption was measured using a UV-Vis-NIR spectrophotometer using the QDs in toluene (normalized to pure toluene). Although this measurement generates absolute values for the absorption, they are omitted here to avoid confusion. This is because the absolute absorption depends on e.g. the QD density and the film thickness, which differs considerably in the actual experiment compared to the absorption measurement. The fluorescence, in contrast, was measured using a thin film on a planar silicon sample, in which case the toluene is removed in the convective assembly coating process.

The expected peak shape in the simplified case of Lorentzian lines for single QDs would be a Gaussian, as the diameters are assumed to be normally distributed. However, the measured fluorescence peak shows deviations from that expectation: for shorter wavelengths a decrease in emission is observed, which is caused by an edge filter in the setup. The source of the deviations in the longer wavelength range is unknown, though they are expected to be caused by complex line broadening mechanisms. It was tried to fit the shape using a simplified model for reabsorption without

reaching a convergence. It is therefore assumed that reabsorption effects are negligible. Another factor is a possible non-Gaussian size distribution of the QDs.

Specifics of the coating layer

The coating process used for the planar silicon sample (fluorescence measurement above) is in the same way used for the PhC sample. The resulting coating is composed of PbS QDs with the OA surface group and no toluene. It is assumed that an excess of OA remains in form of free OA.

Due to the complex composition of the final coating layer the numerical model for the fluorescence enhancement experiment uses a homogenous material with an average refractive index n_{avg} (see section 6.4). Taking the arithmetic mean, the average refractive index is of the form

$$n_{\text{avg}} = \frac{1}{V_{\text{frac}}} \cdot n_{\text{PbS}} + \left(1 - \frac{1}{V_{\text{frac}}}\right) \cdot n_{\text{OA}}, \quad (3.18)$$

where $V_{\text{frac}} = V_{\text{OA}}/V_{\text{PbS}}$ is the volume fraction of the two materials, and the refractive indices at 1400 nm are known to be $n_{\text{PbS}} \approx 4.3$ [94] and $n_{\text{OA}} \approx 1.47$ [95], respectively. The manufacturer of the QDs provided data on the mass of the two constituents based on a thermogravimetric analysis, resulting in a mass fraction $m_{\text{PbS}}/m_{\text{OA}} \approx 1.928$. By identifying

$$\frac{V_{\text{PbS}} \cdot \rho_{\text{PbS}} \cdot m_{\text{PbS}}}{V_{\text{OA}} \cdot \rho_{\text{OA}} \cdot m_{\text{OA}}} = 1 \quad \implies \quad V_{\text{frac}} = \frac{m_{\text{PbS}} \cdot \rho_{\text{PbS}}}{m_{\text{OA}} \cdot \rho_{\text{OA}}} \quad (3.19)$$

the volume fraction can be derived from the known mass fraction using the tabulated volumetric mass densities, $\rho_{\text{PbS}} = 7.6 \text{ g cm}^{-3}$ and $\rho_{\text{OA}} = 0.895 \text{ g cm}^{-3}$. Inserting into equation (3.18) gives the estimate for the average refractive index

$$n_{\text{avg}} \approx 1.64 \quad (\text{PbS QDs – OA coating}). \quad (3.20)$$

As it will be outlined in section 6.4, this estimate is in very good agreement with the refractive index $n_{\text{avg,num}} \approx 1.65$ obtained by comparing simulation and measurement in a parameter scan over this parameter based on reflectance maps.

3.4 Experimental techniques

In the following sections the experimental techniques relevant for the experiments are presented, – namely the anticrossing experiment of chapter 5 and the QD fluorescence enhancement experiment of chapter 6. Specifically, it covers the angular-resolved reflectance (ARR) measurements, used in both experiments, and the actual setup that was used to measure the fluorescence enhancement of the PbS QDs on the PhC slab surface, which is only relevant for the latter experiment.

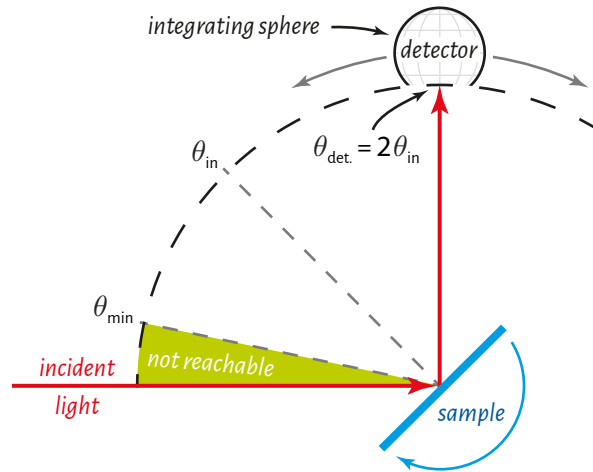


Figure 12: Sketch of the measurement configuration for the angular- and wavelength-resolved reflectance (ARR) measurements. Polarized light is incident on a tiltable sample, making an incident angle of θ_{in} with its surface normal. The directly reflected light is measured using a movable detector inside an integrating sphere at an angle of $\theta_{det.} = 2\theta_{in}$. The configuration limits the minimum incident angle to $\theta_{min} \approx 5^\circ$.

3.4.1 Angular- and wavelength resolved reflectance measurements

The angular- and wavelength-resolved reflectance (ARR) measurements have been performed using a PerkinElmer Lambda 950 spectrophotometer with an automated reflectance and transmittance analyzer accessory [96, 97]. This tool allows to measure the reflectance of a sample using linearly polarized light with a wavelength ranging from 220 nm to 2500 nm with a spot size of 4 mm \times 8 mm. The measurement configuration is sketched in figure 12. The sample can be tilted with respect to the incident beam to account for different incident angles θ_{in} . Suitable detectors are placed inside of a moveable integrating sphere with a radius of 60 mm and a rectangular entrance port of 30 mm \times 17 mm. To measure the directly reflected light from the sample, the detector angle is kept at $\theta_{det.} = 2\theta_{in}$ while varying θ_{in} in the desired range. Care must be taken when comparing these results to the ones obtained numerically (see section 3.2.4), because only the zeroth diffraction order is measured. The measurement is done separately for TE and TM polarizations. Limitations arise from the setup design for small incident angles, so that incident angles below $\theta_{min} \approx 5^\circ$ cannot be realized. The manufacturer specifies an accuracy for the sample and detector angles of 0.02° and 0.01° , respectively.

3.4.2 Measurement of the fluorescence enhancement of PbS quantum dots

The experimental setup for the measurement of the fluorescence of PbS QDs on the PhC slab surface using leaky modes is sketched in detail in figure 13* [98]. The setup had to meet the following demands:

1. Selective excitation of PhC modes by adjustability of the incident angle θ and wavelength, as well as of the different combinations of high-symmetry directions ($\Gamma - K$, $\Gamma - M$) and polarizations (TE, TM). (See figure 9 for an illustration of these parameters.)
2. Quantification of the absolute power incident on the sample.
3. Integration over all scattering angles of the emitted fluorescence light and measurement of its spectrum.
4. Automatization of incident angle and wavelength adjustment, as well as of the spectrum acquisition, for efficient and comparable scan over large parameter spaces.

A tunable IR diode laser source (SACHER Lion Series: TEC-520-1180-30) was used for the excitation, featuring a wavelength range of 1080 nm to 1140 nm and a bandwidth of about 3 nm (see chapter 6, especially figure 30 on page 100 for experimental results). The beam passes a Glan-Thompson polarizer and a $\lambda/2$ -plate for polarization adjustment, and is finally collimated before it enters the sample (greenish in the figure). The high-symmetry direction is adjusted using a proper sample orientation, while the incident angle θ is controlled using the inclination of the sample. The beam power is measured using a calibrated beam splitter and a photo detector. An integrating sphere scatters the fluorescent light into a fiber-coupled spectrometer (Ocean Optics NIR-Quest512) after passing an edge filter for laser peak removal. The angular characteristics of the integrating sphere were quantified using QDs on a planar reference sample for normalization. A microcontroller (Arduino Uno) and a MATLAB-based user interface were used to automatize the measurement for a set of high-symmetry direction and polarization, i.e. the sample inclination and the laser wavelength or adjusted automatically. Furthermore, the interface measures the spectrum and the laser power for energy normalization.

Polarization and wavelength are adjusted using a tunable IR laser source and a combination of a Glan-Thompson polarizer and a $\lambda/2$ -plate. The beam power is measured using a calibrated beam splitter and a photo detector. An integrating sphere scatters the fluorescent light into a fiber-coupled spectrometer.

In principle, the setup allows for an absolute measurement of the fluorescence, so that a quantification of the *absolute* fluorescence enhancement would be possible. However, this enforces to normalize the measurement to a planar reference with the

*Sebastian Roder of HZB installed the setup for the fluorescence enhancement experiment and performed the measurements.

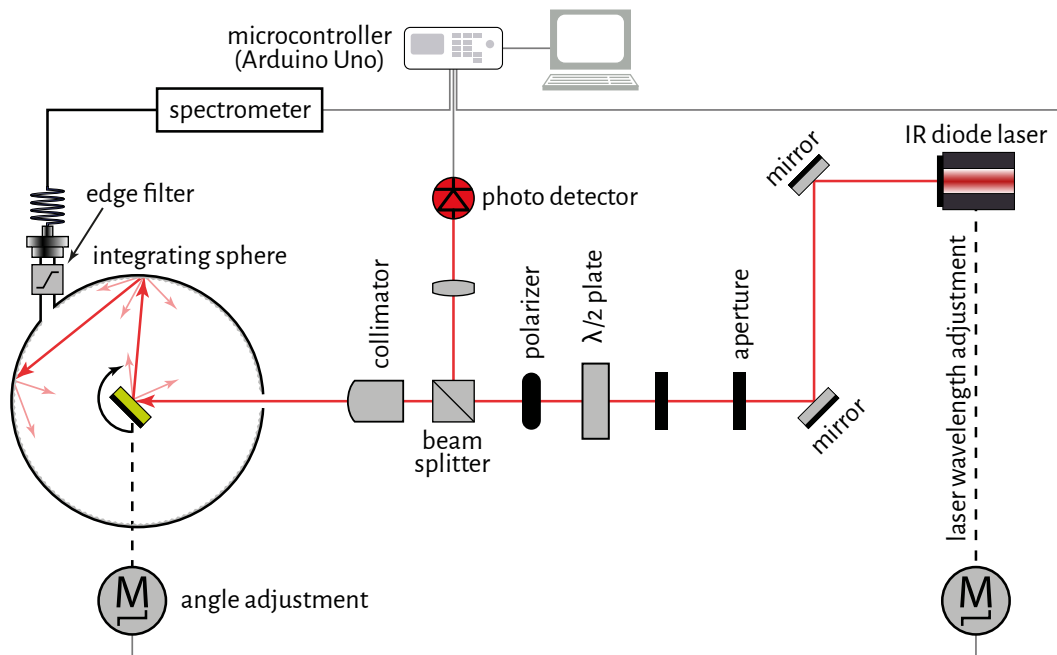


Figure 13: Experimental setup for the fluorescence enhancement measurement. The radiation (red line) of a tunable IR laser source directed onto a sample by passing a collimating and polarization-defining system. The latter is composed of an aperture, a Glan-Thompson polarizer, a $\lambda/2$ -plate and a final collimator. The beam power is measured using a calibrated beam splitter and a photo detector. The sample (greenish) resides inside an integrating sphere, so that an angle-integrated signal enters a fiber-coupled spectrometer via an edge filter. The setup is automatized using a microcontroller and step motors for spectrum read-out, and wavelength- and sample-tilt adjustment.

exact same composition and thickness of the QD coating layer, or rather to quantify the exact position on the sample. None of these prerequisites is fulfilled in the present case, as the coating layer is inhomogeneous and a measurement of the beam position on the sample was not possible. As noted in chapter 6, a minimal estimate for the fluorescence enhancement was chosen instead, by normalizing to the minimum integrated fluorescence in the final map. It is assumed that this estimation is close to the real value, because the numerical results reveal that the maps include regions far off any PhC mode. AS a sidenote, it was checked that resonantly enhanced emission does not play a quantitative role in the experimental setup by measuring the spectral distribution of emitted light. The according spectrum does not depend on the presence of the PhC.

3.5 Fabrication of photonic crystals using nanoimprint lithography

PhC slabs are often favored over 3D PhCs because of the simplicity of fabrication. The slab fabrication is basically compatible with standard complementary metal-oxide

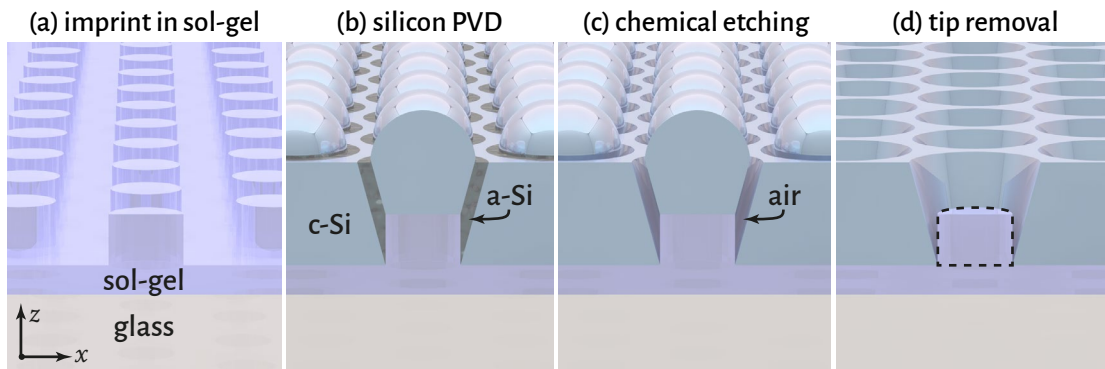


Figure 14: Fabrication process based on nanoimprint lithography (NIL). (a) The inverse of the desired geometry of the PhC is imprinted to sol-gel on glass. (b) Silicon is deposited by physical vapor deposition (PVD) and is subsequently solid phase crystallized by thermal annealing. (c) Amorphous silicon (a-Si) parts located at steep flanks of the imprinted substrate are removed by wet-chemical etching, while (d) silicon tips (and optionally the sol-gel cylinders) are removed by mechanical abrasion.

semiconductor (CMOS) technology and a variety of approaches are at hand. With electron beam lithography extremely precise structures can be achieved, but in an expensive and complex process. Optical lithography on the other hand lacks accuracy. For the samples that were used in this thesis a scalable process based on NIL [27, 99] was used, also known as nanoreplica molding. The process, which will be outlined in the following, enables to fabricate PhC slabs on large areas at low costs and is potentially compatible with mass-production. The explanations closely follow those given in [27] and omit many of the details for simplicity.

The aim of the NIL process is to replicate the inverse of a so-called master structure. This master can be fabricated using whatever technique, and can therefore benefit from the accuracy of e.g. electron beam lithography. The masters that were used in specific are $5 \times 5 \text{ cm}^2$ arrays of pillars in silicon fabricated using electron beam lithography, obtained from a commercial manufacturer (Eulitha AG, Switzerland).

As the first step of the replication process a soft stamp is prepared from poly-(dimethyl) siloxane, which can be reused multiple times. This stamp is used to imprint onto a sol-gel coated glass, effectively obtaining a replica of the initial master structure. The resulting structure is shown in figure 14(a), depicting a plan view onto a cross section of the structure. In the thermal annealing process of the sol-gel a shrinkage of the features takes place, which must be taken into account in the design of the master.

Afterwards, the sample is covered with a layer of amorphous silicon (a-Si) by physical vapor deposition (PVD) and is thermally annealed in a solid phase crystallization process. Figure 14(b) depicts the resulting structure of crystalline silicon (c-Si) pillars. At the steep flanks of the structure the crystallization is suppressed, as indicated by the residual amorphous silicon parts in the figure [100]. In a selective wet-chemical etching step, these amorphous parts are removed, leading to the composition illustrated

in figure 14(c). The silicon tips that reside on the sol-gel cylinders can be removed by mechanical abrasion, i.e. by rubbing them off using an appropriate wipe and subsequent rinsing with deionized water. The final PhC structure is shown in figure 14(c). Depending on the thickness of the silicon layer the sol-gel cylinders are removed in this process as well, as indicated by the blue dashed line in the figure.

4

Convergence and Performance of Finite Element Simulations

AS FOR ANY NUMERICAL TECHNIQUE, the most crucial point when using the finite element method is to be certain of the convergence of the computation and, hence, the accuracy of the results. This demand sounds natural in the first place, but for real-world problems it can be a challenging and often time-consuming task.

It is the aim of this chapter to demonstrate how the convergence of the simulations presented in later chapters was studied and to prove that the denoted accuracy was reached. To this end, after an explanation of the terms convergence and performance, three systems will be studied in detail, which are

1. Fresnel refraction on a flat interface between two dielectrics,
2. Mie scattering on a dielectric sphere in air, and
3. the nanohole array of section 3.2 as a real-world system.

The choice of these systems aims at a logical line of reasoning, which is necessary to make the final thoughts on the accuracy of the real-world system perfectly clear. The first system – the flat interface of two dielectrics – is exactly representable in the finite element mesh as it does not contain any roundings. Moreover, the reflectance and transmittance for this system can be calculated using an exact analytical reference: the Fresnel equations. In the second step, Mie scattering will be studied – another system for which an exact analytical reference solution exists. But in contrast, this system contains a sphere, i.e. roundings, and is not exactly representable using the finite element mesh. The necessary simplifications will be introduced and the influence of the controlling parameters will be studied.

For the previously mentioned two systems the convergence and, in consequence, the accuracy of the derived results can be assessed in an exact way by comparing to

the analytical solution. Using these examples the convergence of the finite element method will be demonstrated in detail and the parameters on which it depends will be studied. In the final step, when analyzing the nanohole array, an analytical solution will be absent and the knowledge from the former systems will be applied to reach a satisfying level of certainty of the convergence properties nonetheless.

Finally, it will be shown that the convergence analysis is not only a necessary task to obtain scientifically relevant results, but also a tool to find a performance optimum of the simulation parameters. That is a set of input parameters that guarantees a specifically chosen accuracy, while causing minimum computational costs – which in the end is CPU time and memory usage.

4.1 Notes on terminology

The terms convergence and performance are both ambiguous. In the context of this work, the term “converged” is used to describe a simulation with well-defined uncertainty of specific quantities. This concept is known as goal-oriented error estimation [101–103], in contrast to the more rigorous approach of measuring the error of the approximation of the near-field itself. In this sense, when studying the convergence properties of a specific simulation setup, the task is to measure the deviation of the quantities of interest from a suitable reference solution, – in other words to achieve certainty on the accuracy of these quantities.

Another requirement, which is more related to practice, is to reach a target accuracy, in the above sense, using minimum computational costs. This is what will be called “performance” in the scope of this thesis. To find a performance optimum for a specific simulation setup, one basically needs to answer three questions, which are

1. What is the accuracy measure?
2. What is the target accuracy?
3. What is the performance measure?

The *accuracy measure* is usually the average or maximum relative deviation of the quantities of interest from the reference solution. The target accuracy can be chosen freely and may depend on external demands such as experiments.

For the *performance measure* it may seem obvious at first glance to use the accumulated CPU time, as time is usually the demanding factor. But this measure would depend on the system on which the computation is executed, so that it underlies fluctuations and is not comparable among systems. A better choice is the *number of unknowns*, as it is a fixed quantity for a simulation setup and is proportional to the CPU time. Also, the number of unknowns is connected to the total memory consumption, which can be another restricting quantity.

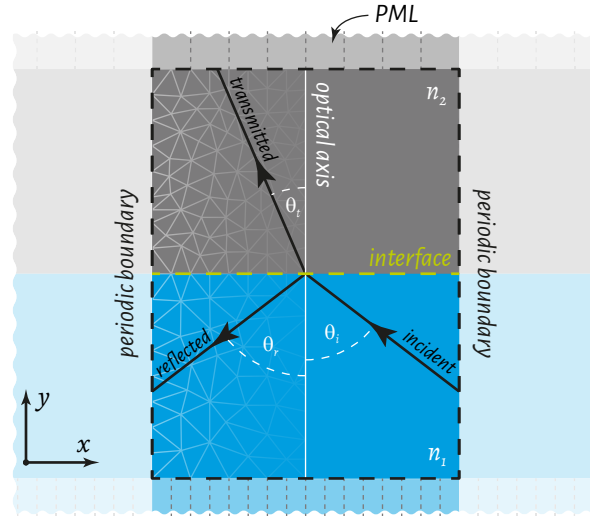


Figure 15: Computational setup of the Fresnel refraction simulation. Two dielectric half-spaces with refractive indices n_1 (dielectric 1, blue) and n_2 (dielectric 2, gray) meet at an interface (green, dashed). Black arrows mark an exemplary incident ray (plane wave) with incident angle θ_i and the reflected and transmitted rays and their respective reflected and refracted angles θ_r and θ_t . The black dashed line marks the computational domain with its periodic and transparent (PML) boundaries.

4.2 Fresnel refraction

One of the most simple scenarios that can be treated in a 2D-finite element simulation is refraction on a flat dielectric interface. In this simulation a plane wave is incident to an interface between two homogeneous, non-magnetic, non-absorbing media with real-valued refractive indices n_1 and n_2 . Figure 15 depicts a sketch of such a system with dielectric 1 in blue and dielectric 2 in gray. The black dashed line marks the computational domain in which the near-fields are solved. The boundaries of this domain are periodic in the $\pm x$ -directions and perfectly matched layers (PMLs) in the $\pm y$ -directions, therefore modeling a system of two dielectric half-spaces. The figure also indicates a typical mesh.

A plane wave is incident from dielectric 1 and makes an angle θ_i with the normal of the interface, i.e. the optical axis. Depending on the dielectric materials and the incident angle a part of the light will be reflected under angle $\theta_r = \theta_i$ (law of reflection), and another part will be transmitted under the refraction angle θ_t , related to the incident angle by Snell's law via $n_1 \sin \theta_i = n_2 \sin \theta_t$.

4.2.1 Analytical solutions

The reflectance R and transmittance T , which are the fractions of the incident energy that are reflected and refracted from/by the interface, are given by the Fresnel equations. In the case of non-magnetic, non-absorbing materials, the transmittance can

always be calculated from the reflectance by

$$T = 1 - R. \quad (4.1)$$

The reflectance depends, along with the incident angle θ_i , on the polarization of the plane wave, for which it is sufficient to consider the two perpendicular cases of transverse-electric (TE)- and transverse-magnetic (TM)-polarization (compare section 2.2.6). After elimination of the dependent angles the Fresnel equations are

$$R_{\text{TE}}(\theta_i) = \left| \frac{n_1 \cos \theta_i - n_2 \sqrt{1 - \left(\frac{n_1}{n_2} \sin \theta_i\right)^2}}{n_1 \cos \theta_i + n_2 \sqrt{1 - \left(\frac{n_1}{n_2} \sin \theta_i\right)^2}} \right|^2, \quad (4.2)$$

$$R_{\text{TM}}(\theta_i) = \left| \frac{n_1 \sqrt{1 - \left(\frac{n_1}{n_2} \sin \theta_i\right)^2} - n_2 \cos \theta_i}{n_1 \sqrt{1 - \left(\frac{n_1}{n_2} \sin \theta_i\right)^2} + n_2 \cos \theta_i} \right|^2. \quad (4.3)$$

These are the analytical reference equations for the reflectance and transmittance, which are quantities that can be computed using Fourier transform post-processes in the finite element simulation.

4.2.2 Simulation setup, mesh parameters and quantity calculation

The simulation setup uses two plane wave sources for TE- and TM-polarization, respectively, as described in section 3.2.3, incident from $-y$ -direction under angle θ with respect to the optical axis. For each of the two materials, i.e. domains in the layout, a different side length constraint (SLC) is set for the triangles of the mesh (the terms “maximum side length” and SLC will be used synonymously). These are two independent parameters for the meshing which might be optimized separately. However, once the number of materials grows in a simulation, the number of parameters for the optimization will increase drastically, causing the number of necessary simulations for a convergence optimization parameter scan to become inconvenient. Referring to the approximate rule for maximum patch sizes defined in equation (3.5), we introduce the more general parameter “side length constraint to wavelength ratio” $n_{\text{domain}} \cdot \text{SLC}/\lambda_0$, where n_{domain} is the refractive index in the given domain and λ_0 the vacuum wavelength of the light source. We will refer to this quantity by the short form “SLC/ λ -ratio”.

According to the mentioned rule (3.5) it is assumed that an SLC/ λ -ratio of 1 is sufficient to reach a satisfying convergence, but it will be shown shortly that smaller values may be useful to reach a better performance. Figure 16 shows the meshes of the Fresnel refraction system for SLC/ λ -ratio values of 0.8, 0.5 and 0.2 for an “air-glass” interface

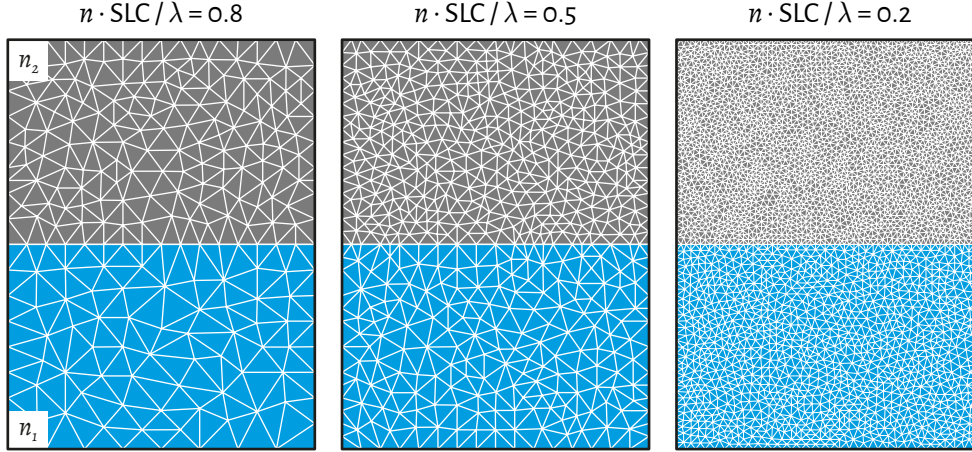


Figure 16: Example meshes for the Fresnel refraction simulation as a function of the SLC/λ -ratio. The three meshes for SLC/λ -ratio of 0.8, 0.5 and 0.2 show how the patch sizes are automatically adjusted for the different materials with refractive indices n_1 and n_2 .

($n_1 = 1.0, n_2 = 1.5$). Reducing the SLC/λ -ratio leads to an overall finer mesh while automatically setting a smaller patch size in the high-index material. That way the relevant parameters controlling the meshing are reduced to only one parameter.

To calculate the reflectance and transmittance numerically, we use two Fourier transforms to calculate the reflected and transmitted diffraction orders, so in this case in $-y$ - and $+y$ - direction, respectively. The Fourier transforms give the electric field components \mathbf{E}_i for each diffraction order i from which the energy flux densities in the normal directions of each case can be computed using the time-averaged Poynting vector $\bar{\mathbf{S}}(\mathbf{r}, t)$ given in equation (2.21). We find the reflectance and transmittance by summing over the normal components of $\bar{\mathbf{S}}_i$ for each diffraction order i and normalizing to the energy of the incident plane wave P_{in}

$$\mathcal{C} = \frac{\sum_i \bar{\mathbf{S}}(\mathbf{r})_i \cdot \mathbf{n}_C}{P_{in}}, \quad \mathcal{C} \in \{R, T\}, \quad (4.4)$$

with the normal vectors $\mathbf{n} = \mp \hat{\mathbf{e}}_y$ for R and T , respectively.

4.2.3 Convergence analysis

The Fresnel refraction system is a flat interface, i.e. there are no corners or roundings, which means equation (3.4) is valid and the error should decrease exponentially when increasing the polynomial degree p , assumed that the mesh is fine enough. Consequently, this system is most suitable to benchmark this proportionality and the general rule on the maximum patch side length for propagation problems. Any adaptivity or refinement technique as described in section 3.1.5 is thus deactivated, which is referred to as the “plain FEM” in the following.

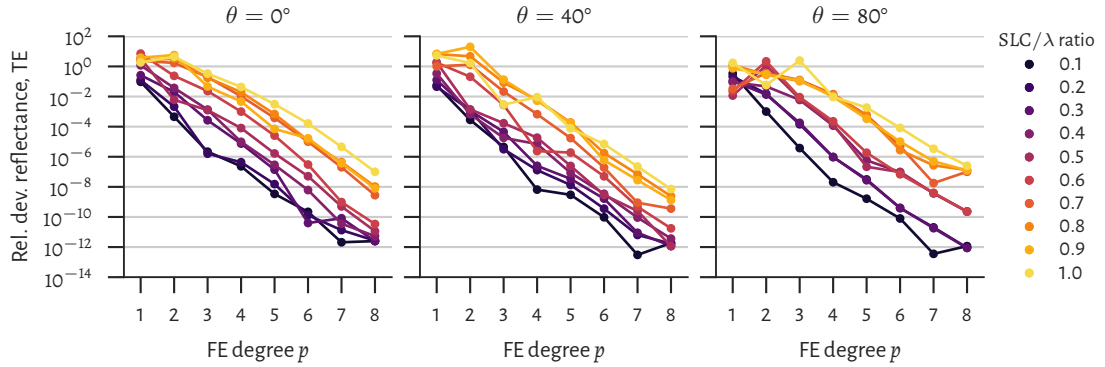


Figure 17: Convergence study of the Fresnel refraction simulation. The relative deviation of the reflectance from the analytical reference solution (TE-polarization) is shown for three different incident angles $\theta = 0^\circ$, $\theta = 40^\circ$ and $\theta = 80^\circ$ (columns) as a function of the finite element polynomial degree p . Different colors represent different values of the adaptive meshing parameter SLC/λ -ratio, given by the legend at the right.

To this end, the system was solved using the “air-glass”/TE case ($n_1 = 1.0$, $n_2 = 1.5$) for a number of FE degrees p and SLC-ratios. Further, as the normal use-case is to optimize a simulation setup for a parameter scan, we suppose that we want to scan over the incident angle θ from 0° to 80° in the end. So we also do these calculations for three different values of θ in the center and at the boundaries of this interval (as we assume a relatively flat behavior). For each solve, the reflectance is computed and compared to the analytical value by calculating the relative deviation $|R_{\text{num.}}/R_{\text{ana.}} - 1|$.

Figure 17 shows the results of this parameter scan. When considering one incident angle θ at a time, i.e. column in the figure, it is clearly seen that an increase in the FE degree p exponentially decreases the deviation (which is linear in the semi-logarithmic plot). This observation approximately holds for all SLC/λ -ratios and all incident angles. Shallower angles (e.g. $\theta = 80^\circ$) lead to stronger discrepancies from this behavior if the grid is coarse. As it is expected from equation (3.4), a finer mesh (color-coded) causes an offset in the exponential decrease. Moreover, from the figure it can readily be seen that, e.g. for normal incidence, a FE degree of $p = 5$ is needed to reach an accuracy of 10^{-2} if only one patch per wavelength is used, i.e. $\text{SLC}/\lambda = 1$; while $p = 2$ is sufficient for $\text{SLC}/\lambda = 0.1$, i.e. ten patches per wavelength. Similar conclusions can be drawn from the plots for the other incident angles.

In summary, the error proportionality relation, equation (3.4), is fulfilled satisfactory and the FEM solver reaches errors as small as 10^{-12} with minimal numerical effort for such simple, well-behaved systems. Furthermore, it was shown that the parameter space can be reduced by using the SLC/λ -ratio and that the approximate rule of equation (3.5) can be used to find reasonable test values. In the next step, a system which can not be represented accurately in the mesh will be studied to see the limitations that arise from this fact.

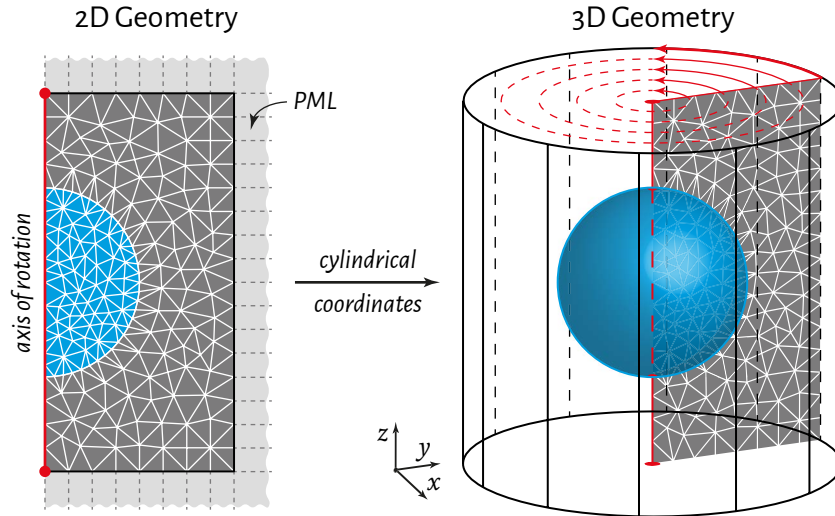


Figure 18: Computational setup of the Mie scattering simulation. (Left) The *actual* 2D mesh composed of a semicircle (dielectric material, blue) surrounded by air (gray) in a rectangular computational domain. The axis of rotation is marked using a red line. Perfectly matched layers (PMLs) are used on the other boundaries. The right part shows the *virtual* 3D geometry achieved by using cylindrical coordinates. Dashed lines depict hidden or rear lines. The 2D mesh used for rotation is shown as an inset.

4.3 Mie scattering

As it was stated in the previous sections, the exact physical geometry plays a major role for the actual accuracy of the FEM. The two dominating factors are the existence of (i) sharp features limiting the accuracy subject to equation (3.6) and (ii) roundings which can only be represented by approximation in a prismatic mesh.

To study the effects of (ii), which is of main importance in the final real-world cylindrical/conical nanohole array, Mie scattering is considered in this section, which is scattering of plane waves by a homogenous sphere and hence a fully three-dimensional problem. The 3D mesh is obtained from a rotation of a primitive 2D mesh, as described in section 3.1.6.

The simulation setup is sketched in figure 18, the left part showing the actual mesh composed of a semicircle in a rectangular computational domain. The axis of rotation is marked using a red line. Transparent boundary conditions (section 3.1.3) are used on each of the other boundaries to simulate a sphere in an infinite, homogenous medium with refractive index $n = 1$. The solver uses cylindrical coordinates, which virtually causes a 3D geometry as depicted in the right part of the figure. The virtual outline of the computational domain is therefore a cylinder. The initial mesh is shown as an inset and the red line again marks the axis of rotation (red arrows denote how the plane is rotated). The sphere is illuminated from +z-direction using TE polarization and a fixed vacuum wavelength of $\lambda_0 = 550$ nm.

4.3.1 Analytical solutions

The analytical solutions for light scattered on spherical objects depend on the radius-to-wavelength ratio r/λ of the sphere and the incident plane wave. The Mie solution is valid for specific ratios for which Mie resonances occur, causing the scattering to be particularly strong or weak. Other solutions are e.g. Rayleigh scattering for very small particles $r \ll \lambda$, the Rayleigh–Gans approximation, or the anomalous diffraction approximation of van de Hulst.

For the present system the Mie solution is valid and the presented formulae are geared to the derivation given by Bohren & Huffman [104]. The established quantities of interest to describe the scattering process are efficiencies Q_i , in this case the scattering efficiency Q_{sca} , the absorption efficiency Q_{abs} and the extinction efficiency Q_{ext} . These are cross sections σ_i normalized to the cross section of the sphere $A = \pi r^2$, i.e.

$$Q_i = \frac{\sigma_i}{\pi r^2}. \quad (4.5)$$

We introduce the size parameter $x = kr$, where r is the radius of the non-magnetic sphere and $k = 2\pi/\lambda_0$ the wave number in vacuum. The analytical equations for the efficiencies depend on the coefficients

$$a_N = \frac{n^2 j_N(nx) [x j_N(x)]' - j_N(x) [n x j_N(nx)]'}{n^2 j_N(nx) [x h_N^{(1)}(x)]' - h_N^{(1)} [n x j_N(nx)]'}, \quad (4.6)$$

$$b_N = \frac{j_N(nx) [x j_N(x)]' - j_N(x) [n x j_N(nx)]'}{j_N(nx) [x h_N^{(1)}(x)]' - h_N^{(1)} [n x j_N(nx)]'}. \quad (4.7)$$

Here, primes mark derivatives and $j_N(z)$ are the spherical Bessel functions and $h_N^{(1)}(z)$ the spherical Hankel functions of order N . These are themselves given by the Bessel functions of first and second kind J_M and Y_M , respectively, thus

$$j_N(z) = \sqrt{\frac{\pi}{2z}} J_{N+0.5}(z), \quad (4.8)$$

$$h_N^{(1)}(z) = j_N(z) + i y_N(z), \quad \text{with} \quad y_N(z) = \sqrt{\frac{\pi}{2z}} Y_{N+0.5}(z). \quad (4.9)$$

Finally, the scattering and extinction efficiencies are given by

$$Q_{\text{sca}} = \frac{2}{x} \sum_{N=1}^{\infty} (2N+1) (|a_N|^2 + |b_N|^2), \quad (4.10)$$

$$Q_{\text{ext}} = \frac{2}{x} \sum_{N=1}^{\infty} (2N+1) \Re(a_N + b_N) \quad (4.11)$$

while Q_{abs} can be calculated from the energy conversion

$$Q_{\text{abs}} = Q_{\text{ext}} - Q_{\text{sca}}, \quad (4.12)$$

which also holds for the cross sections. Equations (4.10) to (4.12) are used to calculate the analytical reference values for the efficiencies, while infinite series can be truncated at $N_{\text{max}} = x + 4x^{1/3} + 2$ (compare to [104]). Effectively, the open source python package `pymiecoated` is utilized which already implements the described equations.

4.3.2 Mesh parameters and numerical quantity calculation

As stated above, the simulation setup de facto uses a 2D mesh as shown in the left part of figure 18. Just as for the Fresnel refraction simulation, we thus introduce the SLC/λ -ratio to automatically adjust the patch sizes for the different materials and to use a dimensionless quantity. Further, the refine all circle (RAC) parameter is used to control the number of edges of the polygon which represents the circle, as explained in section 3.2.2 and equation (3.8). This is a crucial new feature compared to the Fresnel system, where the geometry has been represented by the mesh without any approximations.

Figure 19 shows the same detail of the mesh for different combinations of RAC and the SLC/λ -ratio. For $\text{RAC} = 2$, i.e. $N_p = 16$ edges (left column), the circle representation is very rough and the patch sizes in the region of the circumference are dominated by the SLC/λ -ratio. In contrast, for $\text{RAC} = 6$, which are $N_p = 256$ edges (right column), the mesh becomes extremely fine at the circumference even for very low settings of the SLC/λ -ratio. An accurate circle representation can thus lead to a strong increase in the total number of mesh elements.

To calculate the efficiencies Q_{abs} , Q_{sca} and Q_{abs} we utilize two post processes provided by JCMSuite: (i) a density integration over the electric field energy density \bar{w}_e (equation (2.18)) and (ii) a flux integration over the electromagnetic field energy flux density, i.e. the Poynting vector defined in equation (2.21), for the flux of the scattered field from the computational domain into the exterior domain.

For the first case, the post process yields the total (complex-valued) electric energy

$$\widehat{W}_e^j = \int_{V_j} \bar{w}_e \, dV_j$$

for each domain j with volume V_j . As outlined in section 2.1.2 and equations (2.25) and (2.26) the absorption in a volume V can be obtained from the imaginary part of the electric energy. The absorption cross section of the sphere can in consequence be obtained from the computed electric energy in the related domain, i.e.

$$\sigma_{\text{abs,num.}} = -\frac{\omega}{Z_0} \Im \left(\widehat{W}_e^{\text{sphere}} \right), \quad (4.13)$$

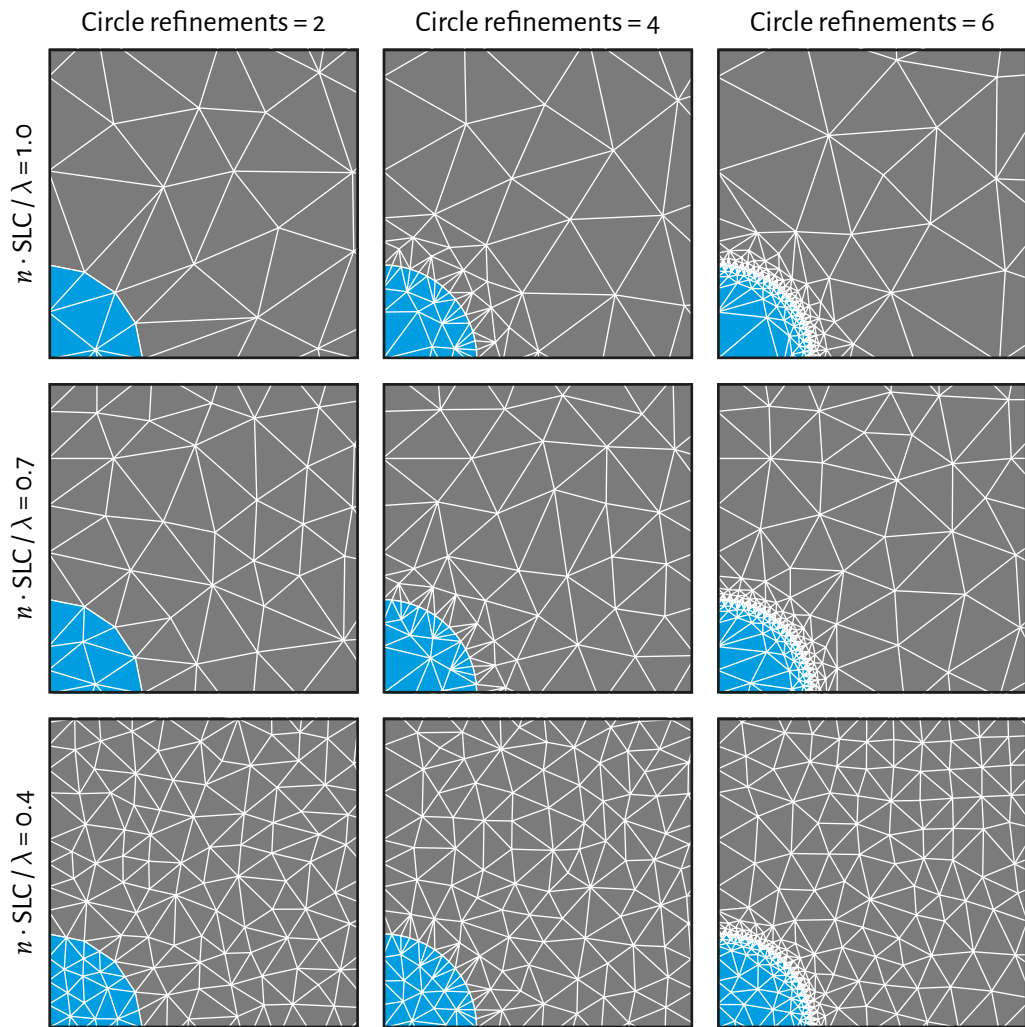


Figure 19: Example meshes for the Mie scattering simulation as a function of SLC / λ -ratio and circle refinements RAC. Each of the nine images shows the same detail of the finite element mesh, depicting parts that correspond to the sphere in blue and the air surroundings in gray (compare figure 18). The adaptive meshing parameter SLC / λ -ratio is varied across the **rows**, while the refine all circle (RAC) parameter is varied across the **columns**.

with the vacuum impedance Z_0 defined in equation (2.8). Secondly, the flux integration post process yields the electromagnetic energy flux of the scattered field

$$\Phi = \int_S \bar{\mathbf{s}} \cdot d\mathbf{f},$$

where S is the surface of the computational domain boundary and $d\mathbf{f}$ is the surface element. As for the absorption cross section, the scattering cross section is given by

$$\sigma_{\text{scat,num.}} = \frac{1}{2Z_0} \Re(\Phi). \quad (4.14)$$

Finally, because of the energy conservation the extinction cross section is given by

$$\sigma_{\text{ext,num.}} = \sigma_{\text{abs,num.}} + \sigma_{\text{scat,num.}}$$

4.3.3 Convergence analysis

To analyze the convergence properties of the Mie scattering system we proceed in the same way as we did for the Fresnel example in section 4.2. The plain FEM will be used to analyze the accuracy of the scattering efficiency Q_{sca} as a function of (i) the FE degree p , (ii) the SLC/ λ -ratio and (iii) the number of circle refinements RAC. We define the use case for which the optimization should be performed as a parameter scan over the sphere radius r from $0.3 \mu\text{m}$ to $0.5 \mu\text{m}$.

Figure 20 shows the results of the convergence parameter scan. Again, as in the Fresnel example, radii samples were taken at the bounds and in the center of the total range, i.e. $r \in \{0.3, 0.4, 0.5\} \mu\text{m}$. Each radius is represented by a column in figure 20, representing an individual parameter scan over the convergence parameters (i)-(iii). The number of circle refinements RAC is varied across the rows, taking values from 3 to 7. The SLC/ λ -ratio is color-coded and the relative deviation of the computed scattering efficiency from the analytical reference is plotted versus p – making the individual plots comparable to the plots in figure 17.

If we concentrate on a single column, e.g. for $r = 0.5 \mu\text{m}$ and start with the case $\text{RAC} = 7$, the situation is comparable to the one in figure 17 up to $p \approx 4$. The accuracy scales exponentially with increasing p , while refining the mesh influences the offset and gradient. However, for larger values of p the deviation saturates at about 10^{-5} . This is many orders of magnitude worse compared to the Fresnel system, which reached 10^{-12} for these values of p and SLC/ λ -ratio!

If we move up in the same column to smaller values of RAC, the saturation occurs for smaller and smaller values of p and the accuracy drops – saturating already at about $5 \cdot 10^{-3}$ for $\text{RAC} = 3$. So we observe that the quality of the representation of roundings drastically limits the maximally achievable accuracy, making the RAC the most prominent mesh convergence parameter in this setup. Comparing the columns between each other reveals the same tendencies for each of the radii, with only minor differences in the saturation values and some fluctuations.

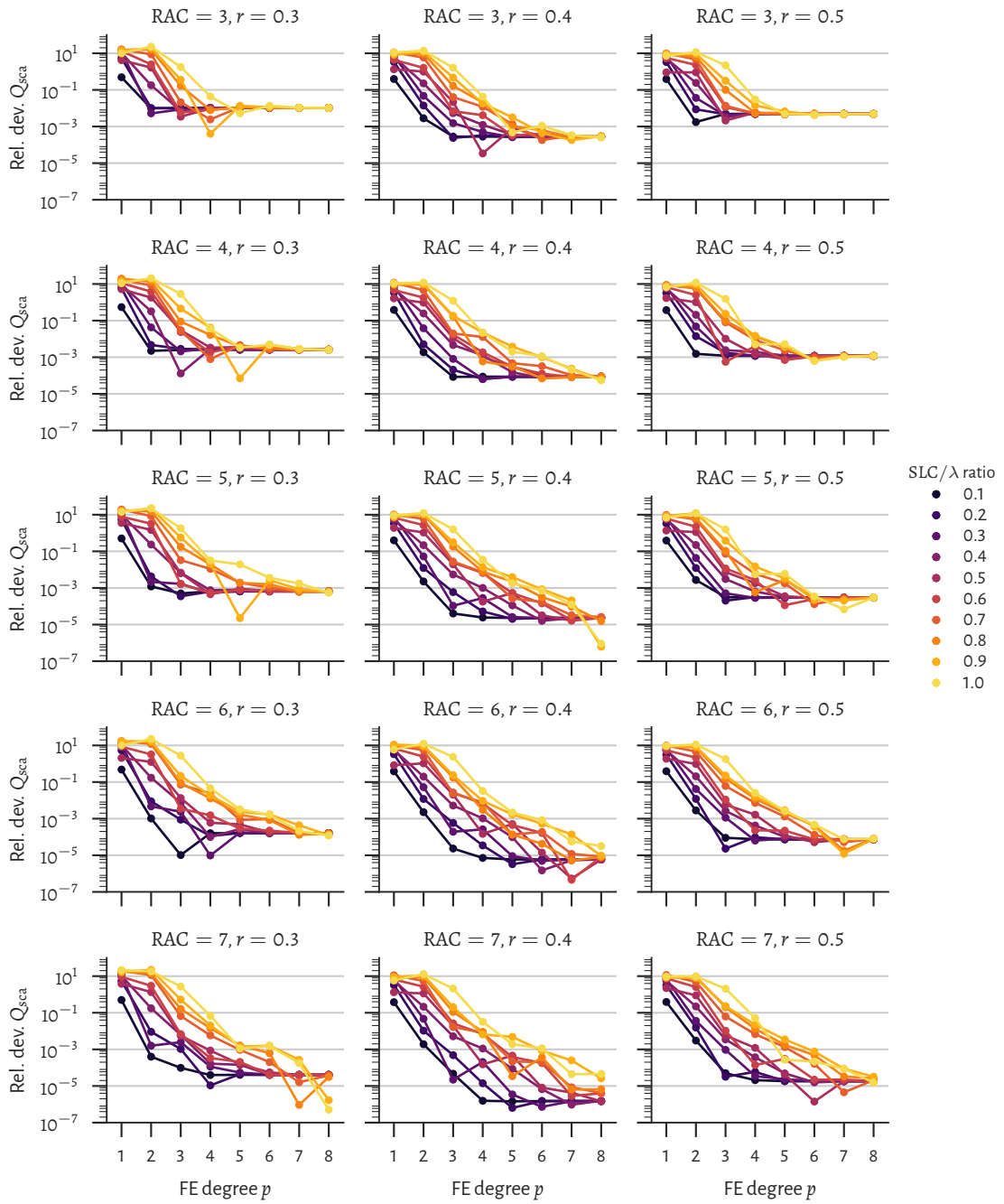


Figure 20: Convergence study results of the Mie refraction simulation. The relative deviation of the scattering efficiency Q_{sca} from the analytical reference solution is shown for different sphere radii (**columns**) and refine all circle (RAC) values (**rows**) as a function of the finite element polynomial degree p . Different colors represent different values of the adaptive meshing parameter SLC/λ -ratio, given by the legend at the right.

Input parameters			Output quantities		
FE degree p	SLC/ λ -ratio	RAC	Mem. (GB)	# Unknowns	Rel. dev. Q_{sca}
5	0.6	5	0.48	35676	4.69e-04
5	0.5	5	0.50	43129	5.97e-04
5	0.6	6	0.51	48747	3.20e-04
6	0.7	6	0.62	63919	4.24e-04
4	0.3	5	0.53	65429	3.68e-04
4	0.3	6	0.55	74510	1.11e-04

Table 4.1: The six optimum configurations of the Mie scattering performance optimization with a target accuracy of 10^{-3} . The configurations, defined by their input parameters finite element polynomial degree p , adaptive meshing parameter SLC/ λ -ratio and refine all circle (RAC), are listed together with their computational costs (memory in gigabytes and number of unknowns) and precision, represented by the mean relative deviation of the scattering efficiency Q_{sca} for all radii. The rows are sorted in ascending order with respect to the number of unknowns, which acts as the performance measure.

4.3.4 Performance optimization

It is now the task to find the performance optimum from all the configurations varied in the convergence parameter scan (see section 4.1 for a definition of performance and additional explanations). A target accuracy of 10^{-3} is chosen. The accuracy measure in this case is the relative deviation of Q_{sca} , as this quantity is computed using a flux integration process, while Q_{abs} is derived from a density integration. The integrand in the density integration is a scalar vector field, while for the flux integration it is a 3-vector field. It is expected that the larger number of uncertain values in the flux integration enlarges the overall uncertainty. In the specific use case, the accuracy should be reached in the complete range of radius values. We thus take the average deviation of Q_{sca} for the three sample radii, so that the accuracy measure is in fact the mean relative deviation of the scattering efficiency. A more restrictive possibility would be to take the maximum deviation.

If we restrict the results to those which meet the accuracy criterium defined above, we can sort them for the number of unknowns in ascending order. The best six configurations together with their computational costs and accuracies are listed in table 4.1. The optimum configuration uses $p = 5$, SLC/ $\lambda = 0.6$ and RAC = 5 and reaches a mean accuracy of $4.69 \cdot 10^{-4}$. When comparing to the second best configuration, which uses a slightly finer mesh, the optimum uses about 18 % less unknowns, less memory, but reaches a higher accuracy.

In order to benchmark the approach the system is solved for 100 radii from $0.3 \mu\text{m}$ to $0.5 \mu\text{m}$, the efficiencies are calculate and compared to the analytical values. The results of this parameter scan are shown in figure 21, showing the numerically obtained values for the efficiencies in the upper panel, and the related relative deviations be-

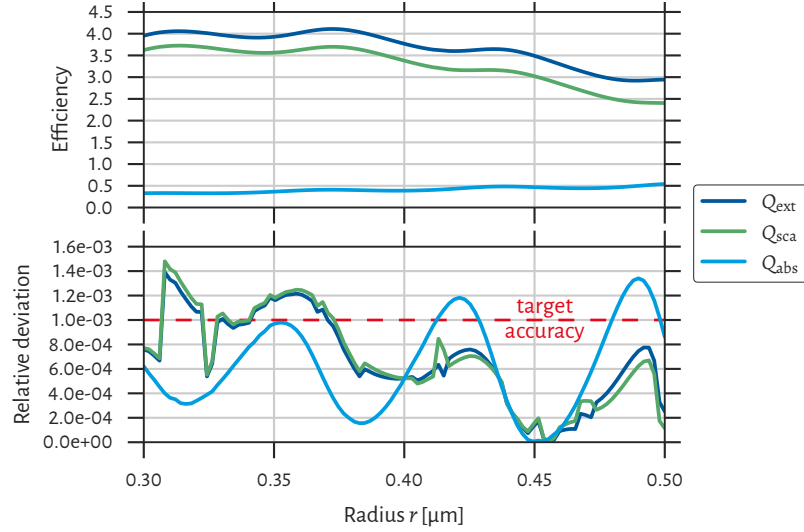


Figure 21: Calculated efficiencies and relative deviations using the performance optimized configuration. (Upper row) Numerically obtained values for the extinction efficiency Q_{ext} (blue), scattering efficiency Q_{sca} (green) and absorption efficiency Q_{abs} (cyan) as a function of the sphere radius r . **(Lower row)** Relative deviations from the analytical values for the same quantities as before and using the same colors. The target maximum deviation is marked using a red dotted line.

low. The target maximum deviation is marked using a red dotted line. The quantities show a relatively flat behavior, so that drastic effects are not expected from a physics point of view. However, the relative deviations show oscillations and the maxima do not align with the sample radii. Also, for radii $> 0.4 \mu\text{m}$ the deviation of Q_{abs} is in fact dominating, which is not expected from the reasoning given above. Another interesting observation is that the deviation of this quantity behaves more smoothly than the one that is derived from the flux integration post process. Such unexpected results highlight the importance of a detailed convergence study and the necessary awareness when working with complex numerical techniques in general. In total, however, the target accuracy is reached satisfactory: it is not exceeded by more than 40 % and the majority of points lies below.

4.4 Nanohole array

The “simple” systems previously discussed showcased the abilities and limitations of the finite element method (FEM) which are relevant for scattering simulations in general – but also in particular for the primarily studied system of this thesis: the nanohole array. This system is a photonic crystal (PhC) slab consisting of a hexagonal-lattice pattern of nanometer-sized, possibly conically-shaped holes on a planar substrate. Not only is this system physically far more complex than the Fresnel and Mie systems, but it also lacks a rigorous analytical reference solution. This situation becomes even harder

if material specific phenomena like for example dispersion and wavelength-dependent absorption should be considered. Nevertheless, in the following it will be shown that the knowledge gained from the simple systems, together with the error estimation-based techniques implemented in JCMSuite (see section 3.1.5), can indeed suffice to achieve certainty about the convergence characteristics.

4.4.1 System geometry, mesh parameters and quantities

A detailed description of the nanohole array system is given in section 3.2, considering specifics on geometry 3.2.1, meshing 3.2.2, illumination 3.2.3 and the physical quantities of interest and their derivation 3.2.4. In consequence, the generalities will not be repeated here, but rather completed with details specific to the convergence analysis.

The 3D geometry introduces new aspects that need to be taken care of for an accurate meshing – especially because the mesh is generated via extrusion from a primitive 2D mesh. Some general explanations regarding the extrusion based meshing have been given in section 3.1.6. Note also figure 9 on page 49 which shows example meshes for the nanohole array and illustrates meshing parameters which are considered in the following.

For the primitive 2D mesh the same techniques as for the Mie system are used in view of the setting of the number of circle refinements RAC and the SLC/λ -ratio. However, when extruding in z -direction the spacing between adjacent layers must be chosen wisely, which is controlled by setting specific spacing parameters for each layer (these are the extrusion layers L_1 , L_2 and L_3 in figure 9, bottom, center). Minimally, the z -spacing must be limited to the maximum side length of the highest-index material in the current extrusion layer. This causes an overhead in the number of elements – and therefore in the number of unknowns – compared to a full-3D mesh, because the lower-index domains are meshed too finely in z -direction.

Moreover, the number of circle refinements must be taken into account, since the polygon that represents the circle can cause very small triangles near the circumference. Since there is no control parameter implemented in JCMSuite to avoid elements with high aspect ratios, an additional parameter is introduced, which will be denoted as “maximum z -ratio”, i.e. the ratio between the extent in z -direction and the in-plane extent of the elements: $z\text{-ratio} = l_z/l_{ip}$. These two extents are marked in the isometric example mesh of figure 9 (bottom, right). For an estimation of the minimum in-plane extent the side length of the polygon representing the circle $l_{ip} \approx 2r \sin(\pi/N_p)$ is considered, where r is the circle radius and N_p is given by equation (3.8). In consequence,

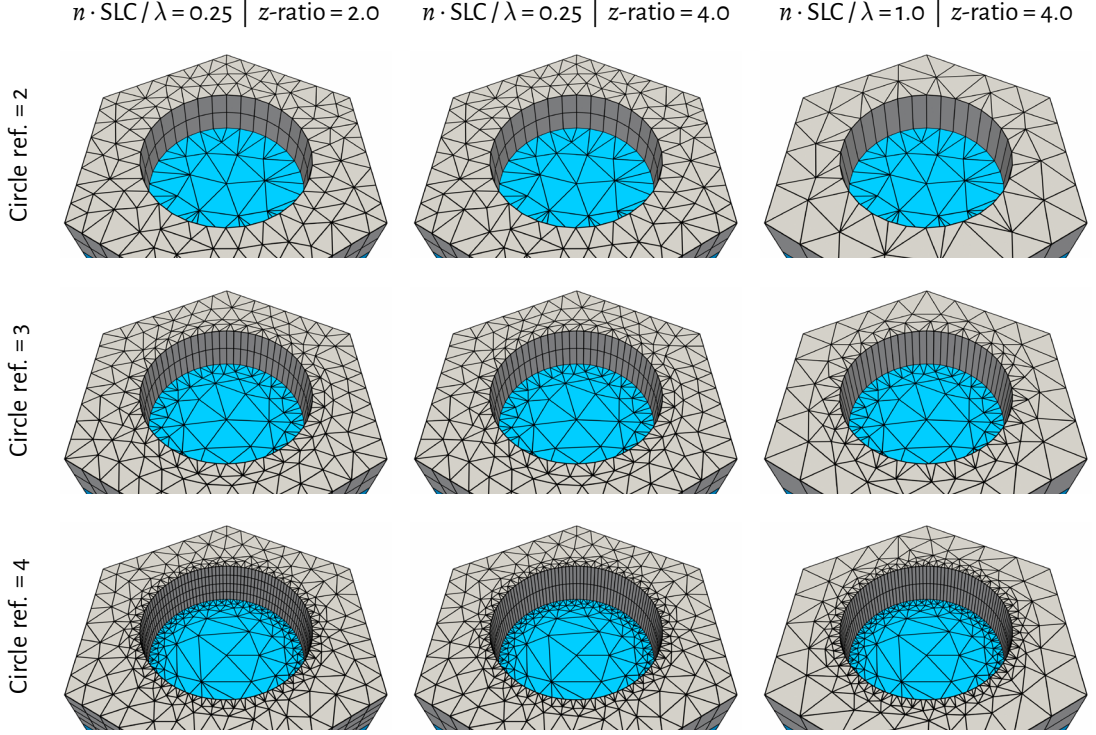


Figure 22: 3D Example meshes for the nanohole array simulation as a function of SLC/ λ -ratio, circle refinements RAC and maximum z-ratio. Each of the nine images shows the same detail of the 3D finite element mesh for the nanohole array, omitting the superspace for visibility and depicting the subspace in cyan and the PhC material in gray (compare figure 9). The refine all circle (RAC) parameter increases across the rows. Columns 1 and 2 have a fine in-plane mesh, controlled by the adaptive meshing parameter SLC/ λ -ratio, while column 3 has a coarser in-plane mesh. At the same time, column 1 has a stringent limit for the maximum z-ratio (equation (4.15)), while columns 2 and 3 have a looser one.

the side length constraint in z -direction for each extrusion layer is chosen as

$$\text{SLC}_z = \max \left\{ \frac{\lambda \cdot (\text{SLC}/\lambda\text{-ratio})}{n_{\max}} \quad \middle| \quad l_{\text{ip}} \cdot (\text{z-ratio}) \right\} \quad (4.15)$$

$$\text{with } l_{\text{ip}} = 2r \sin \left(\frac{\pi}{4 \cdot 2^{\text{RAC}}} \right),$$

which adds extra adaptivity to the mesh. Figure 22 depicts a number of 3D-views of the mesh (air domain not shown) for different combinations of the mesh-relevant parameters. The RAC-setting is increased across the rows. The first column combines a fine overall meshing with a very stringent value for the z-ratio of 2. However, the z-ratio setting only causes additional z -layers for the case of RAC = 4. In columns 2 and 3 this limitation is softened to 4, causing no extra layers in column 2, which means that the z -meshing is dominated by the SLC/ λ -ratio setting. For column 3, the rough overall meshing again causes that additional layers are introduced for RAC = 4. It must

hence be stressed that this approach causes a “responsiveness” of the mesh, which is advantageous on the one hand, but must be kept in mind when looking at the effects of these parameters in the convergence study on the other.

4.4.2 Convergence analysis

The convergence study is performed in the same way as for the previous example systems. Compared to the Mie system there is another meshing parameter: the maximum z -ratio. The main differences are (i) the use case and (ii) the absence of an analytical reference solution.

Addressing difference (i), the typical use case is an analysis of an output quantity, e.g. reflectance or field enhancement, as a function of the illumination conditions, i.e. the direction of incidence defined by θ and ϕ and the vacuum wavelength λ_0 . Consequently, the parameter space is huge and choosing a suitable test condition is a difficult task. In the following, the test condition is denoted as a “sample point”, i.e. a specific set of the illumination condition parameters. At first, λ_0 should be chosen at the lower end of the interval of interest, although this may not be crucial since the meshing adjusts to the wavelength via the SLC/λ -ratio. It may also be advantageous to use a sample point which is far from any photonic modes, i.e. a “flat” part of the solution space. If the position of modes is not known beforehand, e.g. from a band structure analysis, it is hence unavoidable to perform an *a priori* scan to find such a region.

For difference (ii), a quasi-analytical solution must be generated by solving the system with wisely chosen input parameters potentially at the edge of the computational possibilities. This means that

- adaptive techniques such as initial p -adaption should be used to approximately reach a target accuracy, allowing the maximum implemented FE degree $p = 10$,
- the defined target accuracy must be considerably lower than the desired final accuracy of the optimized setup (e.g. 3 orders of magnitude),
- when setting input parameters, those which are known to limit the maximum accuracy must preferably be adjusted,
- everything must be increased until the limits for the memory (random-access memory (RAM)) and (reasonable) computation time are exploited.

It must be stressed that this is the most crucial step, since the convergence of this simulation can not be guaranteed without a further increase of the computational costs.

For the actual study, a flat part of the solution space was localized resulting in a suitable illumination condition of

$$\text{TE-polarization, } \phi = 90^\circ (\Gamma - K), \quad \theta = 10^\circ, \quad \text{and} \quad \lambda_0 = 1050 \text{ nm.}$$

(See section 3.2.1 and figure 9 for related definitions.) It will be proven below that the optimization for this point also holds for points in non-flat regions, i.e. when facing

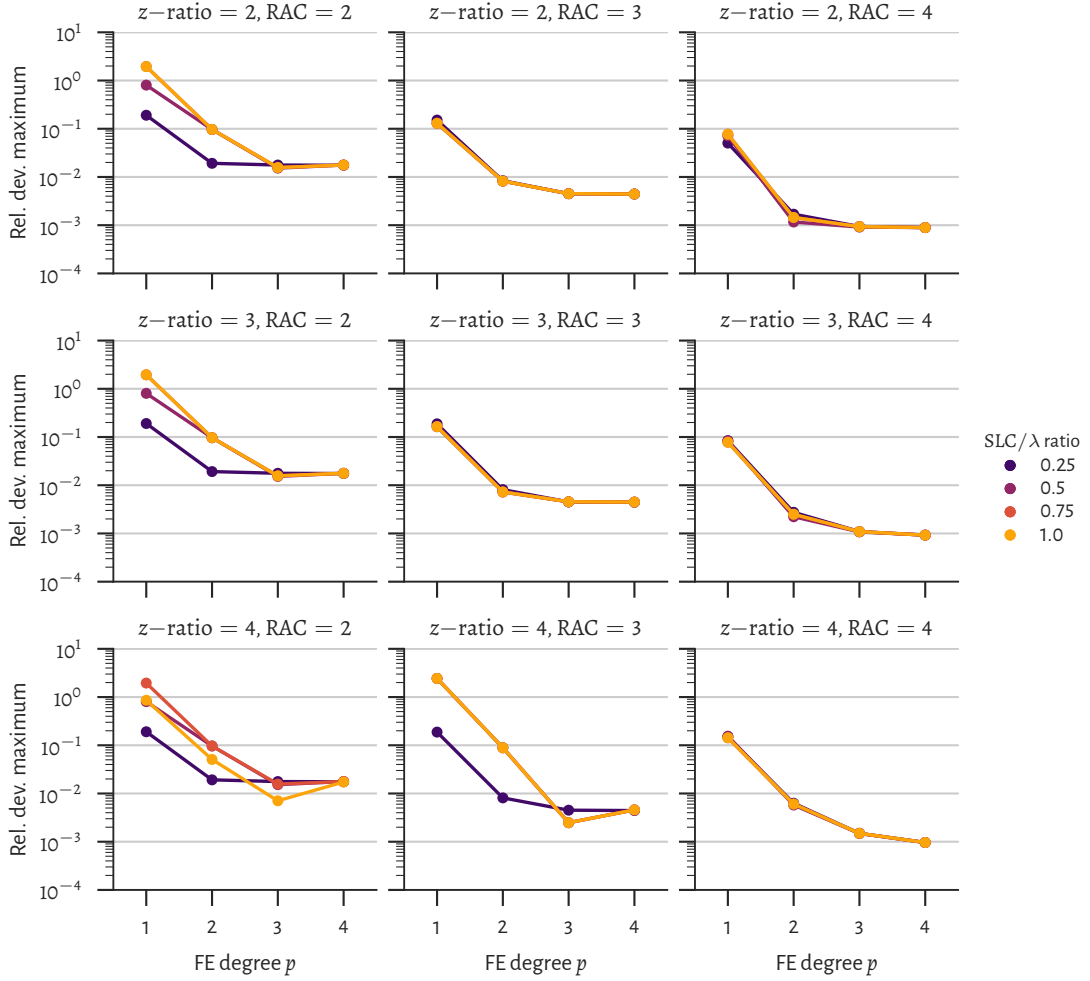


Figure 23: Convergence study results of the nanohole array simulation. The maximum relative deviation of all output quantities defined in table 3.1 for $\Gamma - K$, TE, $\theta = 10^\circ$ and $\lambda_0 = 1050$ nm from the quasi-analytical reference solution is shown for different maximum z -ratios (**rows**) and refine all circle (RAC) values (**columns**) as a function of the finite element polynomial degree p . Different colors represent different values of the adaptive meshing parameter SLC/λ -ratio, given by the legend at the right.

a sharp mode. For the reference solution, initial p -adaption was utilized with a specified target accuracy of 10^{-6} . Since it was already shown in the Mie example system (section 4.3) that the circle refinement parameter RAC is drastically limiting the maximum accuracy, this parameter is preferred and set to $RAC = 5$ (which is at the edge of possibilities on the utilized system.) All input parameters together with computational costs are summarized in the lower row of table 4.2 on page 84. The simulation needed more than 400 GB of RAM and included more than 5 million unknowns.

The results of the convergence study are summarized in the graphs of figure 23. Here, the y -axis shows the maximum relative deviation of all output quantities, as

listed in table 3.1, with respect to the quasi-analytical reference solution. The maximum z -ratio is varied across the rows, while the RAC-setting is varied across the columns and the SLC/λ -ratio is color-coded.

Surprisingly, the SLC/λ -ratio has only a small influence on the convergence, which might be due to the meshing in z -direction, which is adjusted with the circle refinement to avoid high aspect ratio elements. For larger values of RAC the meshing in z -direction gets extremely fine, therefore having a much higher influence on the number of elements than the SLC/λ -ratio. This is confirmed when observing that the z -meshing has a gradient from the bottom-left to the top-right in the figure, consequently showing the highest spread with the SLC/λ -ratio in the bottom-left plot.

As for the Mie system, the number of circle refinements seems to limit the maximum accuracy, which is best seen for $p = 3, 4$, where the relative deviation seems to saturate. Especially in the top row, where the z -meshing is fine and has a small effect, where increasing RAC shifts the saturation deviation to smaller values.

4.4.3 Performance optimization

Just as shown in section 4.3 it is now an easy task to find an optimum configuration for which all output quantities fall below a target accuracy. A target accuracy of 2 % is chosen, which appears adequate when comparing to any of the experimental results presented in later chapters. Again, the number of unknowns will serve as the performance measure.

Table 4.2 lists the six optimum configurations obtained in the parameter scan together with memory usage, number of unknowns and the reached maximum relative deviation. The lower row lists the parameters and results for the reference simulation for comparison. Comparing the values for memory usage and unknowns between the rows reveals that only *three* different simulations have actually been performed, because it is unlikely that different simulations lead to the exact same values for these quantities. These unique simulations are labeled with letters *A*, *B* and *C* in the first column. This behavior is expected, since the adaptive mesh parameters (SLC/λ -ratio and z -ratio) do not enforce unique meshes for any value (compare figure 22). The optimum configuration uses a higher FE degree compared to the five other configurations, which again underlines that this is beneficial once a well-adapted mesh is reached (see section 3.1.4).

4.4.4 Verifying the convergence on a narrow peak

The convergence study was executed in a flat region of the solution space, i.e. off-resonance, since the absolute values of output quantity can vary considerably if the resonance frequency shifts. In the following, an extended analysis is shown to proof that the determined configuration nevertheless gives accurate results on-resonance.

Input parameters					Output quantities		
	p	SLC/ λ	RAC	z-ratio	Mem. (GB)	# Unkn.	Rel. dev. max.
A	3	1.00	2	4.0	2.47	61839	7.05e-03
B	2	0.25	2	2.0	2.09	67498	1.92e-02
	2	0.25	2	4.0	2.48	67498	1.92e-02
	2	0.25	2	3.0	2.48	67498	1.92e-02
C	2	1.00	3	3.0	2.42	84796	7.26e-03
	2	0.75	3	3.0	2.42	84796	7.26e-03
Reference simulation (adaptive p -setting)							
	≤ 10	0.40	5	3.0	404.90	5063320	$\leq 1e-06$

Table 4.2: The six optimum configurations of the nanohole performance optimization with target accuracy of 0.02. The configurations, defined by their input parameters finite element polynomial degree p , adaptive meshing parameter SLC/ λ -ratio and refine all circle (RAC) and maximum z-ratio are listed together with their computational costs (memory usage and number of unknowns) and precision (represented by the maximum relative deviation of all output quantities defined in table 3.1 at $\lambda_0 = 1050$ nm). The rows are sorted in ascending order with respect to the number of unknowns, which acts as the performance measure. Comparing the values for the computational costs between the rows reveals that only *three* different simulations have actually been performed, which are labeled by *A*, *B* and *C* in the first column. The last row shows the values for the reference simulation, which used adaptive p -setting to reach a precision $\leq 10^{-6}$.

The left plot of figure 24 shows the results of an angle scan for the fixed wavelength of 1050 nm and both polarizations, TE in red, TM in blue. Both polarizations exhibit a peak in this angle range, the TM-peak being the sharper one of the two. As a quantification of the peak position accuracy of this scan executed with the optimum configuration of table 4.2, 13 points near the peak maximum were computed using the reference configuration. For both cases, the data was fitted using a Lorentzian of the form $1/[(\lambda - \lambda_0)^2 + (\lambda_0/2Q)^2]$ plus a linear background. The results are shown in the right plot of figure 24, denoted as “high-res.” for the reference and “low-res.” for the performance-optimized configuration. From the fit data, the peak centers coincide with an accuracy of $1.05 \cdot 10^{-4}$, which is far below the target accuracy. The relative deviations for the less crucial amplitude and width are higher (≈ 0.1), possibly caused by the sparse reference data. However, when taking into account the peak width of $\approx 0.3^\circ$ this is a very satisfying convergence.

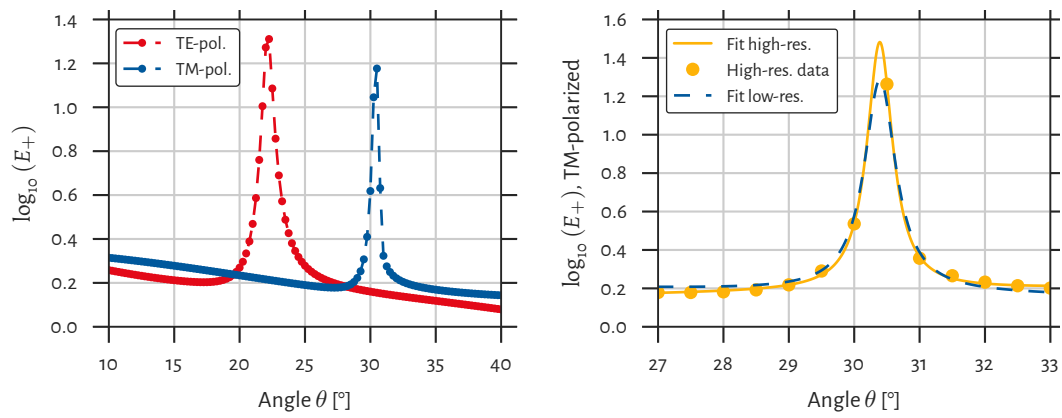


Figure 24: Angle scan results for the nanohole system near a peak. (Left) Logarithm of the electric field energy enhancement $\log_{10}(E_+)$ as a function of the incident angle θ . The simulations used the input parameters obtained from the performance optimization listed in the top row of table 4.2, which is denoted here as low resolution (low-res.). (Right) Comparison of the data for the TM-peak of the left plot (blue) and a scan using a high-accuracy reference configuration (yellow, denoted as high-res.). The curves are obtained from Lorentzian peak fits, while the yellow dots denote the actual data points of the high resolution scan.

5

Discovering Symmetry Dependence in Anticrossing Phenomena

A SLAB-TYPE PHOTONIC CRYSTAL (PhC) is often referred to as a “quasi 2D PhC” to underline its translational symmetry in two dimensions and, at the same time, to emphasize the difference to 3D PhCs. The third dimension, however, plays an important role for PhC slabs as well when regarding the symmetry properties in this direction. In the following, the latter statement will be investigated using the example of a crossing point of two bands in the nanohole array, as published in [41].

Suppose that two bands of the nanohole array on glass show so-called anticrossing, i.e. their coupling results in a frequency splitting that “avoids” the crossing of these bands. The glass substrate causes the system to lack mirror symmetry with respect to a plane perpendicular to the z -axis, as it is the case in a PhC slab completely surrounded by air, for instance. If the system could be symmetrized in z -direction modes may become orthogonal, so that a coupling between them would be forbidden by symmetry; – finally causing the anticrossing effect to disappear.

Such an investigation is possible both experimentally, by sandwiching the PhC slab between glass plates and using an index-matching fluid (IMF) to fill the holes, and numerically, by symmetrizing the system using proper geometry and material parameters. After repeating some background information that was presented in previous chapters, a study on the symmetry-dependent anticrossing phenomenon will be presented in detail. The experimental reflectance from angular-resolved reflectance (ARR) measurements (section 3.4.1) is compared to numerical reflectance and field enhancement calculations, showing the disappearance of anticrossing when symmetrizing the system. Later, in section 7.2, these results will be revisited and further investigated using the machine learning approach.

5.1 Background and guide to relevant sections

In the theoretical treatment of PhC slabs in section 2.2, especially in sections 2.2.5 and 2.2.6, the effects of symmetry characteristics on the photonic modes have been presented in detail. It was shown that the nanohole array has C_{6v} symmetry, as the perhaps conically shaped holes and the glass substrate break the mirror symmetry with respect to the xy -plane. If the conical shape of the holes could be neglected and the superstrate material would have the same permittivity as the substrate, this mirror symmetry would be restored, resulting in the higher symmetry $D_{6h} = C_{6v} \times C_{1h}$. In the same section, it was shown that these symmetry properties can have an effect on the *coupling* of modes, because the orthogonality of the related eigenvectors may depend on it.

The geometry of the nanohole array system was described in section 3.2, as well as details on the numerical treatment using the finite element method (FEM). Moreover, in section 3.2.4 the quantities considered here, such as the reflectance R and the electric field energy enhancement E_+ have been introduced, together with a description of how to obtain them numerically. An overview can be found in table 3.1 on page 52. Details on the involved materials have been given in section 3.3, and the sample fabrication was outlined in section 3.5.

5.2 Sample design and numerical model

To perform the experiment outlined above, a nanohole array sample with a lattice constant of 1000 nm and a hole diameter at z center of 425 nm was used (which was already mentioned in a previous study [27]). Two different versions of this system are necessary, which are

1. the **z -asymmetric case**: with a glass substrate and an air superstrate; and
2. the **z -symmetric case**: for which the superstrate is (basically) composed of glass as well.

Figure 25 gives an overview of these systems for the real and the numerical case. The two left-hand sketches in the upper row illustrate the geometry of the real system. At first, the asymmetric case will be considered. As explained in more detail in section 3.5, the sample is fabricated using nanoimprint lithography (NIL), so that an additional sol-gel layer exists between the silicon PhC slab (thickness: 310 nm) and the glass substrate. The sol-gel, which by approximation has the same optical properties as the glass, features additional pillars, which are also partly missing. The overview SEM image in the lower row of figure 25 reveals a number of such cases. From the zoomed SEM image at the right, one may further notice the gradient at the hole outlines, which can be attributed to a conical shape of the holes. In the related sketches of the upper row (left), this shape is considered by the side-wall angle α of roughly 15° .

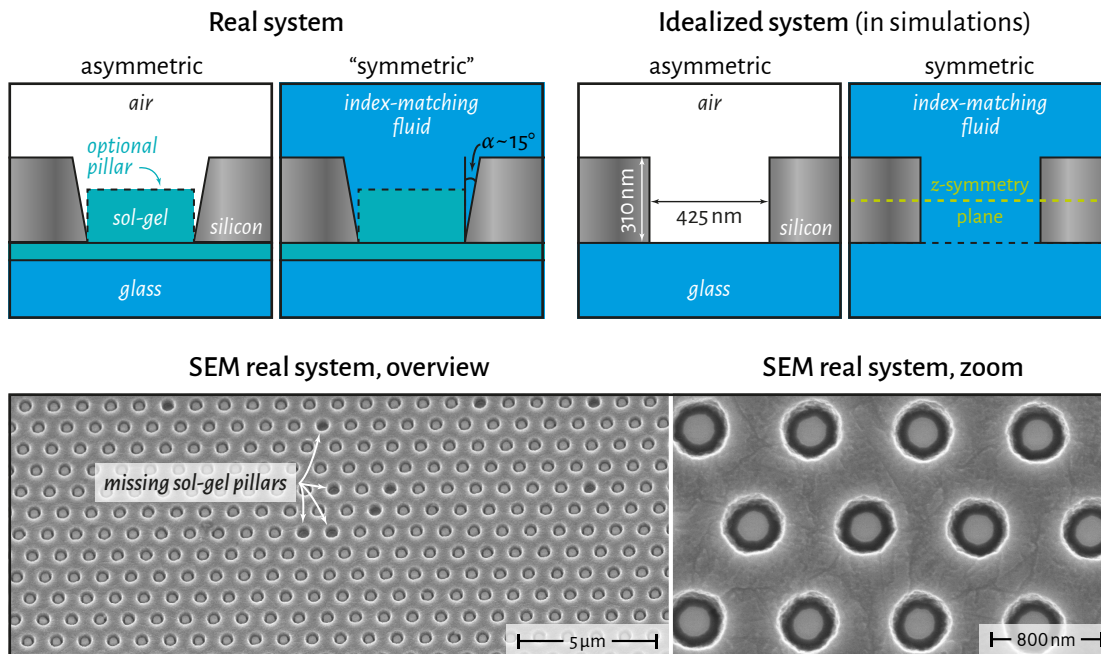


Figure 25: Overview of the sample geometry used for the anticrossing experiment and the considered numerical model. (Upper row) Geometry sketches of the asymmetric and symmetric case for the real system (left) and the idealized numerical model (right). The former exhibits a sol-gel layer with partly missing pillars between the PhC slab and the glass substrate. The holes have a conical shape, indicated by the side-wall angle α . The symmetric cases uses an index-matching fluid that fills up the holes. For the numerical model the conical shape is neglected, as well as the sol-gel layer and its pillars, achieving a z-symmetric system indicated by the green dashed line. **(Lower row)** Scanning electron microscopy (SEM) images (provided by Carola Klimm of HZB) of the system for the asymmetric case. The left image shows a large area under a tilt angle of 30° , featuring holes with missing pillars. The right-hand zoom gives a clearer view of the gradient color at the hole circumferences.

To obtain the symmetric case for the real system, an IMF (matching the refractive index of the glass) is used to fill up the holes and to achieve an accurate interface to a second glass plate attached from above. Regarding the optical properties the PhC slab is effectively surrounded by glass. The z-mirror symmetry is therefore approximately restored and only broken by the conical shape of the holes.

The two right-hand sketches in the upper row of figure 25 illustrate the geometry used in the FEM simulations. In both cases, the conical shape of the holes is neglected in order to obtain a perfectly z-mirror symmetric system for the symmetric case. The sol-gel – especially the pillars – are neglected as well, so that the glass substrate is located directly below the PhC. For the symmetric case, the complete superspace is modeled as glass, so that the incident radiation comes from a glass half-space. It will be shown below that the applied simplifications can be justified using a comparison of experimental and numerical reflectance maps.

5.3 Reflectance and field energy enhancement analysis

The reflectance of both systems was first studied experimentally by ARR measurements (see section 3.4.1) using a wavelength resolution of 2 nm and an angle resolution of 2°. The results are shown in the first column of figure 26 (see also the blue area in figure 10 for the silicon material properties). For the symmetric case the actual angles of incidence θ_{actual} on the PhC were calculated from the angles in the ARR measurements $\theta_{\text{meas.}}$ via

$$\theta_{\text{actual}} = \arcsin \left(\frac{\sin \theta_{\text{meas.}}}{n_{\text{glass}}} \right), \quad (5.1)$$

since the beam undergoes an additional refraction at the air-glass interface. In the following, all results are for the case of the Γ - K direction and transverse-magnetic (TM) polarization. The reflectance maps reveal a large set of bands corresponding to leaky modes. When comparing the two maps for the asymmetric case and the symmetric case, one observes only a slight transformation: the bands are “squeezed” in the direction of smaller angles when the glass superstrate is introduced, so that the same features occur at shallower angles. But more interestingly, bands that show anticrossing features in the asymmetric case, i.e. which “avoid” crossing and show a visible gap of low reflectance, are modified in the symmetric case. Here, these bands get much closer to each other or even cross – as far as it can be estimated from the limited data resolution.

The reflectance maps obtained from FEM simulations are shown in the second column of figure 26. To assess the match between the numerical model and the actual measurements a coarse scan with a wavelength resolution of 2 nm and an angle resolution of 1° was considered. An excellent match with the experimental data can be observed, especially for the long wavelength range. The absolute value of the reflectance is overestimated by the simulations, as it is expected due to the assumed perfect symmetry of the system.

Afterwards, a finely sampled scan was performed in the regions of the (anti)crossing phenomena with a wavelength resolution of 0.25 nm and an angle resolution of 0.25°/0.1° for the asymmetric/symmetric case, respectively (column three in figure 26). In the symmetric case the reflectance bands get much closer to each other, but they do not actually cross. The line shape of the reflectance spectrum is supposed to be caused by interference between various scattering contributions (Fano resonances [105]). The actual crossing of the bands can finally be seen when looking at the E -field energy enhancement maps (E_+) in the fourth column. E_+ is the integrated electric field energy density distribution over the superspace volume V , normalized to the energy of the incident plane wave source in the same volume; where V is defined by the PhC hole and a 250 nm layer above the silicon (see section 3.2.4 and table 3.1 for further details). For the symmetric case the bands cross straightly, which means there is no interaction between them. Since the only characteristic that changed is the symmetry, this

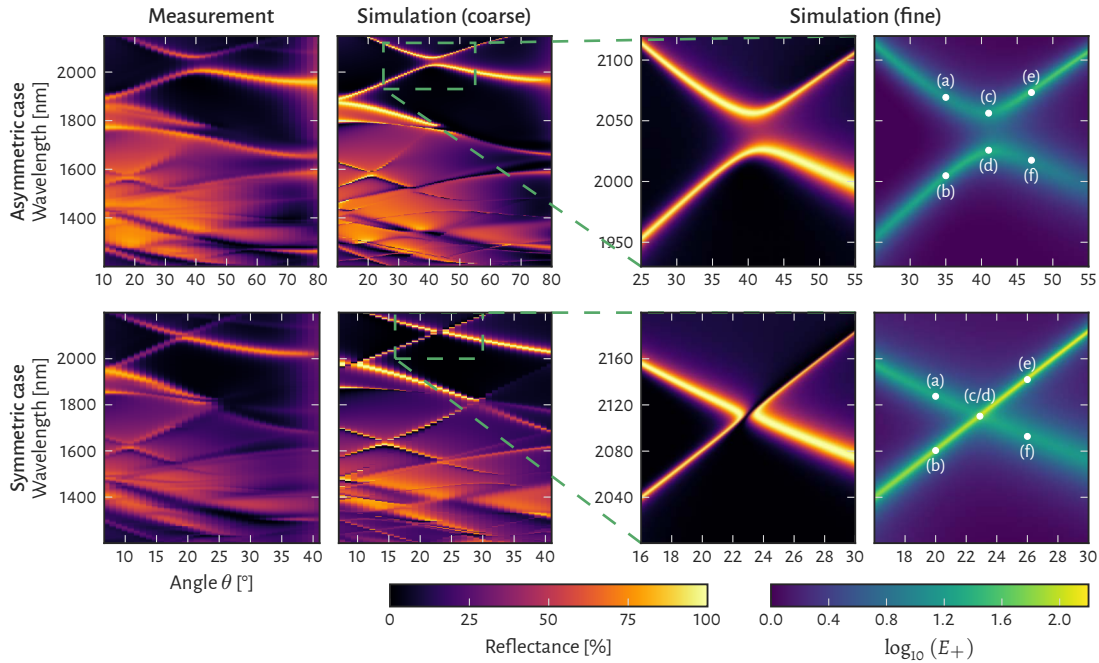


Figure 26: Overview of experimental and numerical reflectance maps, and numerical field energy enhancement maps for the silicon PhC slab on glass. Results are shown for the systems with air-superstrate, i.e. the asymmetric case (**upper row**), and glass-superstrate, i.e. the symmetric case (**lower row**). (**Column 1**) Reflectance maps from ARR measurements as a function of the vacuum wavelength (y -axis) and incident angle θ (x -axis). The quantities of the axes apply for all columns (see figure 9 on page 49 which indicates θ) and the left color bar applies for columns 1, 2 and 3. (**Column 2**) Numerical results for the reflectance in the same wavelength- and angle-range as for the ARR measurements. (**Column 3**) Zoom of the investigated crossing/anticrossing regions with reflectance results from finely sampled simulations. (**Column 4**) E -field energy enhancement (E_+ , right color bar) for the same region as in column 3. Additional markers in each plot show the positions for which field distributions are shown in figure 27. (See section 3.2.4 and table 3.1 for details on the shown quantities.)

necessarily means that the coupling is prohibited by symmetry laws, as explained in the introductory statements above. In contrast, for the asymmetric case the bands bend and form a broad interaction region, which certainly indicates the coupling of the bands.

5.4 Analysis of field distributions

Although the crossing/anticrossing is shown using the field enhancement plots, the coupling of the modes can more directly be studied when looking at the field distributions. To this end, points along each band near the (anti)crossing point have been chosen by searching for the maximum field enhancement on each band for specific angles, as marked in figure 26 (white dots in column 4). Figure 27 shows the absolute

values of the magnetic field strength in the xy -(mirror)-plane for each component at these points for the asymmetric and the symmetric cases. In both cases we observe that aside from the (anti)crossing point the two bands exhibit orthogonal polarization: the band following the path (a) – (c) – (f) is transverse-electric (TE)-, while the band following the path (b) – (d) – (e) is TM-polarized. In the asymmetric case the polarization is less well pronounced as there is still a noticeable field strength in the components which are not attributed to their respective polarization (barely visible). In both cases the field patterns are exchanged when comparing points (a) and (b) to (e) and (f). However, In the symmetric case the patterns at points (c) and (d) (which are identical and in-fact a single computation) show a simple superposition of both solutions, while in the asymmetric case the fields are distorted.

5.5 Discussion

The previously presented results reveal the coupling of bands in the asymmetric case and the absence of coupling in the symmetric case from two different points of view: (i) from an observation of the anticrossing/crossing in field energy enhancement maps (figure 26, column 4), and (ii) from a distortion in the magnetic field components at the (anti)crossing point (figure 27). Both effects are expected from the line of reasoning presented at the begin of this section: namely the difference in the orthogonality of the modes between the symmetric and asymmetric cases.

The transition from asymmetric to symmetric corresponds to a change in the symmetry point group from C_{6v} to D_{6h} . The D_{6h} symmetry exhibits an additional mirror symmetry with respect to the xy -plane at the center of the PhC slab, which is associated with the separation of the TE and TM polarizations (compare section 2.2.6). However, the mirror symmetry is not broken “hardly”, i.e. the glass substrate and the conical shape can be regarded as only a perturbation. In consequence, it is not expected that the TE and TM polarizations are completely absent, but only disturbed. This is directly observed in the field patterns for the asymmetric case of figure 27.

In the case of perfect TE and TM polarization, the modes are orthogonal eigenvectors (compare section 2.2.1) and therefore do not couple. Once the bands approach each other, they can therefore cross without any interaction – just as seen from the field enhancement maps in figure 26. From this point of view, any deviation from the perfect polarization deteriorates the orthogonality, and thus increases the coupling. The result is the observed frequency splitting in the asymmetric case of the same figure.

The results are hence consistent, constituting two different aspects of the same phenomenon. They further showcase how accurately the symmetry laws presented in section 2.2 are fulfilled in the FEM simulations. Because of that, it also represents a case which is well suited to apply another analysis technique: the machine learning based

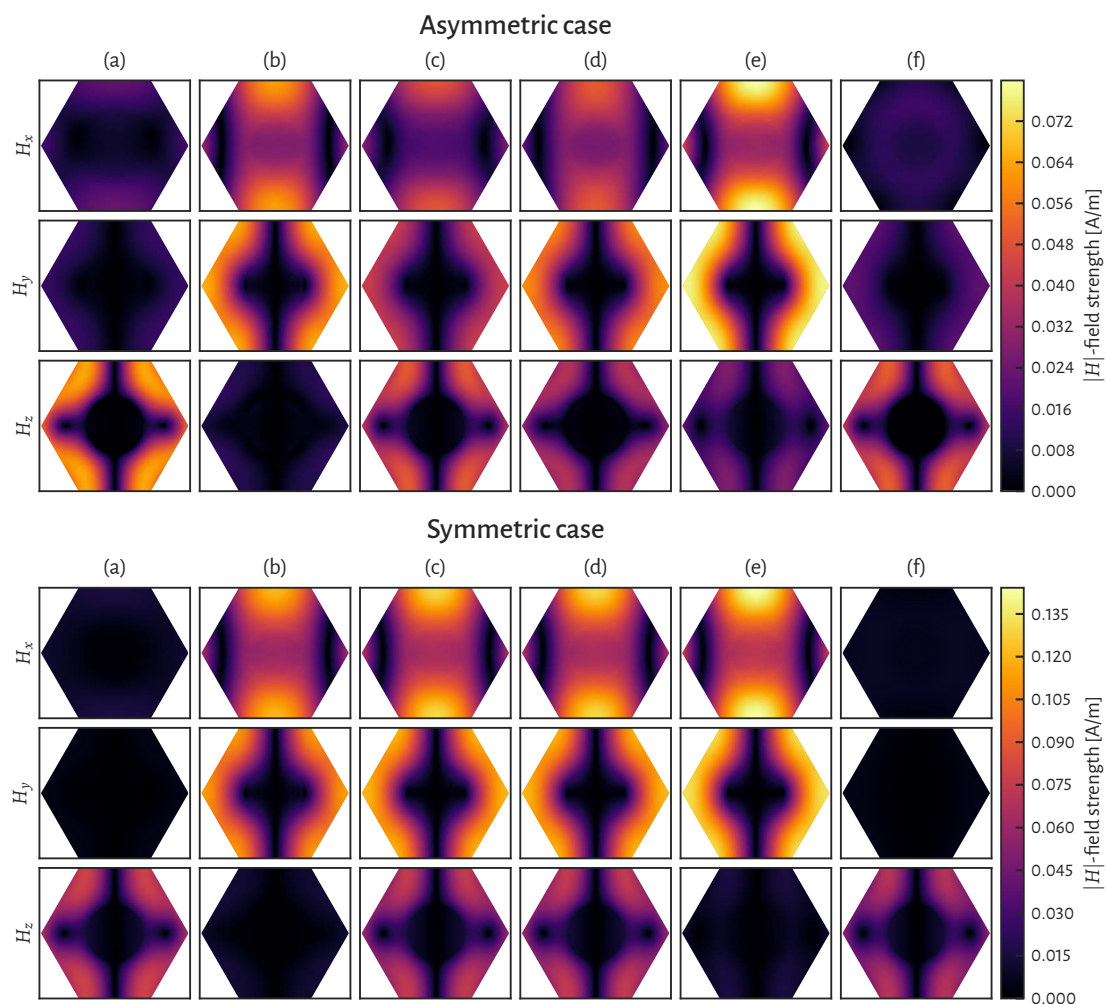


Figure 27: Selected magnetic field strength distributions in the xy -plane. (Upper row) Magnetic field (H) distributions for the asymmetric case in the xy -plane (x dimension on the x -axis, y dimension on the y -axis). Rows correspond to the absolute values of the x , y and z -component of the magnetic field, respectively. The field strength is color-mapped (color bar at the right). Columns correspond to the result on either point marked by white dots in column 4 of figure 26. **(Lower row)** The same depiction as in the upper row, but for the symmetric case.

classification of modes, as it will be shown in section 7.2. In general, anticrossing is of practical relevance as well, because in PhC waveguides the bending of modes at the anticrossing point leads to small group velocities. This phenomenon, commonly known as slow light, is of interest for many applications such as buffering, time-domain processing or the spatial compression of optical energy [106]. The analysis techniques presented here can potentially be applied to PhC waveguides as well, and therefore improve the design process of related systems.

6

Increased Fluorescence of PbS Quantum Dots by Excitation Enhancement

AFTER HAVING DEALT WITH AN EXPERIMENT that demonstrated fundamental characteristics of photonic crystal (PhC) modes in the previous section, the focus here is an effect which is highly relevant for applications: fluorescence enhancement of lead sulfide (PbS) quantum dots (QDs) on the PhC surface. This study was published in [42]. As it was discussed in detail in section 2.2.6, PhC slabs exhibit leaky modes that can be excited by external radiation and which can possess high local energy densities. In section 2.2.7 it was stated that these modes can be used to affect the emission properties of near-surface emitters by two different mechanisms: extraction enhancement and excitation enhancement. Both can lead to an increase in the radiation intensity yielded by exciting the emitters using light incident from the exterior, supposing that the spatial arrangement of the emitters overlaps with the field distributions of the leaky modes.

To reconsider these mechanisms in brief, extraction enhancement occurs if the leaky modes provide “channels” for the outcoupling of the emission. In other words, they scatter the emitted radiation out of the PhC plane. Therefore, this effect depends on leaky mode bands which cross the wavelength range of the *emission* of the QDs. In contrast, if leaky modes are present in the *absorption* wavelength range, excitation enhancement occurs if the emitters are in a volume of increased electromagnetic fields. Consequently, for excitation enhancement the leaky modes have to be excited by the light source, rather than by the emission itself, and therefore depend on the polarization and k -vector of the incident radiation.

Since the leaky mode properties of PhC slabs can be tailored to a large extent, possible applications of these emission enhancement mechanisms can be found in many

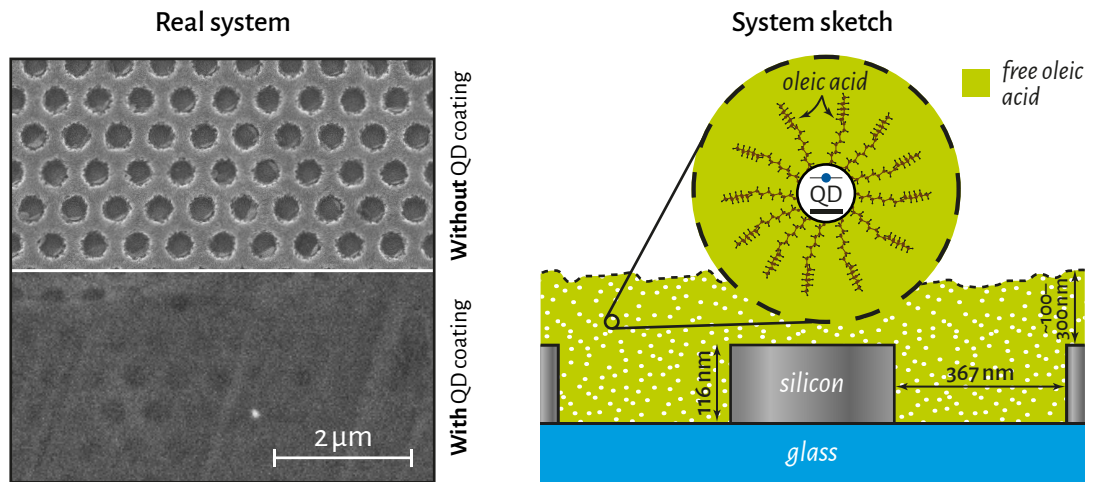


Figure 28: Overview of the sample used for the fluorescence enhancement experiment. (Left) Scanning electron microscope images (provided by Carola Klimm of HZB) of the silicon photonic crystal slab without (top) and with (bottom) quantum dot (QD) coating. (Right) Sketch of the supposed system geometry. A coating of lead sulfide quantum dots (white dots) surrounded by free oleic acid (OA, greenish) fills up the holes and extends ≈ 100 nm to 300 nm above the slab. The zoom illustrates a single QD embedded into an OA matrix.

fields, most prominently in light-emitting diodes (LEDs) [14, 15] and biosensors [16]. An overview of the relevant literature was already given in the introduction (chapter 1). The objective of the experiment presented here is to increase the fluorescence of PbS QDs located on the PhC surface. This is done by experimentally mapping the integrated omnidirectional fluorescence of the QDs interacting with leaky modes of the PhC by using an angle- and excitation wavelength-resolved setup. Directional characteristics of light extraction are eliminated by placement of the sample inside an integrating sphere, hence allowing a pure determination of excitation enhancement effects. The spectral positions of the modes, as well as respective enhancement factors of the electric field energy density are calculated in finite element method (FEM) simulations. The experimental fluorescence enhancement features are explained by considering the field energy enhancement together with an analysis of its three-dimensional spatial distribution. Later, in section 7.4, these results will be reconsidered and analyzed using a machine learning-based approach.

6.1 Sample geometry and quantum dot coating

The platform used for the generation of increased electromagnetic near-fields is a nanohole array sample on glass with a lattice constant of $a = 600$ nm, a slab thickness of $h = 116$ nm and a hole diameter of $d = 367$ nm (see section 3.2 for further information on the system geometry and details on the numerical treatment; see section 3.5 for

details on the fabrication process). These accurate geometrical parameters have been obtained from a comparison of experimental and numerical reflectance properties, as it is explained in the next section. A scanning electron microscopy (SEM) image of this sample is shown in figure 28 (left, top). The conical shape of the holes is neglected because of the small thickness of the silicon layer, i.e. a side-wall angle of $\alpha = 0^\circ$ is assumed.

Except for the reflectance study considered in the next section, the PhCs are covered with spherical PbS QDs with a diameter of (5.6 ± 0.8) nm (see section 3.3.3) using the convective assembly technique – a high-accuracy process that distributes the QDs evenly across the sample [93]. The coating is visible in the SEM image in figure 28 (left, bottom). Prior to the deposition on the PhC surface the QDs are solved in toluene, which is removed in the covering process. The surface of the QDs is shielded by an oleic acid (OA) ligand.

Figure 28 (right) shows a sketch of the complete system in cross section after the particle assembly process. The coating is effectively a mixture of PbS QDs and free OA emerging from the assembly process. Based on SEM images, the thickness of the QD-OA layer is estimated to be in the range of 100 nm to 300 nm. However, the surface roughness and the exact distribution of the QD-OA coating is not known, which is the main source of uncertainty in the experiment.

6.2 Reflectance properties of the uncoated sample

The foundation for an accurate numerical modeling of the QD coated PhC system is the determination of the geometrical parameters of the PhC itself. As shown in section 3.2, these are mainly the slab thickness h , the hole diameter d and the side-wall angle α . To achieve appropriate values, the model has been optimized by comparing measured and simulated reflectance maps (see section 3.4.1 for details on the measurement technique and section 3.2.4 for related theoretical and numerical details). Figure 29 (upper row) shows the measured reflectance for the four combinations of sample orientation (corresponding to $\Gamma - M$ and $\Gamma - K$) and source polarization (transverse-electric (TE) and transverse-magnetic (TM)). Just as for the reflectance investigation of the anti-crossing experiment in section 5.3, reflectance values of almost 0 % to more than 90 % are observed. The parts with high reflectance values can be attributed to leaky modes.

The numerically obtained reflectance maps are shown in the lower row of figure 29. A comparison with the measured reflectance was used to reconstruct the exact geometrical parameters of the produced sample. As this step necessitates to solve the system for a very large number of parameters, the so-called reduced basis method* was used [47, 107]. This method, which is not covered here in detail, enables to compute solutions for the parameter configurations much faster by using a model order reduction

*The reduced basis method analysis was performed by Dr. Martin Hammerschmidt of ZIB.

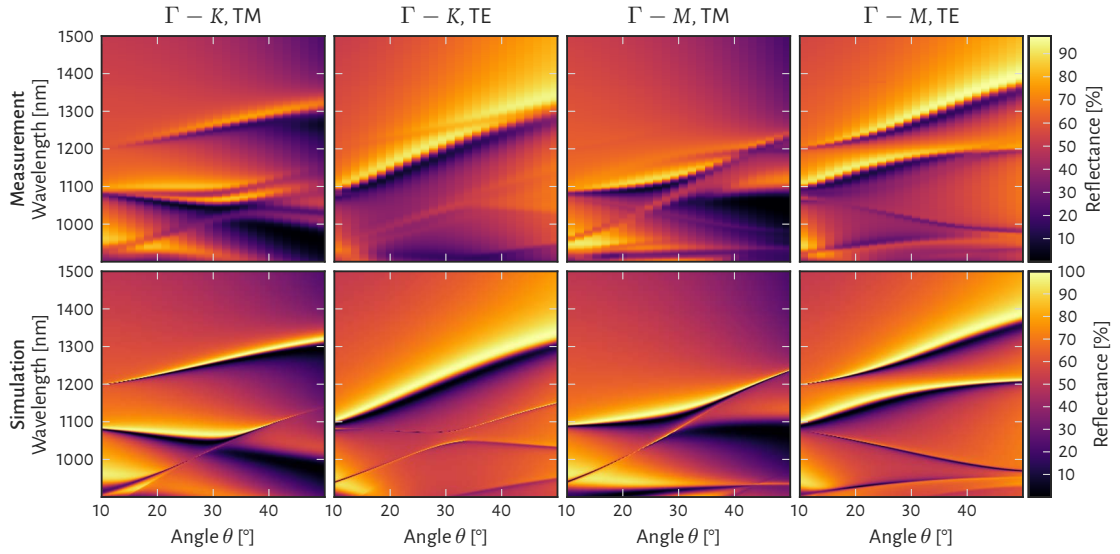


Figure 29: Comparison of experimental and numerical reflectance of the photonic crystal without quantum dot coating. (Upper row) The reflectance obtained from angular-resolved reflectance measurements is shown as a function of the vacuum wavelength and incident angle θ of the incident light (see figure 9 on page 49 which indicates θ). The columns correspond to the four combinations of sample orientation ($\Gamma - M$ and $\Gamma - K$) and source polarization (transverse-electric (TE) and transverse-magnetic (TM)). **(Lower row)** Simulation results for the reflectance in the same wavelength- and angle-range after geometry reconstruction.

technique. In simple terms, the full FEM problem is only solved for a small number of “snapshots”, yielding a reduced basis replacing the finite element space (denoted as V_h in section 3.1.2). The resulting simplified problem can be solved in milliseconds, so that detailed scans over the geometrical parameters can be executed efficiently. From these scans an optimum solution is selected by comparing to the experimental results. More precisely, a first guess based on SEM images yielded a silicon thickness of ≈ 130 nm and a hole diameter of ≈ 360 nm. The numerical reconstruction generated more exact values which were given above, and moreover confirmed the assumption that the conical shape of the holes is negligible.

The resulting maps of figure 29 (lower row) agree excellently with the measured results (upper row) in the whole spectral range. An interesting feature is that the measured maps always possess weak effects from the bands of the opposite polarization: TE bands are weakly seen in TM maps for the same direction, and vice versa. This is most probably caused by symmetry deviations (e.g. by fabrication tolerances), which cause the modes to be not ideally orthogonal and hence weakly excited by the opposite polarization; – an effect very similar to the one in the anticrossing experiment of chapter 5. The numerical maps, however, do not possess these effects because of the idealized geometry, and thus reveal the “true” modes for each polarization. It can be reasoned from this comparison that the numerical model gives accurate predictions

for the fabricated sample.

6.3 Measured fluorescence enhancement

With the numerical optimization of the previous section an accurate geometrical model of the PhC slab was gained. In the following, the actual fluorescence enhancement measurements are considered. This involves the treatment of *coated* PhC, as described in section 6.1. A detailed discussion of the features of the experimental setup was covered in section 3.4.2, so that only the main aspects are repeated here.

The design of the experiment for the fluorescence measurement is related to the absorption and emission properties of the QDs, which were covered in section 3.3.3 (see figure 11 on page 57). For the wavelength of the excitation laser source a range of 1080 nm to 1140 nm was chosen. The optical properties of silicon in this wavelength were discussed in section 3.3.2 (see yellow area in figure 10). In this range, the QDs show a considerable absorption and do not show a fluorescence themselves. Moreover, the absorption of the silicon is low, which would deteriorate near-field enhancement effects [27]. The PhC was designed in a way that it exhibits only a few well-isolated bands in the laser excitation wavelength range, as can be seen from the reflectance maps of figure 29. The reason for this choice is to facilitate the interpretation of the fluorescence measurements in the end.

A sketch of the experimental setup was shown in figure 13 on page 61. The QD fluorescence on the PhC surface was measured in an angle- and wavelength-resolved setup in a region of high layer thickness of the QD coating in order to reach a sufficient signal (≈ 300 nm). Due to the usage of an integrating sphere, the fluorescence measurement is independent of directional effects of the light emitted by the quantum dots.

The top row of the upper panel of figure 30 shows the fluorescence enhancement (F_+) maps obtained by tilting the sample along the respective high-symmetry directions ($\Gamma - M$ and $\Gamma - K$) and by using TE and TM polarization of the incident laser radiation. Each measured spectrum (for a single incident angle) was first integrated over the fluorescence peak from $\lambda = 1200$ nm to $\lambda = 1700$ nm and normalized to the measured incident laser power and the absorption profile of the QDs. The results have further been corrected for a dependence on the incident angle of the integrating sphere. This was done by using a planar reference, i.e. the PbS/OA system on an unpatterned silicon film of the same thickness as the PhC slab. These corrections and subsequent background filtering yield the integrated fluorescence F of the QDs for a single configuration of the incident radiation. A minimum estimate for the fluorescence enhancement F_+ is obtained by dividing by the minimal value in each of the maps.

One observes clear and sharp features of enhanced fluorescence with a maximum enhancement factor of $F_+ = 10^{0.18} \approx 1.5$, i.e. an increase of roughly 50%. An isolated steep band of enhanced fluorescence is observed for TM polarized light, with a higher

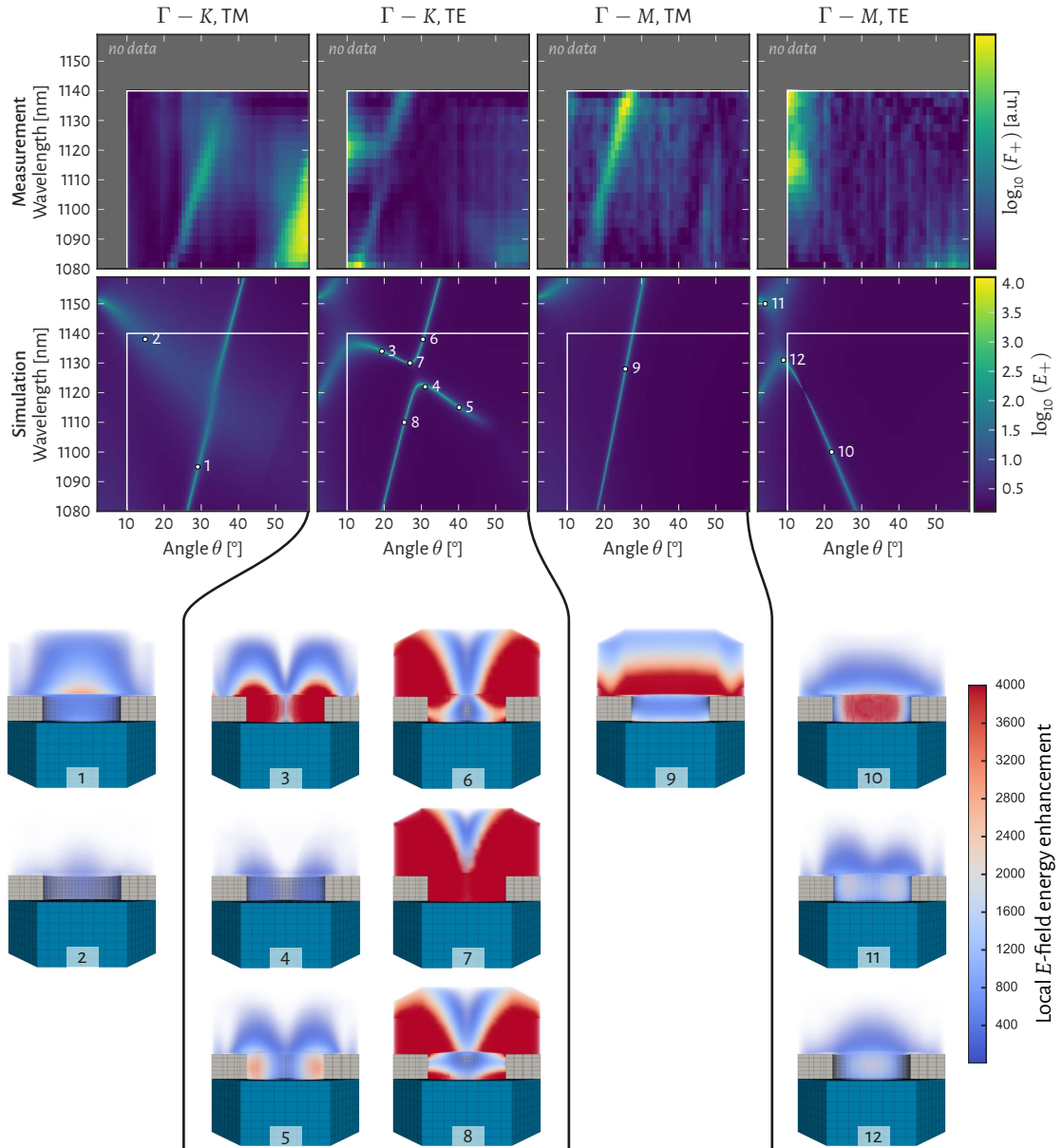


Figure 30: Comparison of measured quantum dot fluorescence enhancement F_+ and simulated field energy enhancement E_+ . (Top, upper row) Measured fluorescence enhancement F_+ as a function of the vacuum wavelength and incident angle θ of the laser source (logarithmic color scale; see figure 9 on page 49 which indicates θ ; see section 3.4.2 for experimental setup). Results are shown for the same combination of directions and polarizations as in figure 29. (Top, lower row) Simulated electric field energy enhancement E_+ for the same conditions as in the upper row. The white lines mark the experimental data limits. (Bottom) 3D volume renderings of the local field energy enhancement for the points marked in the E_+ maps. The different direction and polarization types are separated by black lines. All images are mapped with an identical color map (right), which is a trade-off between visibility of weak fields and minimal clipping of strong fields.

contrast in the case of $\Gamma - M$ direction. For TE polarization, distinct features can be observed as well, although with a more complex appearance.

6.4 Numerical model for the coated photonic crystal

As already mentioned, some geometrical parameters of the actual QD-coated PhC system are uncertain, namely the thickness of the QD-OA layer and its surface roughness. The main source of the problem is that the QD-mixture was assembled with a (non-linear) thickness gradient, because the necessary thickness for the experiment was initially unclear. However, the spot size of the excitation laser in the experiment was comparably large, so that the effects are integrated over many periods of the PhC lattice. To put it briefly, a number of different geometries for the numerical model have been tested, and the best match was found by *ignoring* the additional air-QD interface, i.e. by treating the QD-coating as a half-space. The geometrical model is therefore exactly the same as described in section 3.2 (figure 9), simply treating the superspace as the QD-OA-mixture.

In section 3.3.3 it was further shown that an effective refractive index of $n_{\text{PbS/OA}} = 1.64$ is a reasonable estimate for the coating, which is effectively a mixture of PbS ($n_{\text{PbS}} \approx 4.3$ [94]) and OA ($n_{\text{OA}} \approx 1.47$ [95]). This choice was confirmed by a parameter scan over the refractive index using the mentioned geometrical model, leading to $n_{\text{PbS/OA}} = 1.65$. For a comparison to experiments the incident angles are corrected for the additional refraction (as in equation (5.1)).

6.5 Comparison to numerical field energy enhancement maps

As it was noted above, the fluorescence enhancement is determined by integrating over the complete emission peak of the QDs, i.e. from $\lambda = 1200$ nm to $\lambda = 1700$ nm. When reconsidering the reflectance maps of figure 29, it is seen that there are no resonances beyond ≈ 1400 nm (it was checked that there are no resonances above the shown range until 1700 nm). From the reasoning presented in section 2.2.6, it can be followed that there is only a single leaky mode in the emission wavelength range of the QDs (per polarization and incident direction): – and only this mode could contribute to extraction enhancement (see section 2.2.7). Although it is not shown here, it was in fact ruled out that extraction enhancement effects play a quantitative role by analyzing selected fluorescence spectra.

Consequently, solely excitation enhancement can be responsible for the measured fluorescence enhancement. Recall from section 2.2.7 that excitation enhancement is caused by increased energy densities of the fields at the emitter positions. As a first step to explain the observed values it is hence reasonable to consult the electric field energy enhancement integrated over the simulated superspace volume, denoted as E_+

(see section 3.2.4 and table 3.1). The only difference is that the superspace volume is now composed of the PbS-OA-mixture, as explained above.

The numerically obtained field energy enhancement maps are shown in the lower row of the upper panel of figure 30 (using the same logarithmic color scale for all maps). It must be stressed that the upper and lower row do not show the same physical quantity. Later in the discussion it will be explained in more detail how both quantities may be compared. For now, it is observed that the E_+ maps exhibit clearly visible bands of strong field energy enhancement. The TM cases feature in each case a well-isolated steep band, which both have an obvious equivalent in the corresponding F_+ maps. The TE cases seem to feature a larger number of bands, which moreover show anticrossing. The color scale further points out that field energy enhancement values of up to 10 000 are present, which are correlated with peak width (FWHM) of 0.3 nm, as will be explained below. Note that this resolution is not reached in the experiment due to the laser bandwidth of 3 nm, which together with geometrical imperfections of the PhC reduces the observed fluorescence enhancement.

6.6 Selected field distributions and Q-factors

The E_+ maps of figure 30 give an overview of the illumination conditions that *potentially* lead to a fluorescence enhancement. But due to the included volume integral this is not necessarily the case. Yet, the *overlap* of the QDs and the increased energy densities has not been quantified. And unfortunately the exact distribution of the QDs is unknown.

To this end, figure 30 (bottom) shows the distribution of the field energy enhancement for selected conditions. The depictions are 3D volume renderings of the *local* electric field energy enhancement $E_{+,local}$, derived by normalizing the electric field energy density to the incident plane wave (which has a uniform energy density). The renderings are numbered according to the points 1 to 12 marked in the E_+ maps of the upper panel in the same figure. The positions of these points have been determined by maximizing E_+ using a root-finding algorithm. In this process, successive simulations are performed until a specified accuracy is obtained. The local electric field energy enhancement is rendered in the superspace domain, i.e. the cylindrical volume inside the hole and the hexagonal prism with a height of 250 nm above the silicon. $E_{+,local}$ is a dimensionless quantity and the volume integral over the shown domain equals to the complete electric field energy enhancement E_+ . The glass mesh is shown in blue and the silicon mesh is shown in gray, clipped in the yz -mirror plane to be able to look inside the hole. The same color scale is used for all maps, which is a trade-off between minimal clipping for high field energies and optimal visibility for weak field energy patterns. Large differences in the distributions are obvious: some modes tend to focus the energy inside the hole (e.g. 3, 5 and 10), while others concentrate the light at the plateaus between the holes (e.g. 6 and 9). Moreover, the depictions suggest that

Point #	λ_0 [nm]	θ [°]	Q-factor	FWHM [nm]
1	1095	29.05	245.35	4.46
2	1138	14.91	61.62	18.47
3	1134	19.38	777.97	1.46
4	1122	31.02	997.37	1.12
5	1115	40.14	564.26	1.98
6	1138	30.42	570.62	1.99
7	1130	26.94	2482.43	0.46
8	1110	25.39	521.45	2.13
9	1128	25.62	395.53	2.85
10	1100	21.94	470.33	2.34
11	1150	4.06	275.61	4.17
12	1131	8.93	238.57	4.74

Table 6.1: Results of the Q-factor analysis for the bands in the field enhancement maps. Each row corresponds to a point marked in figure 30 and for which the local field energy enhancement is shown in the same figure. The first column lists the label of these points. The vacuum wavelengths λ_0 and the incident angles θ are listed in columns 2 and 3. Q-factors obtained from Lorentzian fits are listed in column 4. The last column further lists the corresponding full widths at half-maximum (FWHM) of the peaks, which are related to the Q-factors via $\text{FWHM} = \lambda_0/Q$.

the differences in the enhancement factors are larger as it is seen from the E_+ maps. The latter is mainly due to the logarithmic color scale, but rather a natural limitation of this kind of plot.

In addition to the $E_{+, \text{local}}$ -renderings, table 6.1 lists the detailed coordinates and Q-factors of the points marked in figure 30. Each Q-factor was derived from a Lorentzian fit proportional to $1/[(\lambda - \lambda_0)^2 + (\lambda_0/2Q)^2]$ and a linear background. The Q-factors are proportional to the full width at half-maximum (FWHM) of the actual leaky mode resonance via $\text{FWHM} = \lambda_0/Q$, as outlined in section 2.2.6. This quantity will be considered in the discussion below.

6.7 Discussion

In the preceding sections a number of results of very different nature has been presented, which are all relevant for the explanation of the measured fluorescence effects. These results are presented in figure 30 and table 6.1. A “guide” of how to combine all these aspects to an interrelated reasoning could read as follows:

1. Select a feature in the fluorescence enhancement (F_+) maps and
2. check whether there is an according integrated field energy enhancement in the E_+ maps below. If this is true, the simulation actually suggests a possible excita-

tion enhancement effect. Otherwise, the measured fluorescence enhancement *might* not be explained by the numerical model.

3. Afterwards, observe the $E_{+,local}$ distribution corresponding to the point on the actual band that correlates to the measured effect (which is of course not possible for all features using the selected points). *If* the emitter distribution would be known, one should now check if the overlap between the emitters and the increased field explains the strength of the observed fluorescence enhancement. (In the present case, a consistent picture can only be gained by taking into account all cases.) If this is true, the effect is explained satisfyingly. Otherwise, take into account
4. the Q-factor of this band. Depending on the laser source bandwidth, Q-factors which are too high (corresponding to a very small FWHM) might impair the efficiency of the excitation, causing a smaller fluorescence enhancement than suggested by the field enhancement.

Accordingly, the steep bands for the TM-cases are clearly visible in the F_+ maps with a good accordance in their gradient angles and spectral positions. In the distribution render, point 9 shows a strong field which is located mainly above the silicon and ranges wide into the superspace volume. This explains its clear visibility in the fluorescence enhancement measurement ($\Gamma - M/TM$). The same is true for point 1 in the $\Gamma - K/TM$ -case, which has a higher field energy density than point 2, where no fluorescence enhancement is visible in the experiment. These accordances suggest that although the numerical model is a simplification of the actual system, the positions of the resonances regarding wavelength and angle of incidence agree qualitatively.

The $\Gamma - K/TE$ -case features two bands that show anticrossing in the measurement window. For the steeper band the field energy enhancement distribution is shown for points 6, 7 and 8, which exhibit huge field energies in a very large volume, e.g. an integrated enhancement factor of 7740 for point 7. This band is clearly visible in the measurement, as well as a gap correlating with the anticrossing point. The shallower band is vanishing in its field energy when moving to larger angles, as can be seen from the distributions for points 3, 4 and 5. Only at point 3, a comparatively large field in a large volume was found, which is in good accordance to the bright spot at about 10° and 1120 nm in the measurement. Finally, the $\Gamma - M/TE$ -case features two bright spots in the measurement which may correspond to the regions where the two bands show a strong bending at the anticrossing point, although shifted slightly outside the measurement window in the simulation. Shifts of that scale may still be explained by the uncertain distribution of the free OA for example. The continuation of the lower band through point 10 is not clearly seen in the measurement, which could be caused by the field energy distribution of this mode. The field energy is localized at two sides of the flanks of the hole, suggesting that the quantum dot density may be low on such very steep parts of the geometry.

Taking into account the Q-factors reveals another important aspect. Modes with smaller Q-factors (i.e. broader line widths) are more efficiently excited by the ≈ 3 nm broad laser source. Consequently, point 7 with a Q-factor of > 2400 (FWHM ≈ 0.46) does not result in a strong fluorescence enhancement effect, for example, although it has a considerably high energy. Similar conclusions can be drawn for other points with very high, or vice-versa with low Q-factors.

When assessing the achieved fluorescence enhancement with a maximum of about 50 %, it must be noted that it was not the concern of this demonstration to optimize the system in this regard, but to map and understand the achieved enhancement based on the PhC mode properties. From a comparison with Ganesh *et al.* [30], who achieved excitation enhancement of about 700 % in a similar system without a global optimization, it is clear that much larger fluorescence enhancements could be reached.

SO FAR, MANY OF THE EXPERIMENTAL OBSERVATIONS are consistently explained using the presented analysis. Using the E_+ maps, illumination conditions were determined for which leaky modes with a large *integrated* energy enhancement are excited. For selected illumination conditions, the *spatial* characteristics of the field energy density were analyzed. Using the energy distributions, some of the deviations between the measured fluorescence enhancement F_+ and the numerical field energy enhancement E_+ were explained. Using a Q-factor analysis, a mismatch between the spectral bandwidths of the leaky modes and the excitation laser source accounted for further deviations.

However, a few aspects remain unexplained, for example the nature of the elongated bright spot in the fluorescence enhancement of the $\Gamma - M$, TE case. Moreover, the distribution of the QDs can not be estimated from the results yet, which would be an additional outcome. The main weakness of the analysis technique is the consideration of only a small number of field distributions. The points for which the distributions are considered are partly arbitrary, and using a much larger number of distributions could become confusing.

In section 7.4, it will be shown that the remaining challenges can be met using a classification of modes based on their spatial properties. This classification can be obtained using clustering algorithms from the field of machine learning. The technique will reveal which parts of the E_+ maps of figure 30 correspond to modes with common spatial properties. Moreover, the method yields representative field distributions for the explanation of the measured fluorescence enhancement. The machine learning results will be combined with the results of this chapter to account for the aspects which are yet unexplained. Therefore, a detailed evaluation of the numerical techniques is saved for the following chapter (see section 7.5.2).

“Learning without thought is labor lost; thought without learning is perilous.”

—CONFUCIUS—

7

Classification of Field Distributions Using Machine Learning

IN THE FOLLOWING SECTIONS, the machine learning techniques introduced theoretically in section 2.3 will be used to classify field distributions from finite element method (FEM) simulations. In possible applications based on excitation enhancement there is a strong need to identify modes which have a large field energy enhancement *and* an appropriate field energy density distribution at the same time. This can be necessary in the design process, e.g. to tailor a photonic crystal (PhC) to possess a mode with maximum field enhancement and an optimum energy distribution, or in a subsequent analysis of actually measured effects. The common task is to “cluster” solutions with similar field distributions, so that the solution space is reduced to a small set of field distribution prototypes – which, loosely speaking, can be seen as “mode fingerprints”. In the end, these prototypes can be consulted as representative solutions to choose modes with the desired spatial distribution and, in the present case, they will be used to gain additional insight into the physics behind the experiments of chapters 5 and 6.

In the discussion of the fluorescence enhancement experiment of chapter 6 in section 6.7, the need for a systematical analysis approach of field distribution data was motivated. The challenge is to explain the deviations between the actually measured fluorescence enhancement F_+ on the one hand, and the simulated field energy enhancement factors E_+ on the other. The enhancement factors only allow for an assessment of the *integrated* field energy. For example, if a mode exhibits high field energy densities too close to the PhC surface, the overlap with the quantum dots (QDs) might be small. In the numerical analysis of chapter 6 only a small number of field distributions was considered, leaving parts of the deviations unexplained. Obviously, a more

rigorous interpretation of the experimental data necessitates to consider the field distribution at *any* configuration of the illumination conditions, i.e. for all directions of incidence, wavelengths and polarizations. But this parameter space is huge: supposing a rather low resolution of 100 wavelengths and 100 angles, the four combinations of polarizations and high-symmetry directions would effort to analyze 40 000 field distributions – possibly even in 3D. Even if this could be done “manually”, the volume rendering of the corresponding images would be computationally expensive.

The anticrossing experiment of chapter 5 was explained using an analysis of selected field distributions as well. The anticrossing behavior of two bands was explained by observing the coupling of modes, or the absence of coupling, in specific magnetic field distributions. Although the analysis did not leave aspects unexplained, the comparatively simple data is well-suited for testing purposes of the method which will be introduced in the following.

In the course of this chapter, a numerical method for the classification of PhC modes with respect to their spatial properties is developed. The method is based on clustering algorithms of the field of machine learning. First, the applicability is justified from theoretical considerations in section 7.1. Afterwards, the method is applied to the anticrossing experiment and explained in detail (sections 7.2 and 7.3). Finally, the method will be used to analyze the fluorescence enhancement experiment with a focus on the aspects that are still unexplained (sections 7.4 and 7.5).

As a preliminary note, the following sections partly contain explanations on the actual method of clustering – although these might belong to the methodical chapter 3. However, to the knowledge of the author, the presented approach has not been used for the classification of PhC modes before – or is at least a non-standard technique. Therefore, it is preferred to integrate a few methodical explanations here, as they are indispensable for the comprehension of the presented results (see section 2.3.1 for a basic example of clustering).

7.1 Justification of mode clustering

In the theoretical treatment presented in section 2.2, a number of expectations for the behavior of photonic bands was discussed. These expectations, which involve the spatial distribution of the related modes, also apply for the experiments of chapters 5 and 6. The modes that correspond to a single band are expected to exhibit well-behaved symmetry properties. For a fixed high-symmetry direction, e.g. $\Gamma - K$, we expect basically two types of solutions when scanning over wavelength and incident angle, which are

1. regions that correspond to leaky-mode bands, and
2. regions that are off any photonic band, and therefore corresponding to the continuum of radiation modes.

Reconsidering the explanations of section 2.2.5, the symmetry type of a photonic band will either stay constant when moving from one high symmetry point to another, or it will undergo a smooth transition from one type to another. The regions of the radiation modes are expected to exhibit solutions that couple to plane waves of the exterior domain, but which might partly be affected by a band when being close to it (or rather overlap with it). All things considered, only a small number of different symmetry types is expected, which is of the order of the number of bands that cross the parameter scan window.

This is where machine learning comes into play. In section 2.3 different clustering algorithms were introduced. If we consider the specific field distribution for a single illumination setting as the observation, the clustering technique is able to subdivide the *entirety* of field distributions into a finite number of *typical* field distributions – i.e. field distribution prototypes. This approach is reasonable because the following prerequisites are satisfied:

- The data range contains a finite number of typical field patterns (based on their symmetry properties) and each of the real field patterns can be identified with one of those prototypes, i.e. it only differs slightly from its assigned counterpart.
- These prototypes have a sufficient “uniqueness”, e.g. they considerably differ in their symmetry properties.

The remaining challenges are to find the proper number of clusters and to evaluate if the clustering gives a satisfactory description of the solution space. Both these issues will be covered in each of the specific cases below.

7.2 Clustering for the anticrossing experiment

In chapter 5, the symmetry dependence of anticrossing was analyzed both experimentally and numerically, using a *z*-asymmetric and a *z*-symmetric nanohole array sample. It was shown in two different ways, that the crossing properties of bands are affected by the purity of their (orthogonal) polarizations. A lack in orthogonality leads to an interaction of the bands near the crossing points, and hence anticrossing. Although the observed effects have been explained consistently, it is still possible to achieve more insight when using the clustering technique, as shown in the following. It moreover acts as a “clear case” to demonstrate the abilities of this approach, before applying it to a more complex case in section 7.4.

To be more precise, the analysis technique using a manual selection of field patterns has a number of drawbacks. Firstly, the specific points for which the fields are evaluated are partly random and need an additional maximization step to determine the peak center for each angle/mode combination. Secondly, as in this example, the observed distortions of the modes which couple can be quite unremarkable, i.e. may be

easy to overlook. Finally, only a xy -slice of the total 3D field was evaluated, which might neglect effects occurring aside this plane.

In this very specific case, we have two distinct setups, which are expected to cause very similar field patterns for the involved bands: the symmetric and the asymmetric one. Here, the idea is to learn the field patterns in a limited angle range for only the symmetric case, as it is expected from the previous analysis that the modes are more pure in their respective polarizations. The clustering algorithm trained in this manner should then be used to recognize the modes for the residual data, known as “prediction” in the machine learning vocabulary. The resulting classification should reflect the positions of the two target bands and reveal the interaction based on the distance from the cluster centers in the anticrossing zone.

7.2.1 Constructing the clustering data

As explained in detail in section 2.3, the clustering is executed on an input matrix X of shape $N_s \times N_f$, where N_s is the number of *samples* and N_f the number of *features*. The features, in the present case, are absolute values of the magnetic field components H_j with $j \in \{x, y, z\}$ for a number of points $\mathbf{r}_i \in \mathbb{R}^3$, i.e. of the form $|H_j(\mathbf{r}_i)|$. Consequently, if the field is evaluated at N_p points, these are $N_f = 3N_p$ features. To avoid exporting the magnetic field on a full Cartesian grid in 3D, which would cause huge amounts of data when trying to achieve a reasonable resolution, data is only exported on a number of symmetry planes; here, the xy -, xz - and yz -planes. More symmetry planes could be used as well, but based on these three planes a reasonable classification can be reached (this was tested using smaller data sets, comparing to a full 3D field output). Obviously, a field pattern of a single simulation is a 4D data set, holding data for each spatial direction and each component j of the magnetic field. As each sample X_i must be a 1D row vector with observations of single scalar values x_0, \dots, x_{N_f-1} , it is necessary to flatten these data sets in always the same way, yielding “1D representations” of the fields.

This field export is performed for each point in each map of figure 26, column 4, so that the samples are unique simulations for a given symmetry case, wavelength λ and incident angle θ . As a side note, it is an additional challenge to keep the amount of data small enough to store and analyze it in a reasonable time. The number of samples for a single symmetry case is given by $N_s = N_\lambda \cdot N_\theta$. Therefore, the size of the input matrix becomes large if a high resolution in both input parameters *and* the field export is desired.

7.2.2 Learning the field patterns for the symmetric case

Once the magnetic field data is generated and stored (in a compressed and highly accessible database), the input matrices X can be assembled. For the clustering the very stable k -means algorithm is used, which scales well to large number of samples and which was introduced in section 2.3.4. The task is now to learn the field patterns of the

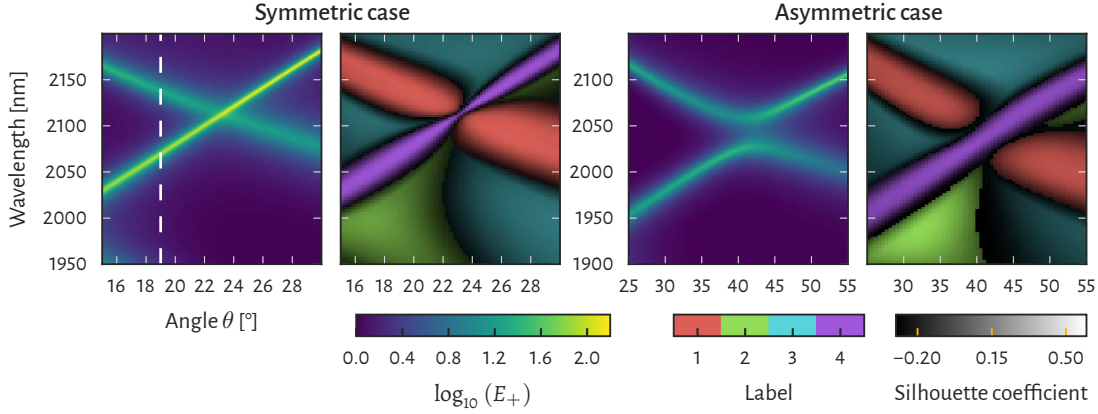


Figure 31: Comparison of field energy enhancement E_+ and classification maps for the symmetric and asymmetric cases. (Columns 1 and 3) Repeated results from the last column of figure 26: the E -field energy enhancement E_+ (left color bar) is shown as a function of the vacuum wavelength (y -axis) and incident angle θ (x -axis). The white dashed line in column 1 marks the angle θ_c up to which the classifier was trained. The quantities of the axes apply for all columns (see figure 9 on page 49 which indicates θ). **(Columns 2 and 4)** Classification maps depicting the cluster labels using different colors (center color bar) and the silhouette coefficients using alpha-blending with a black background (right color bar). More saturated colors denote larger silhouette coefficients.

symmetric case in a limited angle range, in order to avoid a strong deformation of the modes when approaching the next high-symmetry point. The k -means algorithm is executed using a “fitting set”, for which a matrix is composed using the magnetic field distributions for all points with angles smaller than a critical angle θ_c . To choose θ_c , it must be considered that smaller values will reduce the fitting set size, thus limiting the convergence of the clustering, while larger values lead to a stronger modification of the modes. It is reasonable to stay well below the crossing point to avoid patterns that contain superpositions of two bands. A good choice was found for $\theta_c = 19^\circ$, small changes $\pm 4^\circ$ were found to be uncritical.

7.2.3 Mode classification

The overall results of the clustering process are shown in figure 31. The two plots on the left-hand side belong to the symmetric case, the others to the asymmetric case. For each case, the field energy enhancement E_+ from figure 26 is again shown on the left (using the left color bar), while the clustering result is shown on the right. These plots (column 2 and 4) will be referred to as “classification maps” in the following. The white dotted line in the left plot of the symmetric case marks the critical angle, i.e. the field patterns for the data points left of that line have been used to obtain the cluster centers.

The k -means was performed with $N_k = 4$, yielding 4 cluster centers where each is assigned to a label k . The centers can be thought of as “mode fingerprints”, as will be illustrated shortly. The fitted algorithm was then used to assign each field pattern for

the data at the right of the dashed white line in figure 31 to the best matching cluster center, thus to label it (prediction step).

The same was done for the asymmetric case, which is expected to exhibit very similar mode profiles for the related bands. So it may be stressed here, that the k -means algorithm was *not* applied again for the asymmetric case, but rather the trained classifier was used to predict the mode labels. The resulting classification map is shown in column 4 of figure 31.

The classification maps depict the labels using different colors for each cluster k , shown in the center color bar. For the moment, we may ignore the blackish alpha blending in the plots and concentrate solely on the colors. For the symmetric case (left), it can clearly be seen that the two bands of the energy enhancement plot are identified with labels “1”, for the weaker band ranging from $\approx [15^\circ, 2160 \text{ nm}]$ to $\approx [30^\circ, 2060 \text{ nm}]$ (red); and label “4”, for the stronger band ranging from $\approx [15^\circ, 2040 \text{ nm}]$ to $\approx [30^\circ, 2180 \text{ nm}]$ (violet). The regions aside the photonic bands are split into two areas labeled with “2” (green) and “3” (cyan).

For the asymmetric case, we effectively find the same class assignment of the two bands as for the symmetric case with labels 1 and 4. This is an important result, as it confirms the initial expectation that both cases exhibit very similar mode profiles. But now this is not only shown for randomly chosen points, as done before in section 5.4, but for the complete maps and under consideration of multiple planes of the magnetic field distributions. The relation even holds for the regions without photonic bands. But before the classification plots will be discussed in detail, the problem of how to measure the representation quality will be addressed, which will also involve the blending in the classification maps.

7.2.4 Measuring the quality of the class assignments

In addition to the color-coding using the labels, there is a layer of alpha-blending with a black background in the classification maps. The k -means algorithm does not support probabilistic outputs, that is it can only provide “hard” decisions for the classes to which a sample belongs. But the representation using the cluster centers is of course not equally good for all samples. In other words, each sample has a different distance from the cluster center.

As a tool to estimate the representation quality of a sample X_i^k by its cluster center μ_k , the *silhouette coefficient* $s(i)$ was introduced in section 2.3.6, and defined in equation (2.51). The silhouette coefficients were used to calculate the alpha-value, i.e. the transparency assigned to each point in the classification plots. It is described using the right color bar in figure 31, indicating that a more blackish color corresponds to lower values of s , while more saturated colors correspond to higher values.

To understand the information which is visualized in that way, we will repeat parts of the explanation of the silhouette coefficients from section 2.3.6. The coefficient $s(i)$

is calculated using the ratio between the average dissimilarity of X_i^k to all other samples of the class k , and the minimum average dissimilarity of X_i^k to all samples in the other classes $j \neq k$. In short, values of $s(i)$ near $+1$ indicate that the sample is *well-clustered*, while a value close to 0 indicates that the sample is close to the border of the neighboring cluster, so it is an *intermediate case*. If $s(i)$ is close to -1 , it seems more likely that X_i belongs to its neighboring cluster, so it was probably *misclassified* (compare [71]). Considering these features of the silhouette coefficients, it is possible to discuss the classification maps in detail.

7.3 Discussion (part 1)

If we compare both classification maps in figure 31, we can see that the red and violet areas are getting much closer to each other in the **symmetric case** than in the asymmetric case. We expect a superposition of the mode profiles at the crossing point for the former case, and, from the enhancement plots, the band with the positive slope is expected to be dominant with regard to its field intensity. The violet area is getting very slim at the crossing point, revealing the extreme narrowness of the band with label 4. However, it indeed dominates and is thus “cutting” the red band with label 1.

This behavior can be understood when considering the parts where the bands are isolated. Here, the band is surrounded by very small field intensities, so that even in the regions where the band fades, it will dominate the background. Therefore, the bands appear broader compared to the enhancement maps. Once the bands cross, the classifier must choose between two very strong patterns, revealing the *actual* width of the bands.

Another important aspect (– still considering the symmetric case –) is the silhouette coefficient mapping. We observe that the saturation decreases at the border of two clusters. This is expected, as silhouette scores close to 0 indicate a sample which is in fact close to the border of the neighboring cluster (compare section 2.3.4 or [71]). The important part is again at the crossing point: here, the blackish separation between the clusters is extremely narrow, and this supports the interpretation of a “lack of interaction” between the bands. If an interaction were present, it would be expected that the bands affect and distort each other, leading to large black regions where none of the classes is a good representation for the actual field (negative silhouette scores). If no interaction takes place, the classes will be valid representations until the actual superposition occurs, where one of the bands will dominate. This is in exact agreement with the observation.

Moving to the **asymmetric case**, we observe exactly the picture drawn before for an *existing* interaction. Here, the red and violet clusters are much more separated at the anticrossing point, and we also observe a bending of the bands. The blackish areas between the clusters are broader, stemming from a distortion of the field patterns to

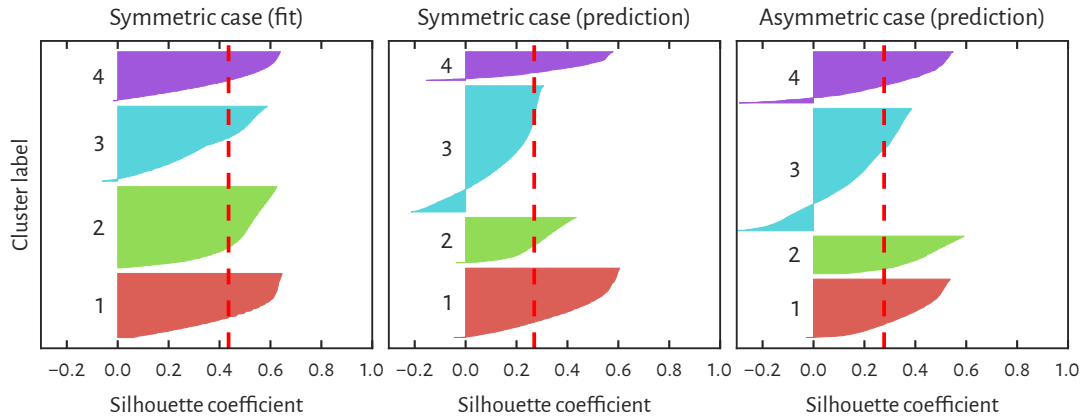


Figure 32: Silhouette analysis plots for the fitting and prediction steps of the symmetric case, and for the asymmetric case. Silhouette coefficients for each sample are plotted as a bar in x -direction with a length corresponding to its value. The samples are sorted by their silhouette coefficients, with smaller values being located at smaller y -positions; and grouped and color-coded using the same colors as in figure 31. Red dashed lines mark the silhouette scores.

which none of the cluster centers is a good fit. The violet band appears much broader than in the symmetric case, although this is not expected from a physics point of view. After all, the band’s widths are in accordance far from the crossing/anticrossing points, – as expected. This again supports the interpretation that an interaction is present, as the classification simply “snaps” to the violet cluster in broader regions where the distorted fields are more similar than to the red cluster.

7.3.1 Validating the clustering model

The previous discussion showed that the clustering results are in accordance with theoretical expectations. But before we investigate the cluster centers, the quality of the clustering itself is evaluated using a mathematical analysis in the following. This can be done using the silhouette coefficients again, using a scheme known as “silhouette analysis”. It will not only validate the choice for the number of clusters, but also allow for another view on the physical phenomena.

Figure 32 shows the typical plots for this analysis technique [71], providing a visual aid for the interpretation of the clustering. In each of the three plots, the silhouette coefficients for each sample are plotted as a “bar” in x -direction with a length corresponding to its value (negative values point into the $-x$ -direction). The samples are sorted by their silhouette coefficients, with smaller values being located at smaller y -positions. In addition, the samples are grouped for each cluster k and color-coded using the same colors as in figure 31. The red dashed lines mark the average of all silhouette coefficients, which is a measure for the absolute quality of the representation denoted as “silhouette score”. The results are the typical “sails” or “shark fins” and are

shown (from left to right) for

- the fitting part of the symmetric case *left* of the white dashed line in figure 31,
- the prediction part of the symmetric case *right* of the white dashed line, and
- the asymmetric case, which is completely predicted.

Only the fitting part of the symmetric case will be considered for the quality assessment of the clustering, as this is the part for which the actual k -means algorithm was executed. Deviations are expected when moving to higher angles. This is directly obvious from the silhouette score, which is ~ 0.4 for the fitting case and only ~ 0.25 for the prediction cases. Although an expectation for the absolute value of the silhouette score can not be given here, it can be stated that 0.4 is satisfactory as it is clearly positive. The smaller values for the prediction cases are as expected, because of the large areas with superpositions of modes and possible perturbations caused by coupling effects.

Considering the *distribution* of the silhouette coefficients, fins which are not too sharp are observed in the **left-hand plot**, i.e. having broad plateaus of high silhouette coefficients. There is only a minimum number of values with negative coefficients. Both arguments together give a validation for the fact that the number of clusters is not *underestimated*: negative values would occur if there were too few clusters, leaving back samples which do not fit in one of the classes ($s(i) \sim -1$). Too many clusters could be identified by a large fluctuation in the fin widths. But this does not fully apply here, as the areas occupied by the bands and the residual parts are unequal. Therefore, equally broad classes are not expected. Instead, the band clusters 1 and 4 are expected to be comparable in size, which is fulfilled in the silhouette plot. Also, a slightly too large number of clusters can be seen as unproblematic, because it would basically subdivide the radiation mode regions further, which are of limited relevance for the interpretation. Another point that suggests a good representation is that there are no clusters with below average silhouette scores.

The **center plot** in figure 32 shows the silhouette analysis for the prediction part of the symmetric case. The representation quality for the band clusters 1 and 4 is nearly unaffected, while the clusters for the offside-band parts degrade. This is a possible behavior, as the offside regions are expected to be affected by nearby bands and, therefore, may change when moving to higher angles. The negative values in the violet and blue clusters are caused by the crossing zone of the band. Here, the field distributions which contain superpositions are mapped to any of the adjacent clusters without being a good match.

Finally, the **right-hand plot** for the asymmetric case shows stable assignments for the band clusters as well. There are even broader ranges of negative coefficients, which is expected from the increased interaction of the bands. The distorted fields at the anticrossing point are expected to fit badly into the classes learned from undisturbed bands. The silhouette analysis hence gives another validation for the accordance between the clustering and the observed physical phenomena.

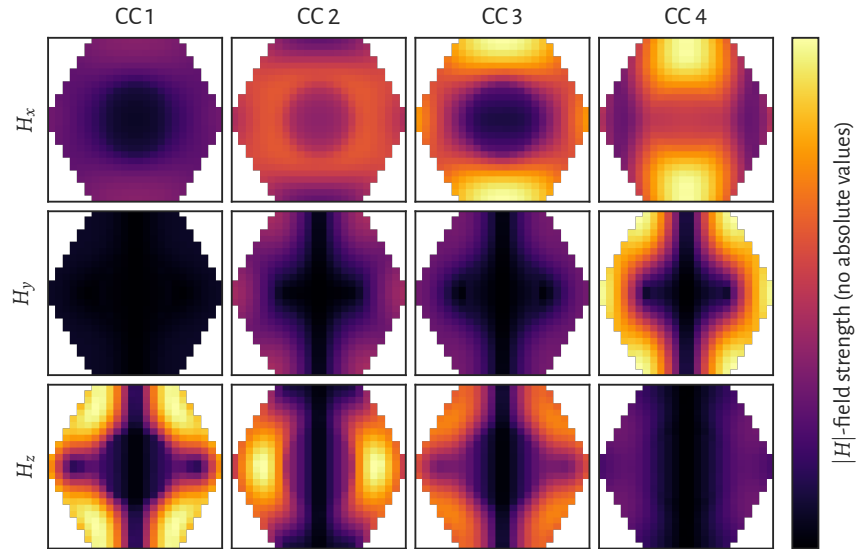


Figure 33: Magnetic field prototypes on the xy -plane obtained from the cluster centers. Magnetic field (H) distributions for the four cluster centers in the xy -plane as obtained from the k -means classification (x dimension on the x -axis, y dimension on the y -axis). Rows correspond to the absolute values of the x , y and z -component of the magnetic field, respectively. The field strength is color-mapped (color bar at the right). Columns correspond to the cluster centers (CC) of the related classes identified by the label. Absolute values are omitted as the centers are based on standardized data. Compare these patterns to figure 27.

7.3.2 Cluster centers: the field pattern prototypes

Finally, besides revealing the crossing/anticrossing using the classification maps of figure 31, the machine learning approach has an additional outcome: the cluster centers. In the present case, these centers can be thought of as the average field distribution for all samples which are grouped into a class. In consequence, they represent field pattern prototypes.

The prototypes contain the information of all of the three planes on which the H -field was exported in the underlying simulations, namely the xy -, yz and xz -planes. The full 3D fields could have been used just as well to achieved full-3D prototypes, although much more computationally costly. To compare the resulting prototypes to the randomly chosen distributions presented in figure 27, we show the xy -plane of the cluster centers in figure 33 (here: CC=cluster center). The prototypes for the bands with labels 1 and 4 are therefore shown in columns 1 and 4 of the figure, respectively. If these are compared to the exemplary distributions of figure 27, i.e. columns (a) and (b) of the symmetric case with clusters 1 and 4, we observe a very good accordance. The example points fit absolutely well into their respective classes, again validating the clustering approach. In the next chapter which addresses the fluorescence enhancement experiment, the cluster centers will be of even greater importance.

7.4 Clustering for the fluorescence enhancement experiment

The previous sections gave an impression of the abilities of the clustering approach by analyzing maps with windows that feature a small number of broad, well-isolated bands. The techniques and the reasoning presented there can similarly be applied to the fluorescence enhancement experiment of chapter 6, as presented in the following. The objective is to demonstrate that the clustering approach provides a more rigorous and complete picture of the underlying effects and explains observations which are yet unaccounted. The main weakness of the argumentation in chapter 6 is that it is based on rather arbitrarily chosen points in case of the field distributions and Q-factors (see figure 30). This is solved using the clustering technique, which takes into account the field distributions on *any* point in the shown E_+ maps.

Due to the similarity to sections 7.2 and 7.3, the methods and the reasoning of the analysis are not repeated in the same depth, so that the reader is referred to these sections for further information. Also note the introductory statements at the beginning of this chapter, and the theoretical justification in section 7.1.

7.4.1 Specifics of the clustering procedure

In contrast to the approach used for the anticrossing experiment, the clustering in the present case does not include any prediction steps, i.e. it is carried out for the complete angle and wavelength range of the E_+ maps in figure 30. It further considers the electric field instead of the magnetic field, which most likely leads to the same classification, but results in cluster centers for the electric field.

However, the main difference is that the maps include extremely narrow bands. When the choice for the k -means clustering algorithm was reasoned before, the main mentioned advantages were its robustness and simplicity. As mostly, this comes at a price, which in this case is its limited flexibility. In fact, k -means assumes that the clusters are *circular*: it simply uses a hyper-spherical volume, whose center is nothing but the considered cluster center, and whose radius is defined by the most distant member of the class. But for the present application it is not guaranteed that the clusters are circular, especially because we deal with clusters of very different size.

It is therefore necessary to use a more advanced approach known as Gaussian mixture model (GMM) clustering. This method, which was introduced in section 2.3.5, assumes that the data is composed of a mixture of Gaussian probability distributions in the multidimensional feature space. It is often considered as a generalization of the k -means method that takes into account the covariance structure of the data. The greater flexibility in the cluster sizes and shapes makes the GMM clustering algorithm better suited for the present task.

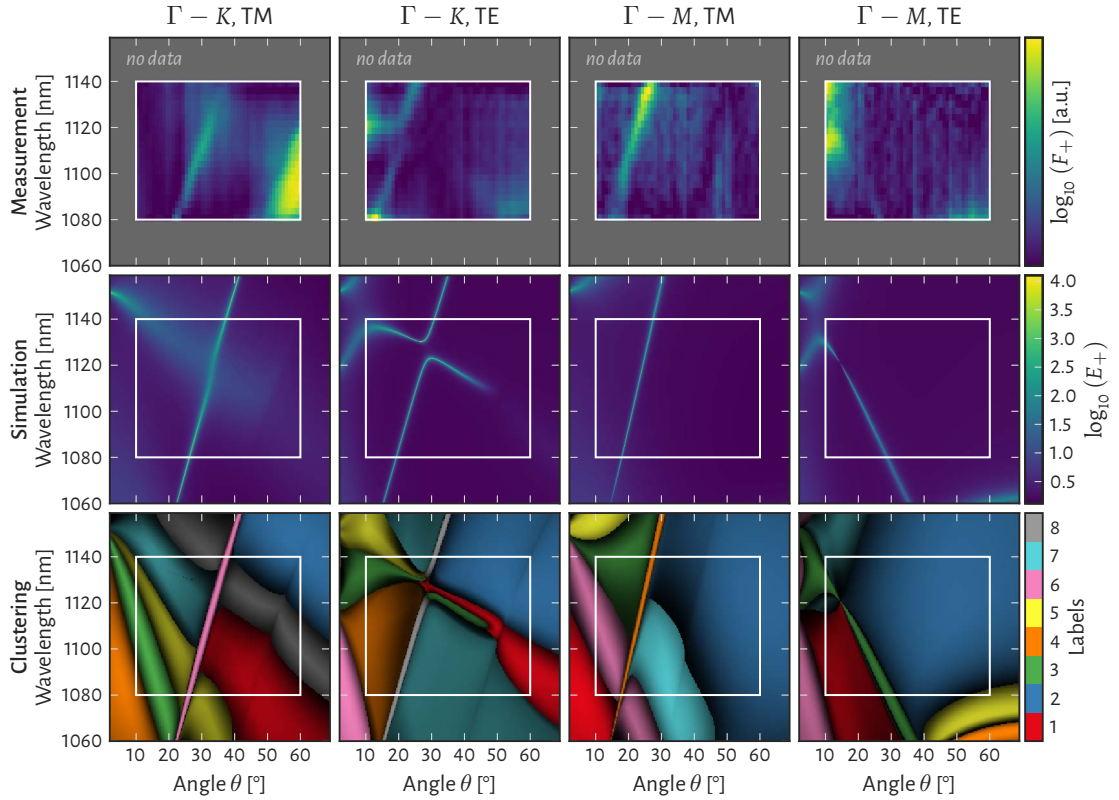


Figure 34: Clustering results for the fluorescence enhancement experiment. The upper and the center rows of the panel repeat the same results as already shown in figure 30 (top, see the corresponding caption for further details) for a larger angle and wavelength range. The lower row depicts the classification maps in the same way as in figure 31. The colors represent the cluster assignments (independently for each plot), while the the alpha-blending (“blackishness”) accounts for the silhouette coefficient (color bar omitted).

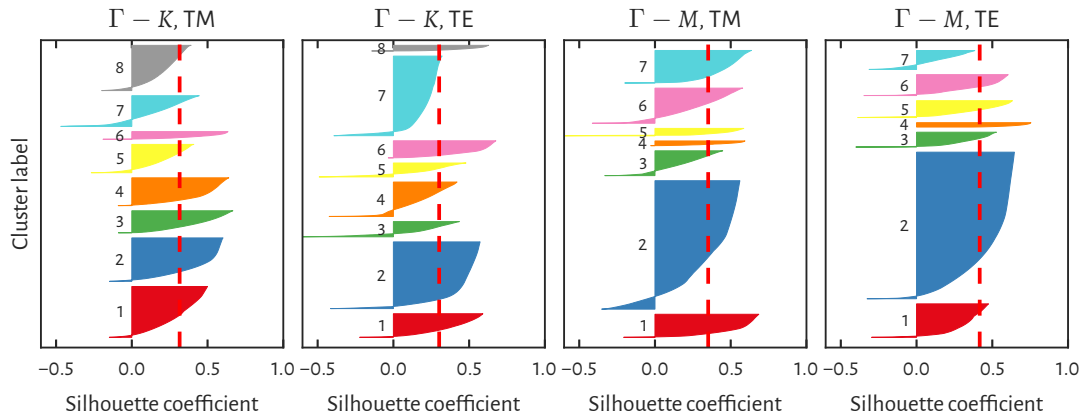


Figure 35: Silhouette analysis plots for the different direction/polarization combinations. For each combination of direction and polarization (columns), the silhouette plots are shown in the same way as in figure 32 (see the corresponding caption for further details).

7.4.2 Classification maps and silhouette analysis

The clustering was performed for each of the direction/polarization combinations independently, considering the normalized absolute electric field distributions on equally spaced points on the xy -, xz - and yz -planes. For the wavelength and angle resolution, values of 0.5 nm and 0.3° have been used, respectively. Consequently, for each clustering the input matrix X had a size of $N_s \times N_f = 47\,034 \times 8616$, where N_s is the number of samples and N_f the number of features. This is a comparably large problem size, especially because the clusters have a dimensionality of N_f , so that the procedure took more than 10 hours on a hexa-core workstation with roughly 40 GB of memory consumption. The optimum number of clusters was determined using a reduced data set for each combination individually, considering the silhouette plots to evaluate the representation quality (see section 7.3 for details of the reasoning).

The final classification maps are shown in the lower row of figure 34. The top and center rows of the same figure repeat the results that have been presented in figure 30 on page 100, but using a larger wavelength and angle range. As before, the white rectangles indicate the experimental data limits, showing that the simulation allows to see effects beyond that window. The classification maps in the lower row depict the class assignment, i.e. the label for each point in the maps by color-coding. Note that the classification maps cannot be compared among each other, although the same colors have been used. The quality of the representation by the assigned cluster for each point has been measured using the silhouette coefficient, which was used to calculate the alpha-blending using a black background in the maps (color scale omitted). The clusterings for the $\Gamma - K$ -cases used 8 clusters, while the $\Gamma - M$ -cases only required 7 (i.e. there is no gray region in these maps).

Figure 35 depicts the silhouette plots for each combination, using the same column order as in figure 34. Just as in section 7.3, the silhouette coefficients for each sample are plotted as a bar in x -direction with a length corresponding to its value. The samples are sorted by their silhouette coefficients, with smaller values being located at smaller y -positions; and grouped and color-coded using the same colors as in the corresponding classification maps of figure 34. The red dashed lines indicate the silhouette score, which is the average of all silhouette coefficients (see section 2.3.6). The width of each “fin” in the silhouette plots is proportional to the area of the correspondingly labelled points in the classification maps.

When concentrating on the narrow bands of high field enhancement in the E_+ maps, corresponding narrow areas are visible at the same positions in the classification maps as well. Recall that the E_+ maps and the classification maps are based on completely different data sets! The former are derived from an energy density integration in the superspace volume only, while the latter uses electric field patterns on planes that include the PhC and glass domains. The accordance is therefore astonishingly well. These clusters are moreover found by the GMM algorithm although they have much

smaller sizes, as also seen in the silhouette plots.

When observing the regions off the narrow leaky-mode bands, i.e. the domains of the radiation modes, it is seen that these regions are multiply subdivided in some cases; e.g. $\Gamma - K$, TM: bottom left. In contrast, other parts are homogenous over large ranges, such as $\Gamma - M$, TE: top right.

7.4.3 Cluster centers

The second essential outcome of the clustering procedure is the cluster centers, i.e. the field distribution prototypes, this time for the electric field. As the input data for the GMM algorithm have been electric field values on three planes, namely xy , xz and yz , the prototype data is available on these planes as well. Before the (quite large amount of) data will be discussed coherently in the next section, these cluster centers are given as well. To this end, the field distribution prototypes for all clusters of each combination and on all three planes are depicted in figures 36 to 39 on the following full-size pages. A full caption is omitted below these figures for reasons of space, but is rather given in the list below.

To ease the comprehension of the plots, and especially the comparison among them, a number of guides have been introduced. The following list gives an overview of all the aspects related to the plots that deal with clustering:

- Each cluster center overview figure, denoted as **prototype map** in the following (e.g. figure 36), is organized in three **panels** for the xz , yz and xy planes, respectively (from top to bottom), separated by horizontal black lines.
- Each of these panels has the same number of **columns**, accounting for the number of clusters, and each column has a **colored edge** in the top-most row that corresponds to the color used for that label in the cluster maps shown in the lower row of figure 34. The cluster center (CC) label is further given in the title of the xz -panel.
- Each of the panels has four **rows** of which the top row shows the electric field energy distributions $\|\mathbf{E}\|^2$, while the other three rows show the distributions of the x -, y - and z - component of the E -field, respectively (from top to bottom).
- The aspect ratio of the individual **distribution plots** accounts for the actual aspect ratio of the system in that plane. The yz plots are therefore wider than the xz plots (see figure 9 on page 49).

(Continued on page 125)

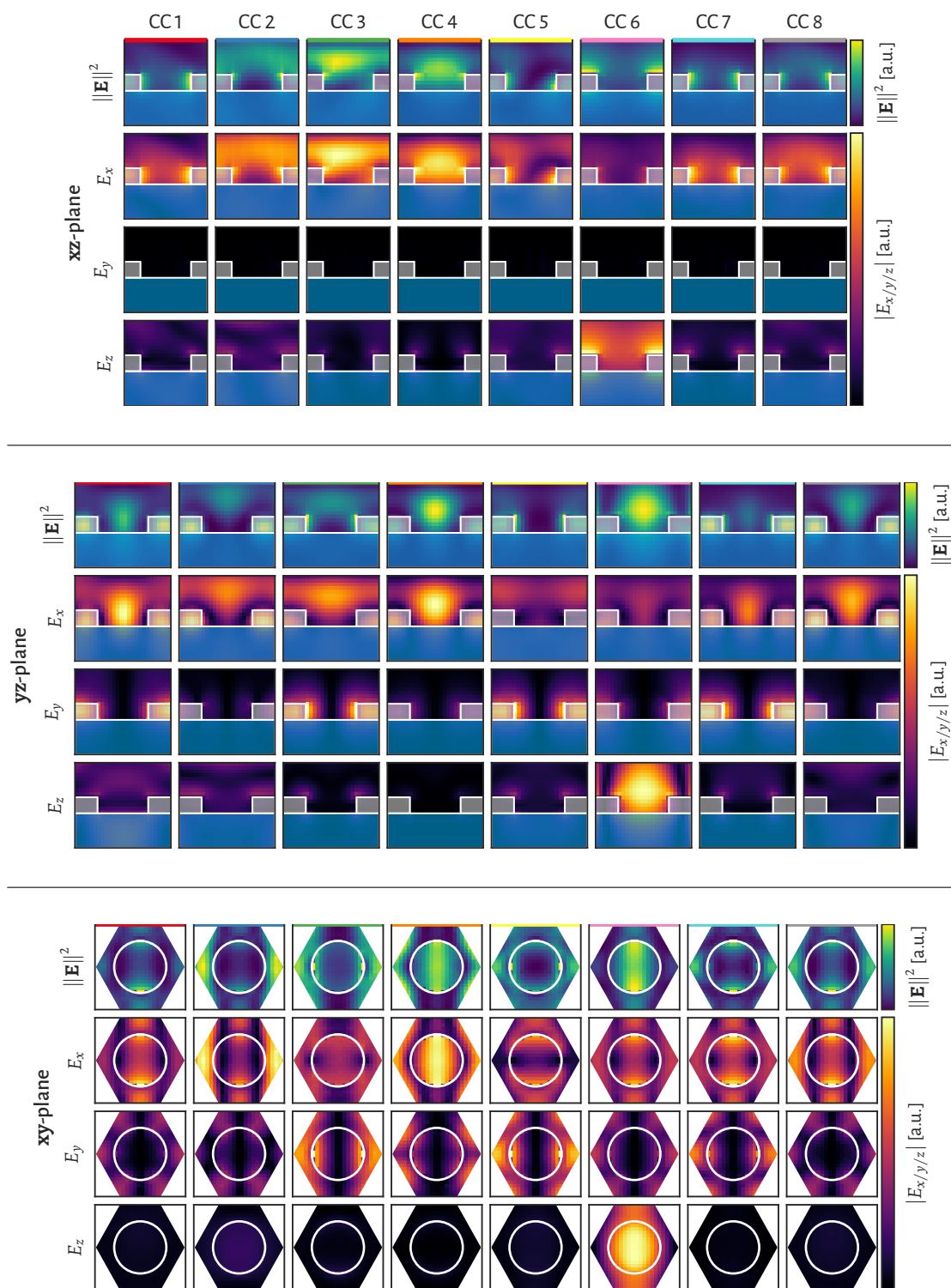


Figure 36: Prototype map for $\Gamma - K$, TM. Due to space restrictions the figure description is given in the list on page 120.

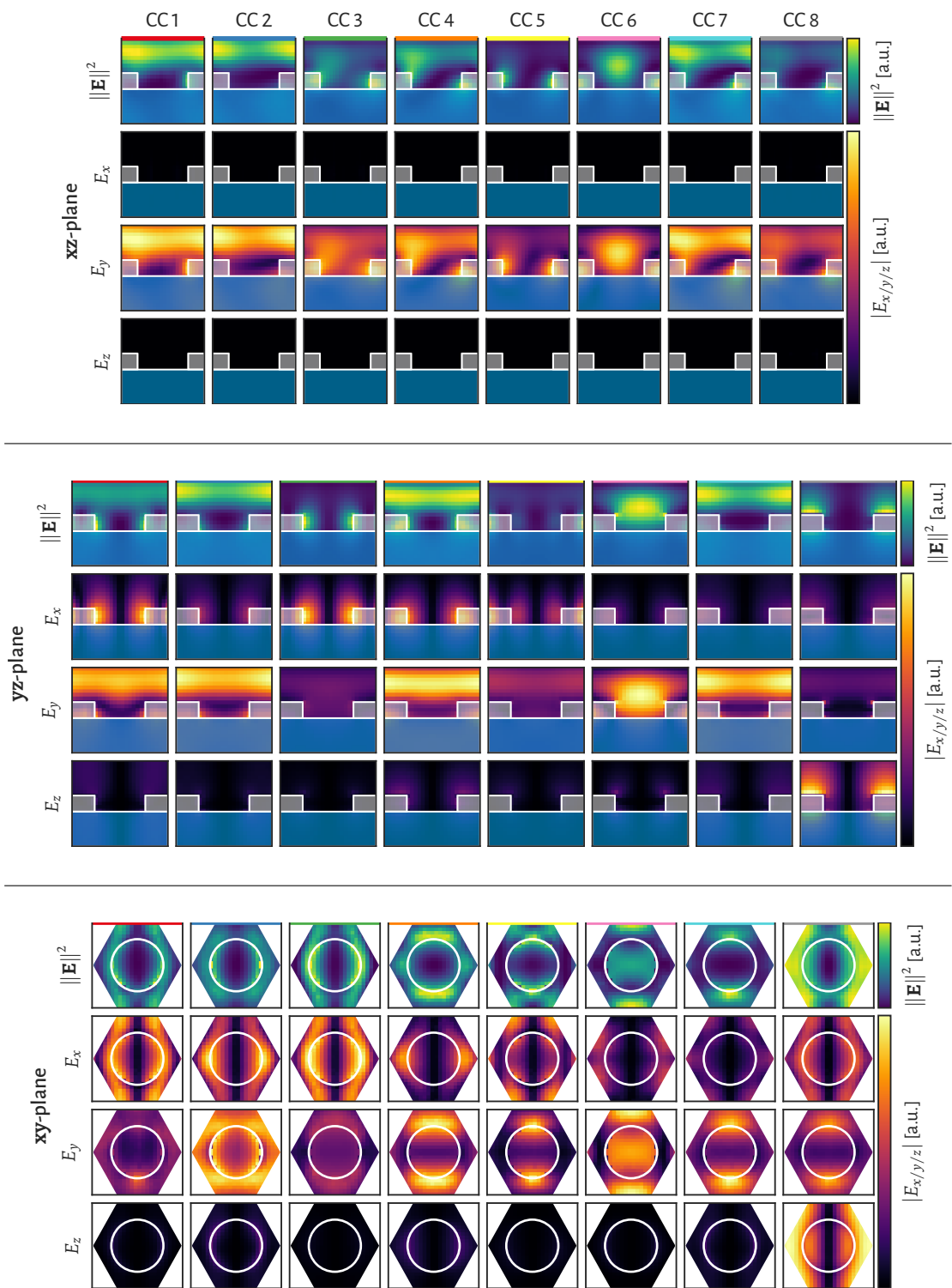


Figure 37: Prototype map for $\Gamma - K$, TE. Due to space restrictions the figure description is given in the list on page 120.

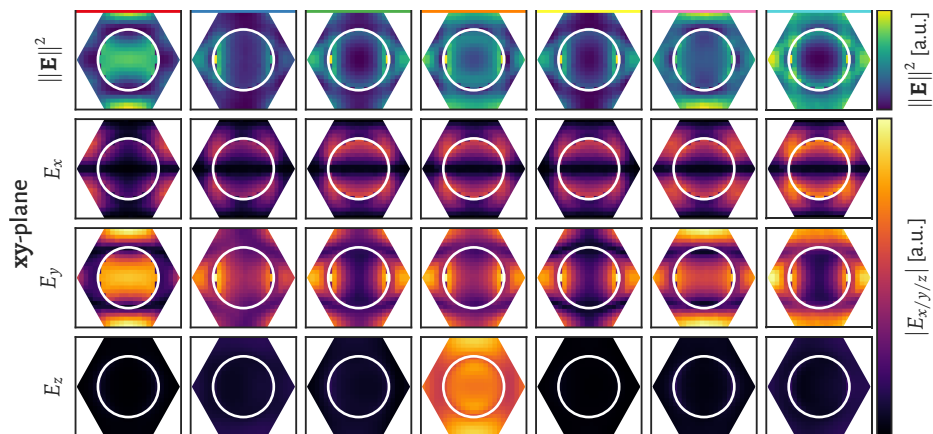
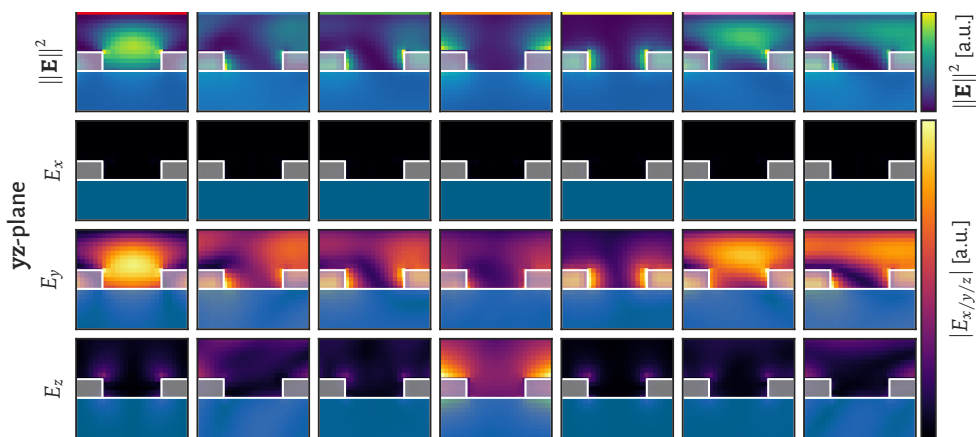
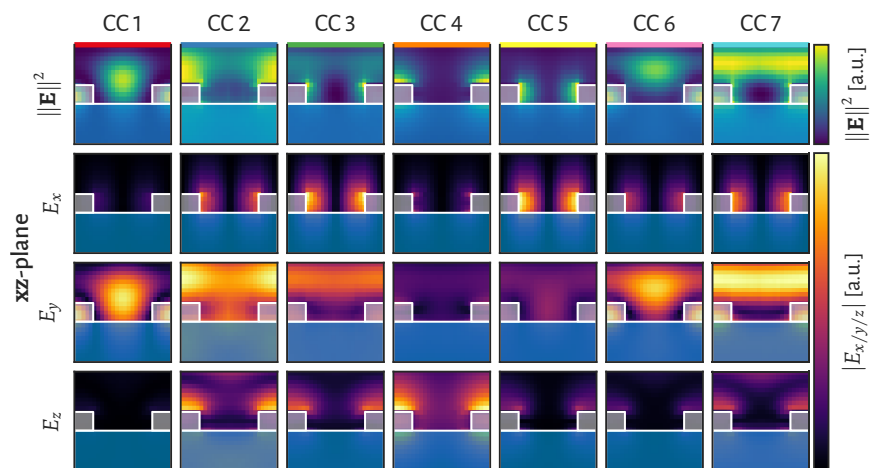


Figure 38: Prototype map for $\Gamma - M$, TM. Due to space restrictions the figure description is given in the list on page 120.

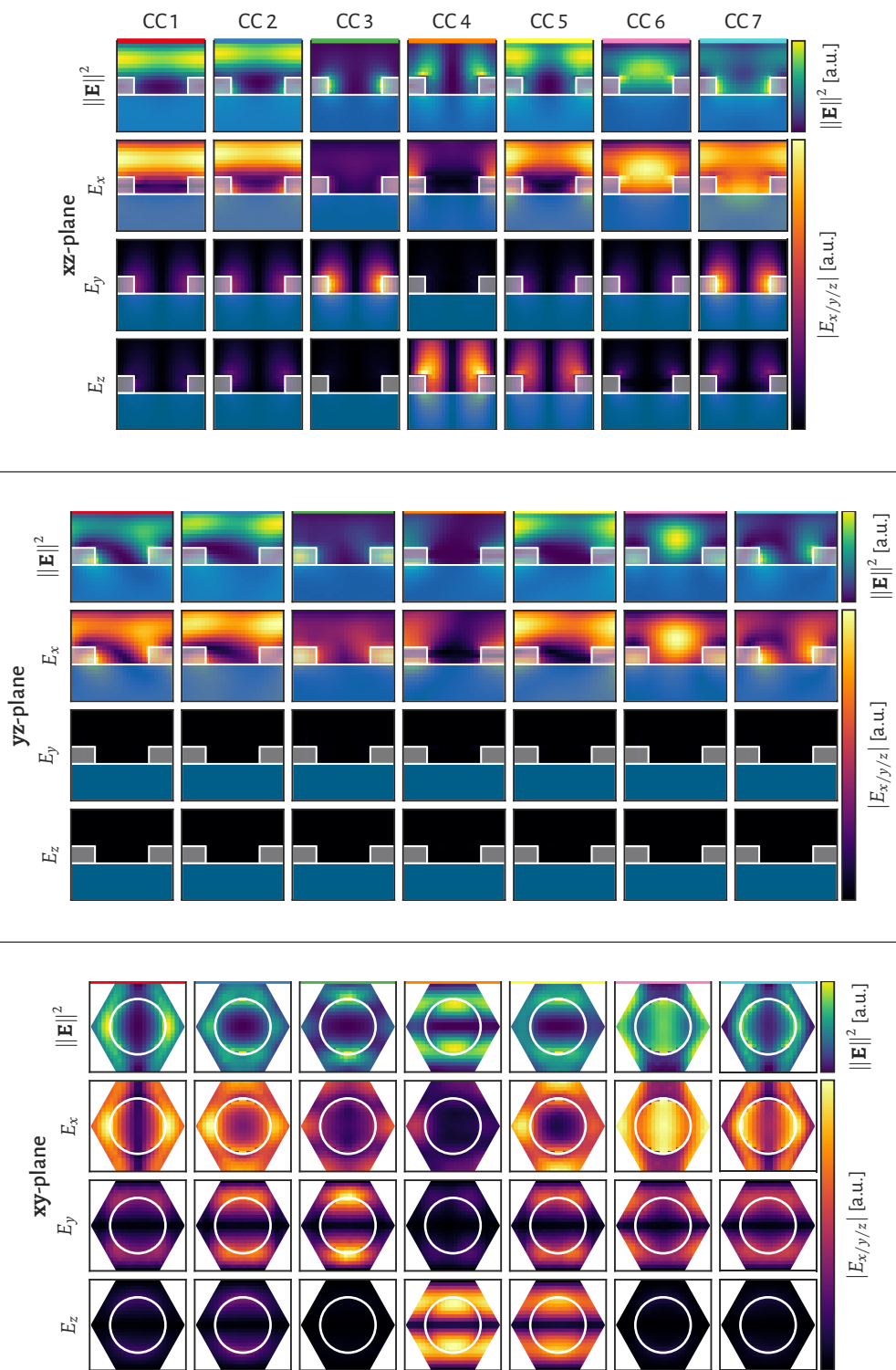


Figure 39: Prototype map for $\Gamma - M$, TE. Due to space restrictions the figure description is given in the list on page 120.

(Continuation from list on page 120)

- Furthermore, the distribution plots feature **semitransparent markings** for the glass superstrate (blue) and the silicon of the PhC (gray) in the case of xz and yz ; and a white circle indicating the hole circumference in the case of xy .
- Finally, it is noted that the **color scales** do not give absolute values, as the cluster centers are based on normalized data and are therefore not comparable among each other. However, the three E -field components for each column and each plane are comparable.

Because of the amount of information provided in these figures, it is of limited value to give further descriptions of the observed features without considering the supposed explanation. This part is therefore integrated into the discussion part below, which tries to give a coherent interpretation.

7.5 Discussion (part 2)

In this final discussion section, a complete analysis of the clustering results for the fluorescence enhancement experiment will be given, followed by an evaluation and summary of the method itself. At first, the objective is once again to explain the observed fluorescence enhancement shown in the upper maps of figure 34 using the numerical data. The latter, here, consists of the (i) field energy enhancement maps (E_+ , figure 34, center), the (ii) classification maps (figure 34, bottom) and the prototype maps (figures 36 to 39). An explanation for the same experimental data was already given in chapter 6 using selected field distributions, and the numbered list on page 103 gave a *guide* on how the different aspects of the results can be connected to yield a complete interpretation. This guide can now be updated in the following way, using the clustering results instead (steps 1 and 2 remain unchanged and are repeated here):

1. Select a feature in the fluorescence enhancement (F_+) maps and
2. check whether there is an according integrated field energy enhancement in the E_+ maps below. If this is true, the simulation actually suggests a possible excitation enhancement effect. Otherwise, the measured fluorescence enhancement *might* not be explained by the numerical model.
3. Afterwards, observe the corresponding region in the classification maps and determine the cluster label from the color using the color bar.
4. Using this label or color, locate the related column in the prototype map that belongs to the direction/polarization combination (the prototype maps are ordered according to the columns in figure 34, from left to right). Check if the field distributions on the three planes can explain the observed fluorescence enhancement (this may necessitate to take into account all cases, because the QD distribution is unknown).

- (5. Optionally, in some cases the Q-factor information of table 6.1 may be useful as it takes into account the coupling quality between the excitation laser and the mode. This information can not be gained from the clustering results.)

7.5.1 Systematic analysis of the clustering results

Based on the strategy given in the updated guide in the list above, the data will be analyzed systematically in the following. To avoid confusion, only one combination of high-symmetry direction and polarization will be discussed at a time.

$\Gamma - M, TM$

Let us start with the clearest case: $\Gamma - M, TM$ (column 3 and figure 38). The F_+ maps feature a single stripe of increased fluorescence with a high contrast. This stripe excellently corresponds to the single leaky-mode band causing a high field enhancement in the E_+ map. The classification map reveals this band accordingly with label 4 (orange), for which the field distributions are shown in column 4 of the prototype map. The xz and yz patterns show that the energy of this band is accumulated at the *plateaus* between the holes and caused by the E_z component. When observing other columns of the prototype map, there are other interesting patterns which could potentially increase the emission of the QDs, for instance in columns 1 and 5. These two modes gather their energy in the *center of the hole* and at the *flanks*, respectively. However, when looking at the classification maps again, these correspond to the red and yellow regions, which are (unfortunately) outside the measurement window. Another important point is given by the patterns of solutions that are related to radiation modes, i.e. modes that mainly couple to the plane waves of the exterior. These would be expected at regions *off* any band, e.g. in the dark blue and cyan regions with labels 2 and 7. Returning to the prototype maps, these modes in fact have energy distributions that increase with the distance from the PhC surface. This leakage seems to be caused by a single E -field component at a time, while others can e.g. still exhibit the influence of a near band. This observation holds for all of the prototype maps.

$\Gamma - K, TM$

Moving on to the similar case of $\Gamma - K, TM$ (column 1 and figure 36), we observe a steep band of high fluorescence and field energy enhancement at a similar position. The clustering approach found the band as well, labeled as 6 (pinkish). Column 6 of the prototype map shows that this band localizes its energy at the center of the hole (slightly above the PhC in z -direction) but also at the flanks in the xz plane. It therefore potentially affects QDs relatively independently of whether they are gathered inside the hole or on the plateaus. Returning to the clustering, it is seen that a second, much broader band running from top left to bottom right is seen in the E_+ maps. The classification

maps reveal that the field distribution of this band undergoes a change when crossing the pinkish band, from label 7 (cyan) to label 1 (red). This band is basically not seen in the fluorescence enhancement, *but* there is a very bright region above 50° in the fluorescence that has not yet been commented. When keeping to the guide given above, it follows from step 2 that this feature might not be explained from the numerical data, because there is no field enhancement. However, if looking closely there is a kind of “transition boundary” in the E_+ map at almost exactly the outline of the bright fluorescence region. In the classification map, there is a feature at this location as well: a kind of “stroke” across the red, gray and dark blue regions. In fact, the prototype maps show that these clusters have similar energy distributions compared to the pinkish band, in this case caused by E_x rather than E_z . Although this still does not explain the fluorescence enhancement, it shows that there is in fact an effect at exactly this position which could potentially explain it. It is conceivable that this mode couples very effectively to the QDs and that the field enhancement in the real system is higher than suggested by the simulation.

$\Gamma - K, TE$

So far the TE cases are left to discuss, which both feature a more complicated band structure. In the $\Gamma - K$, TE case (column 2 and figure 37), there are two very clear bands that show anticrossing, a steeper band crossing the complete wavelength range from roughly 20° to 40° , and a shallower one coming from top left. The former is very clearly seen in the clustering by the gray region with label 8. From the prototype map it is observed that this band has a node along the x -direction and concentrates its energy at the flanks and the plateaus in y -direction. The energy distribution is therefore comparable to the one of the orange band in the $\Gamma - M$, TM case, which is clearly seen in the fluorescence as well. The shallower mentioned band undergoes a transition from the green cluster (label 3) to the red cluster (label 1) in the classification maps. For the green parts the energy is strongly localized at the flanks, while in the red case the E_y component couples to radiation modes. The energy is therefore less well confined to the surface in the red case, which is exactly seen in the fluorescence maps, where only at the location of a broad green region a fluorescence enhancement is seen.

To give a clear idea of the 3D energy density distribution for three selected modes, and also to show how well the clusters match the actual physical fields, figure 40 shows semi-artistic full-3D renderings. The images depict multiple periods of the photonic crystal as a grayish metal-like material, without showing a superspace material. The upper row shows a topview of the volume-rendered electric field energy density color-coded using a heat map, which is not comparable between the figures. The lower row shows a closer view and indicates a random distribution of QDs as bright small spheres, emitting white light with an intensity proportional to the field energy density at their specific positions. The QD distribution is the same for all three images. The

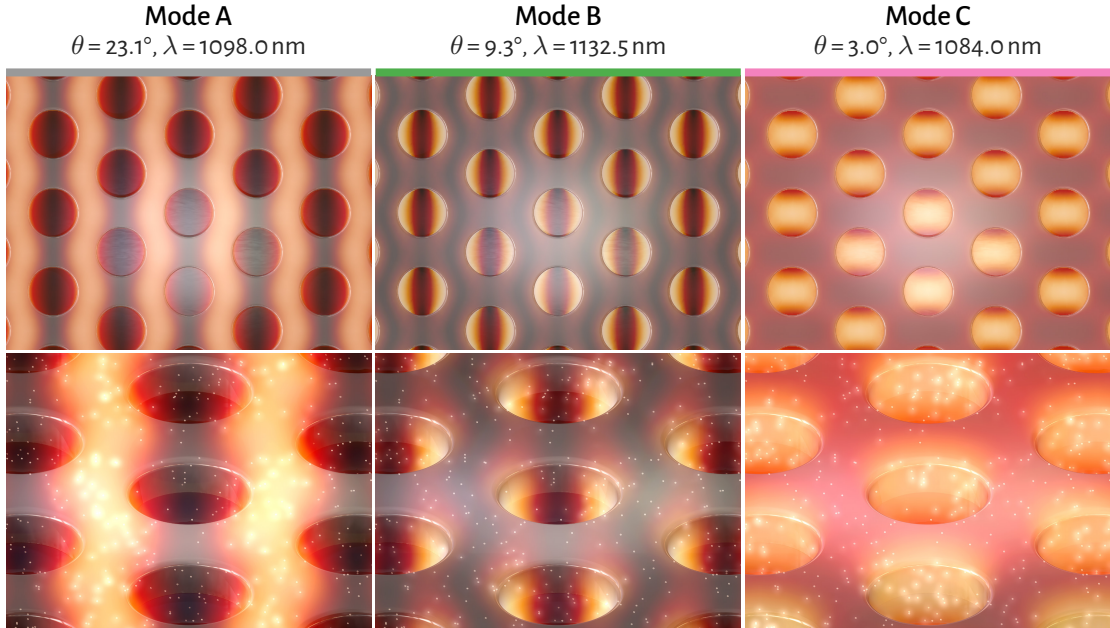


Figure 40: Full-3D volume renderings of selected modes for the $\Gamma - K$, TE case. Semi-artistic ray tracing images depicting multiple periods of the photonic crystal as a grayish metal-like material. The **upper row** shows a topview of the full-3D E -field energy density, color-coded using a heat map (not comparable between the figures; see also figure 1 on page 3). The **lower row** shows a closer view and indicates the same random distribution of quantum dots (bright small spheres), emitting white light with an intensity proportional to the field energy density at their specific positions. The **columns** relate to three different modes of the $\Gamma - K$, TE case, denoted as A, B and C. They correspond to clusters 8, 3 and 6 in figures 34 and 37, as indicated by the colored edges which match those of the previous figures (from left to right). Incident angle θ and wavelength λ for each mode are given in the headings. The figures use actual physical proportions.

columns relate to three different modes of the $\Gamma - K$, TE case, denoted as A, B and C. They correspond to clusters 8, 3 and 6 in figures 34 and 37, as indicated by the colored edges which match those of the previous figures. Incident angle θ and wavelength λ for each mode are given in the headings. Note that these images have an illustrative character, but can be very helpful to imagine the actual physical situation.

Modes A and B are the ones which have been discussed recently, and it is clearly seen that the former concentrates its energy at the *plateaus*, while the latter has high energy densities at the *flanks* of the holes. A third type is shown with mode C, which focusses the energy directly *inside the holes*. The illustrations in the lower row give a notion of how these modes activate different QDs, depending on their position. Only a small density of QDs is used for the images for purposes of visibility, and they are randomly distributed in a layer that fills the holes and extents 100 nm in z -direction. Mode A very efficiently excites QDs at the plateaus, just as expected, while modes B and C do the same at the flanks and inside the holes, respectively. Consequently, these renderings, which are complicated to generate and very demanding regarding computational

costs, completely confirm the results of the clustering approach.

$\Gamma - M, TE$

Finally, the $\Gamma - M, TE$ case (column 4 and figure 39) covers two bands that show anti-crossing at the long wavelength/steep angle end of the data window (top left). The lower band and most parts of the interaction zone are labeled as cluster 3 (green), while the upper band has label 7 (cyan). The green band has a node in the yz plane, while the energy in x -direction is strongly localized at the flanks. It is therefore likely to be seen in the fluorescence enhancement, when comparing to the previous results. However, a fluorescence enhancement for the green band is mainly seen in the interaction zone. This can be explained when considering the energy distribution of the cyan band: this band has almost the same distribution for E_y in the xz plane, but it does not have the node in the yz plane. In the interaction zone the two bands basically overlap, so that the E_y components add up and the node is partly erased. Therefore, a stronger effect in the fluorescence enhancement is expected, just as it is observed.

Interestingly, there is moreover a small effect at ≈ 1080 nm for large angles in the F_+ map. The clustering reveals another band with strong localization at the flanks: the orange region with label 4 (and the similar yellow one which couples more strongly to the radiation modes). It is likely that the measured effect is actually caused by this band, as it has a similar energy distribution as other bands which are clearly seen.

7.5.2 Summary and evaluation of the analysis method

The prior discussion showed a very consistent explanation of nearly all the effects observed in the fluorescence enhancement experiment. Even for the most complicated case of $\Gamma - M, TE$ a reasonable interpretation of the elongated bright spot (or rather two very close spots) has been found by a superposition of modes; and moreover light was shed on the very small effect in the bottom right corner. Similarly, it was possible to explain why the shallower band in the $\Gamma - K, TE$ case does not cause a strong fluorescence beyond the anticrossing point. And even for the bright spot at shallow angles in the $\Gamma - K, TM$ case a potential explanation was found.

When comparing these results to the ones that have been obtained by the first method based on a small number of selected field energy distributions in chapter 6, it is obvious that the clustering approach gave a much more coherent and detailed explication of the underlying physical phenomena. Of course it may have been possible to use even more points for the distribution analysis in the first method, and to thereby find similar conclusions. However, the clustering approach emphasizes the interesting parts automatically and systematically, – consequently revealing aspects that may have stayed unnoticed. The results further have a larger reliability as they are based on the complete set of field distributions, rather than on a partly random choice of points. The clustering technique seems to be applicable to even more complicated

cases, e.g. in windows with more bands where the first method would become rather complex (or even confusing). On the other hand, an aspect of the first method which could be taken into account in addition to the clustering is the Q-factor analysis, as it considers the additional quantity of the coupling quality between excitation source and leaky mode.

The presented technique composed of (i) the field energy enhancement maps and (ii) the field distribution clustering provides a versatile tool for the analysis and design of PhCs for applications based on excitations enhancement. For any known distribution of near-surface emitters that should be affected by leaky modes, optimum values for all relevant parameters can in principle be determined in the following way:

1. Define a wavelength range for the excitation of the emitters by considering their absorption properties, and possibly also their emission properties. The latter is relevant if an interaction of the emitted radiation with leaky modes is to be avoided (or even desired, if extraction enhancement effects should be utilized at the same time).
2. By using FEM simulations with a model that fits the actual final system, perform a parameter scan over the incident wavelengths, angles and polarizations and output/calculate the field energy enhancement E_+ and field values in 3D for clustering. This process results in the information as given in figure 34 (center and lower row) for the present case.
3. Choose the mode that causes the largest overlap of high field energy with the known emitter distribution from a spatial analysis of the prototypes (i.e. cluster centers) from the clustering, as e.g. in figure 36. This step will define the high-symmetry direction (i.e. incident angle ϕ in figure 9) and polarization, supposed there is a mode that is a clear optimum.
4. Determine the incident wavelength and angle θ by choosing the configuration with the largest field energy enhancement E_+ for the selected mode.

This process can moreover be repeated for possible geometrical parameters of the PhC, e.g. the lattice constant, slab thickness or hole radius. Alternatively, if the geometrical parameters should be varied extensively, the technique could be applied for an initial set of geometrical parameters to select a potential mode and to reduce the wavelength and angle window. Successively, only the field energy enhancement E_+ may be calculated in the scan over the possible geometrical parameters to determine the absolute maximum of the enhancement.

Numerous applications could benefit from these optimization abilities. In the field of biosensing, PhCs have become an important platform for e.g. label-free biosensing or for the enhancement of the output of photon emitting tags used in the life sciences and *in vitro* diagnostics. The recent article of Cunningham *et al.* [16] reviews the application areas and advances in this field. It shows that PhC enhanced biosensors are yet extremely relevant, even commercially and potentially on industrial scale: they

have been fabricated with costs that are compatible with single-use disposable applications. Exploiting leaky modes with large Q-factors enables for narrow bandwidth (< 1 nm) and extremely high sensitivities, e.g. for detection of disease biomarkers in serum with concentrations of ~ 1 pg ml⁻¹. The numerous applications that are described in the mentioned review article have in common that the PhC is designed for a very specific mode, i.e. a specific illumination condition and a determinable distribution of the molecules/cells/virus particles in question. This is where the technique presented here could be utilized for a *systematic* optimization in the design process, and hence to further increase the sensitivities of related sensors. Beyond biosensing, photochemical upconversion [108] is another application that could benefit from the discussed all-numerical design abilities. For this particular field, thoughts on possible applications will be covered in detail in the outlook part of chapter 8, so that they are omitted here.

Finally, with the analysis presented above the usage of machine learning for the mentioned purposes has just started. There certainly is a potential for the improvement of the efficiency of the method and also its applicability. From the large number of available clustering algorithms only two different ones have been used, namely *k*-means and GMM clustering. In consequence, a future task would be to systematically explore the different approaches and to find the algorithm which is best suited for the task at hand. As an example, there is a more powerful implementation of the GMM, commonly known as Bayesian GMM, which allows for an automatic determination of the number of clusters (see [64], chapter 9). Although this approach was tried, it did not result in reasonable numbers for the clusters. Accordingly, working out how to successfully apply this particular method or comparable methods could add another level of reliability and automatization.

8

Conclusion and Outlook

THE AIM OF THIS DISSERTATION has been to explore and develop numerical techniques for the analysis and design of photonic crystal (PhC) slabs for the interaction with light emitters in the vicinity of the surface. Of the processes which are capable of inducing an increase in optical transitions in such emitters, the excitation enhancement effect has been the focus of the investigations. Excitation enhancement occurs when leaky modes of the PhC increase the stimulated emission rate of emitters by locally enhanced field energy densities. Referring to the introduction, designing PhCs for applications that use this effect requires the identification of a mode with a large field energy density *and* a field distribution that optimally matches the arrangement of the emitters on the surface. Afterwards, the geometrical parameters of the PhC must be optimized for specific demands of the application, e.g. the illumination conditions, and for a maximum field energy enhancement. The challenges that arise are (1) the vast parameter spaces in the optimization process and (2) the huge amounts of field distribution data. To handle these challenges an accurate and efficient numerical modeling of the PhC-emitter system and proper techniques for the reduction and analysis of the data amounts are inevitable.

Chapter 2 showed that PhC slabs exhibit leaky modes that couple to the external light field, and that the properties of these modes are linked to the symmetry properties of the system. With this in mind, chapter 5 demonstrated experimentally that changing the symmetry of a specific PhC slab can affect the orthogonality of PhC modes, as revealed by certain anticrossing effects. A symmetrization of the PhC caused the anticrossing of two adjacent photonic bands to disappear. This effect was reproduced in finite element method (FEM) simulations and observed both in field energy enhancement maps and example field patterns. In a second experiment, chapter 6 showed that the fluorescence of quantum dots (QDs) is increased by excitation enhancement

when suitable leaky modes of the PhC overlap the absorption spectrum of the QDs. The angle- and wavelength-resolved measurements were explained using complementary field energy density calculations and an analysis of selected 3D field distributions.

Considering challenge (1) of the numbering given above, chapter 4 derived an accuracy-controlled and performance-optimized simulation setup for the efficient treatment of the specific PhC systems. To examine the spatial distribution of enhanced fields *systematically*, an extended analysis technique based on a classification of modes by machine learning was developed in chapter 7. The approach uses clustering techniques to classify the numerically obtained modes in view of their 3D field distributions. The reduction of the field distribution data to a minimum subset of representative modes accounts for challenge (2) given above. The representative modes, denoted as “prototypes”, virtually contain the complete information necessary to draw conclusions about the spatial aspects of excitation enhancement effects. A visual analysis technique denoted as “classification map” was introduced, which depicts the mode classification and the representation quality by the corresponding prototype at the same time. Chapter 7 applied the clustering approach to the anticrossing experiment of chapter 5 and the fluorescence enhancement experiment of chapter 6. For the first experiment, the symmetry dependence of anticrossing was verified from an extended perspective and the abilities of the clustering approach were showcased. For the fluorescence enhancement experiment, a much more systematic and complete explanation of the measured fluorescence enhancement was gained from the classification. Classification maps allowed for the explanation of virtually any aspect of the complex experimental fluorescence enhancement maps. Moreover, the prototypes were used to identify different types of modes that lead to a measurable increase in fluorescence.

A set of tools for the systematic design and analysis of PhC slabs for excitation enhancement of near-surface emitters has been attained. The effectiveness of these tools is based on the abilities of the FEM to accurately model complex dielectric structures including all relevant physical effects, and the selection of modes with specific spatial properties using a machine learning classification. This allows to optimize PhCs for applications utilizing excitation enhancement. It is conceivable that the machine learning-based classification of modes becomes a valuable technique in the analysis of PhCs, e.g. as an alternative to traditional band structure computations.

Limitations of the clustering approach may arise in the case of a high density of photonic bands and if complex interactions are present. Another aspect is the comparably high computational effort and the challenge of finding the optimum input parameters for the clustering algorithm. However, these limitations appear manageable when considering the large number of available clustering algorithms and related techniques which are yet to be explored. More advanced algorithms, such as the Bayesian Gaussian mixture model clustering ([64], chapter 9), potentially can expand the applicability

and increase the automatization of the classification of PhC modes.

BESIDES THE IMPROVEMENT OF THE METHODS, there are multiple conceivable areas of activity for future research which are apparent from the content of this thesis. The presented fluorescence enhancement experiment could be repeated with an optimized PhC design. This would necessitate achieving a well-defined QD distribution, e.g. a monolayer, and optimizing the system for a maximum field energy enhancement *and* a maximum overlap of the field and the QDs. Instead of mapping the fluorescence enhancement against the illumination conditions, the measurement could use a specific illumination setup and a laser source that matches the bandwidth (i.e. Q-factor) of the related leaky mode. In a second step, the PhC could be designed to exhibit leaky modes in the wavelength range of the QD emission as well. This would allow the exploitation of extraction *and* excitation enhancement effects at the same time, as already demonstrated by Ganesh *et al.* [30].

From the applications that already have been reported in literature, the developed techniques could be regarded as the missing piece of the puzzle, at least for PhCs which are periodic in two dimensions. Let us reconsider the experiments of Ganesh *et al.* [30], who showed PhC enhanced fluorescence of QDs, and Block *et al.* [17], who showed the same for DNA molecules. Both report a massive increase in fluorescence which is partly caused by excitation enhancement, but *without* a true optimization of the PhC in view of the mode profiles and field energy enhancement factors. It can be assumed that an optimization would further increase the observed effects. The relevance of PhC slabs in the field of biosensing has recently been reviewed by Cunningham *et al.* [16], who showed that they are not only widely used, but may become a key technology for the study of the behavior of stem cells, cancer cells, and biofilms. Specifically, PhC enhanced fluorescence is relevant for high sensitivity cancer biomarker detection or for label-free high-resolution imaging of cells and individual nanoparticles. By using enhanced excitation and extraction at the same time, increases in fluorescence as high as $7500\times$ have been reported [109, 110]. These systems could certainly benefit from the presented design techniques as well.

Another point of interest is the exploration of different or more advanced geometries of the actual PhC slab. Figure 41 shows an illustration of the hexagonal lattice on the left, which has been used for all the investigations. One possibility is to introduce a periodic arrangement of point defects to the lattice, usually denoted as coupled cavity arrays [6, 111], as suggested in the center of figure 41. These cavities can have huge local densities of optical states and can exhibit so-called strong coupling to nearby emitters [62, 112]. This increases the interest in how these systems could be used for similar effects as the ones which have been investigated so far. As a second kind of possible variation of the geometry, other lattice types may be explored, such as quasiperiodic

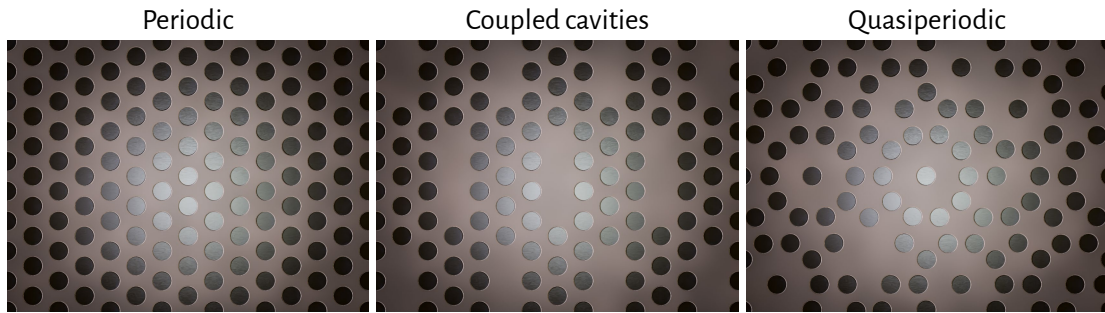


Figure 41: Examples for nanohole arrangements in silicon photonic crystal slabs. The illustrations depict a periodic hexagonal lattice (left), an array of coupled L3 cavities (center), and a 10-fold quasiperiodic arrangement (right).

arrangements as illustrated at the right of figure 41 [113–115]. The latter, which more generally belongs to the class of deterministic aperiodic nanostructures, exhibit intermediate properties between periodic and random arrangements. This potentially allows to tailor PhC slabs for broadband excitation enhancement, as broadband effects are a main characteristic of random arrangements. It must however be noted that the treatment of aperiodic structures is computationally more elaborate, due to the lack of a unit cell.

Finally, application fields should be explored which have different design targets or which introduce additional challenges. Besides applications such as surface-enhanced Raman spectroscopy [116], upconversion seems to be a candidate that could benefit from the increased near-fields and also from extraction enhancement effects. Recent publications by Wu *et al.* [117, 118] use a monolayer of lead sulfide (PbS) QDs on glass to give rise to upconversion in an adjacent layer of doped rubrene. The excitons of the QDs are transferred to the rubrene molecules in a non-radiative process and lead to triplet–triplet annihilation (TTA). The latter process causes the incident light to be “converted” to shorter wavelengths, i.e. raised to a higher energy. The efficiency of this process depends on the amount of light which is absorbed by the QD layer, and in the experiment presented in [117], the absorption was as low as 0.1%. However, increasing the thickness of the QD layer is contradictory to the additional demand of a low diffusion length of the excited states of the QDs. Here is where PhC enhanced near-fields could contribute by effectively increasing the absorption rate of the QDs. This is moreover a crucial aspect, as the upconversion efficiency scales approximately as the square of the excitation rate. A sketch of the conceivable system is depicted in figure 42, which shows a slice through the hexagonal PhC as it was considered in the experiments in this thesis. The PhC surface is covered with a monolayer of QDs (greenish) and an adjacent layer of rubrene (black). The transfer of excited states from the QDs to the rubrene and the subsequent TTA process is indicated in the zoomed in circle at the right of the figure. The emission at a wavelength smaller than the excitation wavelength, indicated

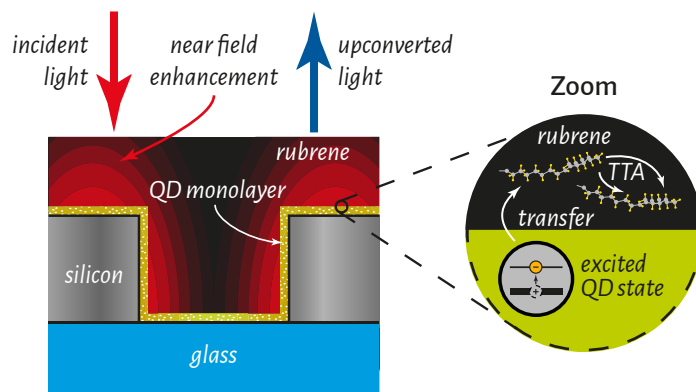


Figure 42: Sketch of a possible photonic crystal enhanced upconversion system. A silicon photonic crystal (gray) on glass (cyan) is covered with a monolayer of quantum dots (QD, greenish with white dots) and rubrene. Incident light (red arrow) excites a leaky mode of the photonic crystal, leading to near-field energy enhancement. The field excites states in the QDs which are transferred to rubrene molecules (zoomed in circle at right). The light is upconverted to shorter wavelengths by triplet–triplet annihilation (TTA), as indicated by the blue arrow.

by a blue arrow in the figure, must be taken into account in the design of the PhC, as challenges may arise due to reabsorption in the PhC. However, a proper design could possibly even improve the extraction efficiency of the upconverted light using leaky modes in the related wavelength range.

In the end, upconversion is e.g. interesting for solar energy harvesting by increasing the fraction of the solar spectrum that contributes to the photovoltaic effect [108, 119]. In this and comparable cases, another challenge would be to design the system for a maximum field energy enhancement in a very broad wavelength range. As it was mentioned above, such broadband field energy enhancement effects may be generated using quasiperiodic arrangements in the PhC geometry. Finally, the design process of complex systems, such as for the upconversion application, may even depend on a systematic and highly automatized assessment of PhC mode properties. The developed machine learning-based classification of modes, together with the powerful FEM, appear to be well suited for this task.

Own Contributions

Peer-reviewed articles

- Barth, C.**, Burger, S. & Becker, C. *Symmetry-dependency of anticrossing phenomena in slab-type photonic crystals*. *Optics Express* **24**, 10931 (May 2016).
- Barth, C.**, Roder, S., Brodoceanu, D., Kraus, T., Hammerschmidt, M., Burger, S. & Becker, C. *Increased fluorescence of PbS quantum dots in photonic crystals by excitation enhancement*. *Applied Physics Letters* **111**, 031111 (July 2017).
- Barth, C.**, Herrmann, S., Hammerschmidt, M. & Becker, C. *Numerical characterization of symmetry properties for photonic crystals with hexagonal lattice*. *Proceedings of SPIE* **9885**, 988506 (2016).
- Hammerschmidt, M., **Barth, C.**, Pomplun, J., Burger, S., Becker, C. & Schmidt, F. *Reconstruction of photonic crystal geometries using a reduced basis method for nonlinear outputs*. *Proceedings of SPIE* **9756**, 97561R (2016).
- Jäger, K., **Barth, C.**, Hammerschmidt, M., Herrmann, S., Burger, S., Schmidt, F. & Becker, C. *Simulations of sinusoidal nanotextures for coupling light into c-Si thin-film solar cells*. *Optics Express* **24**, A569 (Mar. 2016).
- Jäger, K., Köppel, G., **Barth, C.**, Hammerschmidt, M., Herrmann, S., Burger, S., Schmidt, F. & Becker, C. *Sinusoidal Gratings for Optimized Light Management in c-Si Thin-Film Solar Cells*. *Proceedings of SPIE* **9898**, 989807 (2016).
- Jäger, K., **Barth, C.**, Hammerschmidt, M., Herrmann, S., Burger, S., Schmidt, F. & Becker, C. *Sinusoidal Nanotextures for Coupling Light into c-Si Thin-Film Solar Cells*. in *Light, Energy and the Environment 2015* **2950** (Optical Society of America, Washington, D.C., 2015), PTu4B.3.

Contributed talks

- Barth, C.**, Roder, S., Brodoceanu, D., Kraus, T., Burger, S., Hammerschmidt, M., Schmidt, F. & Becker, C. *Photonic Crystal Enhanced Fluorescence of PbS Quantum Dots: Experiments, Light Scattering Simulations and Band Structure Computations*. (presented by K. Jäger) SPIE Photonics Europe, Photonic Crystal Materials and Devices XII, Brussels, Belgium, 2016.

Barth, C., Hammerschmidt, M., Jäger, K., Burger, S. & Becker, C. *Near field enhancement in large-area Si-photonic crystals*. Matheon Workshop, 8th Annual Meeting Photonic Devices, Berlin, Germany, 2014.

Poster presentations

Barth, C., Jäger, K., Burger, S., Hammerschmidt, Martin Schmidt, F. & Becker, C. *Design of Photonic Crystals with Near-Surface Field Enhancement*. Optical Society of America (OSA) Energy and the Environment Congress, Suzhou, China, 2015.

Barth, C., Burger, S., Hammerschmidt, M. & Becker, C. *Near field enhancement in large-area Si-photonic crystals*. European Optical Society Annual Meeting (EOSAM), Berlin, Germany, 2014.

Barth, C., Adler, M., Probst, J., Schoengen, M., Löchel, B., Wolters, J. & Benson, O. *Design and Optimization and Fabrication of Photonic Crystal Structures for Single Photon Applications*. Deutsche Physikalische Gesellschaft (DPG) Tagung, Regensburg, Germany, 2013.

Own master and bachelor theses and related publications

Barth, C., Wolters, J., Schell, A. W., Probst, J., Schoengen, M., Löchel, B., Kowarik, S. & Benson, O. *Miniaturized Bragg-grating couplers for SiN-photonic crystal slabs*. *Optics Express* **23**, 9803 (2015).

Barth, C. *Investigation of Photonic Crystal Components for Integrated Devices in the Visible*. Master Thesis (Humboldt-Universität zu Berlin, 2014).

Barth, C. *Design und Optimierung von Wellenleitern und Gitterkopplern für Photonische Kristall-Strukturen*. Bachelor Thesis (Humboldt-Universität zu Berlin, 2011).

Supervised master theses

Roder, S. *Messung der Fluoreszenzerhöhung von Quantenpunkten durch Wechselwirkung mit photonischen Kristallen*. Master Thesis (Technische Universität Berlin, 2016).

References

1. Joannopoulos, J. D., Johnson, S. G., Winn, J. N. & Meade, R. D. *Photonic crystals: molding the flow of light* 2nd editio (Princeton University Press, 2008).
2. Sakoda, K. *Optical Properties of Photonic Crystals*, 258 (Springer-Verlag, Berlin/Heidelberg, 2005).
3. Kuramochi, E., Notomi, M., Mitsugi, S., Shinya, A., Tanabe, T. & Watanabe, T. *Ultrahigh-Q photonic crystal nanocavities realized by the local width modulation of a line defect*. *Applied Physics Letters* **88**, 041112 (2006).
4. Johnson, S. G., Villeneuve, P. R., Fan, S. & Joannopoulos, J. D. *Linear waveguides in photonic-crystal slabs*. *Phys. Rev. B* **62**, 8212–8222 (Sept. 2000).
5. Johnson, S. G., Fan, S., Villeneuve, P., Joannopoulos, J. D. & Kolodziejski, L. *Guided modes in photonic crystal slabs*. *Physical Review B* **60**, 5751–5758 (Aug. 1999).
6. Altug, H., Englund, D. & Vučković, J. *Ultrafast photonic crystal nanocavity laser*. *Nature Physics* **2**, 484–488 (2006).
7. Hartmann, M. J., Brandão, F. G. S. L. & Plenio, M. B. *Strongly interacting polaritons in coupled arrays of cavities*. *Nature Physics* **2**, 849–855 (2006).
8. Rosenblatt, D., Sharon, A. & Friesem, A. *Resonant grating waveguide structures*. *IEEE Journal of Quantum Electronics* **33**, 2038–2059 (1997).
9. Astratov, V. N., Whittaker, D. M., Culshaw, I. S., Stevenson, R. M., Skolnick, M. S., Krauss, T. F. & De La Rue, R. M. *Photonic band-structure effects in the reflectivity of periodically patterned waveguides*. *Physical Review B* **60**, R16255–R16258 (Dec. 1999).
10. Astratov, V. N., Culshaw, I. S., Stevenson, R. M., Whittaker, D. M., Skolnick, M. S., Krauss, T. F. & De La Rue, R. M. *Resonant coupling of near-infrared radiation to photonic band structure waveguides*. *Journal of Lightwave Technology* **17**, 2050–2057 (1999).
11. Erchak, A. A., Ripin, D. J., Fan, S., Rakich, P., Joannopoulos, J. D., Ippen, E. P., Petrich, G. S. & Kolodziejski, L. A. *Enhanced coupling to vertical radiation using a two-dimensional photonic crystal in a semiconductor light-emitting diode*. *Applied Physics Letters* **78**, 563–565 (Jan. 2001).
12. Ochiai, T. & Sakoda, K. *Dispersion relation and optical transmittance of a hexagonal photonic crystal slab*. *Physical Review B* **63**, 125107 (Mar. 2001).

13. Chutinan, A. & John, S. *Light trapping and absorption optimization in certain thin-film photonic crystal architectures*. *Physical Review A* **78**, 023825 (Aug. 2008).
14. Fan, S., Villeneuve, P. R., Joannopoulos, J. D. & Schubert, E. F. *High Extraction Efficiency of Spontaneous Emission from Slabs of Photonic Crystals*. *Physical Review Letters* **78**, 3294–3297 (Apr. 1997).
15. Wiesmann, C., Bergenek, K., Linder, N. & Schwarz, U. *Photonic crystal LEDs - designing light extraction*. *Laser & Photonics Review* **3**, 262–286 (Apr. 2009).
16. Cunningham, B. T., Zhang, M., Zhuo, Y., Kwon, L. & Race, C. *Recent Advances in Biosensing With Photonic Crystal Surfaces: A Review*. *IEEE Sensors Journal* **16**, 3349–3366 (May 2016).
17. Block, I. D., Mathias, P. C., Ganesh, N., Jones, S. I., Dorvel, B. R., Chaudhery, V., Vodkin, L. O., Bashir, R. & Cunningham, B. T. *A detection instrument for enhanced-fluorescence and label-free imaging on photonic crystal surfaces*. *Optics Express* **17**, 13222 (July 2009).
18. Ganesh, N., Mathias, P. C., Zhang, W. & Cunningham, B. T. *Distance dependence of fluorescence enhancement from photonic crystal surfaces*. *Journal of Applied Physics* **103**, 083104 (2008).
19. Threm, D., Nazirizadeh, Y. & Gerken, M. *Photonic crystal biosensors towards on-chip integration*. *Journal of Biophotonics* **5**, 601–616 (2012).
20. *Persistence of Vision Raytracer*. Williamstown, Victoria (Australia), 2013.
21. Boroditsky, M., Vrijen, R., Krauss, T., Coccioli, R., Bhat, R. & Yablonovitch, E. *Spontaneous emission extraction and Purcell enhancement from thin-film 2-D photonic crystals*. *Journal of Lightwave Technology* **17**, 2096–2112 (1999).
22. Ganesh, N., Block, I. D., Mathias, P. C., Zhang, W., Chow, E., Malyarchuk, V. & Cunningham, B. T. *Leaky-mode assisted fluorescence extraction: application to fluorescence enhancement biosensors*. *Optics express* **16**, 21626–21640 (2008).
23. Ondič, L., Babchenko, O., Varga, M., Kromka, A., Čtyroký, J. & Pelant, I. *Diamond photonic crystal slab: Leaky modes and modified photoluminescence emission of surface-deposited quantum dots*. *Scientific Reports* **2**, 914 (Dec. 2012).
24. Ondič, L., Dohnalová, K., Ledinský, M., Kromka, A., Babchenko, O. & Rezek, B. *Effective Extraction of Photoluminescence from a Diamond Layer with a Photonic Crystal*. *ACS Nano* **5**, 346–350 (Jan. 2011).
25. Ondič, L., Kůsová, K., Cibulka, O., Pelant, I., Dohnalová, K., Rezek, B., Babchenko, O., Kromka, A. & Ganesh, N. *Enhanced photoluminescence extraction efficiency from a diamond photonic crystal via leaky modes*. *New Journal of Physics* **13**, 063005 (June 2011).

26. Ondič, L., Varga, M., Hruška, K., Kromka, A., Herynková, K., Hönerlage, B. & Pelant, I. *Two-dimensional photonic crystal slab with embedded silicon nanocrystals: Efficient photoluminescence extraction*. *Applied Physics Letters* **102**, 251111 (2013).
27. Becker, C., Wyss, P., Eisenhauer, D., Probst, J., Preidel, V., Hammerschmidt, M. & Burger, S. *5 × 5 cm² silicon photonic crystal slabs on glass and plastic foil exhibiting broadband absorption and high-intensity near-fields*. *Scientific Reports* **4**, 5886 (July 2014).
28. Mathias, P. C., Ganesh, N. & Cunningham, B. T. *Application of Photonic Crystal Enhanced Fluorescence to a Cytokine Immunoassay*. *Analytical Chemistry* **80**, 9013–9020 (Dec. 2008).
29. Ryu, H. Y., Lee, Y. H., Sellin, R. L. & Bimberg, D. *Over 30-fold enhancement of light extraction from free-standing photonic crystal slabs with InGaAs quantum dots at low temperature*. *Applied Physics Letters* **79**, 3573 (2001).
30. Ganesh, N., Zhang, W., Mathias, P. C., Chow, E., Soares, J. a. N. T., Malyarchuk, V., Smith, A. D. & Cunningham, B. T. *Enhanced fluorescence emission from quantum dots on a photonic crystal surface*. *Nature Nanotechnology* **2**, 515–520 (Aug. 2007).
31. Adachi, M. M., Labelle, A. J., Thon, S. M., Lan, X., Hoogland, S. & Sargent, E. H. *Broadband solar absorption enhancement via periodic nanostructuring of electrodes*. *Scientific Reports* **3**, 2928 (Oct. 2013).
32. Kim, S., Kim, J. K., Gao, J., Song, J. H., An, H. J., You, T.-s., Lee, T.-S., Jeong, J.-R., Lee, E.-S., Jeong, J.-H., Beard, M. C. & Jeong, S. *Lead Sulfide Nanocrystal Quantum Dot Solar Cells with Trenched ZnO Fabricated via Nanoimprinting*. *ACS Applied Materials & Interfaces* **5**, 3803–3808 (May 2013).
33. Su, L. T., Karuturi, S. K., Luo, J., Liu, L., Liu, X., Guo, J., Sum, T. C., Deng, R., Fan, H. J., Liu, X. & Tok, A. I. Y. *Photon Upconversion in Hetero-nanostructured Photoanodes for Enhanced Near-Infrared Light Harvesting*. *Advanced Materials* **25**, 1603–1607 (Mar. 2013).
34. Zhang, F., Deng, Y., Shi, Y., Zhang, R. & Zhao, D. *Photoluminescence modification in upconversion rare-earth fluoride nanocrystal array constructed photonic crystals*. *Journal of Materials Chemistry* **20**, 3895 (2010).
35. Hofmann, C. L. M., Herter, B., Fischer, S., Gutmann, J. & Goldschmidt, J. C. *Upconversion in a Bragg structure: photonic effects of a modified local density of states and irradiance on luminescence and upconversion quantum yield*. *Optics Express* **24**, 14895 (June 2016).
36. Smajic, J., Hafner, C. & Erni, D. *Optimization of photonic crystal structures*. *Journal of the Optical Society of America A* **21**, 2223 (Nov. 2004).

37. Hakansson, A., Sanchez-Deh, J. & Sanchis, L. *Inverse design of photonic crystal devices*. *IEEE Journal on Selected Areas in Communications* **23**, 1365–1371 (July 2005).
38. Lu, J. *Nanophotonic Computational Design*. Dissertation (Stanford University, 2013).
39. Lu, J. & Vučković, J. *Nanophotonic computational design*. *Optics Express* **21**, 13351 (2013).
40. Piggott, A. Y., Lu, J., Lagoudakis, K. G., Petykiewicz, J., Babinec, T. M. & Vučković, J. *Inverse design and demonstration of a compact and broadband on-chip wavelength demultiplexer*. *Nature Photonics* **9**, 374–377 (2015).
41. Barth, C., Burger, S. & Becker, C. *Symmetry-dependency of anticrossing phenomena in slab-type photonic crystals*. *Optics Express* **24**, 10931 (May 2016).
42. Barth, C., Roder, S., Brodoceanu, D., Kraus, T., Hammerschmidt, M., Burger, S. & Becker, C. *Increased fluorescence of PbS quantum dots in photonic crystals by excitation enhancement*. *Applied Physics Letters* **111**, 031111 (July 2017).
43. Jackson, J. D. *Classical Electrodynamics* 3rd editio (John Wiley & Sons, New York, Sept. 1999).
44. Lavrinenko, A. V., Lægsgaard, J., Gregersen, N., Schmidt, F. & Søndergaard, T. *Numerical Methods in Photonics* (ed Wyant, J. C.) 362 (CRC Press, Boca Raton, FL, 2015).
45. Pomplun, J., Burger, S., Zschiedrich, L. & Schmidt, F. *Adaptive finite element method for simulation of optical nano structures*. *physica status solidi b* **244**, 3419–3434 (Oct. 2007).
46. Zschiedrich, L. *Transparent Boundary Conditions for Maxwell's Equations: Numerical Concepts beyond the PML Method*. PhD Thesis (Freie Universität at Berlin, 2009).
47. Hammerschmidt, M. *Optical simulation of complex nanostructured solar cells with a reduced basis method*. PhD Thesis (Freie Universität Berlin, 2015).
48. Nolting, W. *Grundkurs Theoretische Physik 3*, 156 (Springer Berlin Heidelberg, Berlin, Heidelberg, 2013).
49. Rayleigh, L. XVII. *On the maintenance of vibrations by forces of double frequency, and on the propagation of waves through a medium endowed with a periodic structure*. *Philosophical Magazine Series 5* **24**, 145–159 (Aug. 1887).
50. Yablonovitch, E. *Inhibited Spontaneous Emission in Solid-State Physics and Electronics*. *Physical Review Letters* **58**, 2059–2062 (May 1987).
51. John, S. *Strong localization of photons in certain disordered dielectric superlattices*. *Physical Review Letters* **58**, 2486–2489 (1987).

52. Ashcroft, N. W. & Mermin, N. D. *Solid State Physics* College (Harcourt College Publishers, 1976).
53. Barth, C., Herrmann, S., Hammerschmidt, M. & Becker, C. *Numerical characterization of symmetry properties for photonic crystals with hexagonal lattice. Proceedings of SPIE* **9885**, 988506 (2016).
54. Cornwell, J. F. *Group theory and electronic energy bands in solids* (John Wiley International Publishers, New York, 1969).
55. Inui, T., Tanabe, Y. & Onodera, Y. *Group theory and its applications in physics* (Springer, Berlin, 1990).
56. Sakurai, J. J. & Napolitano, J. *Modern Quantum Mechanics* 2nd editio (Addison-Wesley, San Francisco, 2011).
57. Courant, R. & Hilbert, D. *Methods of Mathematical Physics, Volume 1*, 575 (Wiley, New York, 1989).
58. Sakoda, K. *Symmetry, degeneracy, and uncoupled modes in two-dimensional photonic lattices. Physical Review B* **52**, 7982–7986 (Sept. 1995).
59. Johnson, S. G. & Joannopoulos, J. D. *Block-iterative frequency-domain methods for Maxwell's equations in a planewave basis. Opt. Express* **8**, 363–376 (2001).
60. Hu, J. & Menyuk, C. R. *Understanding leaky modes: slab waveguide revisited. Advances in Optics and Photonics* **1**, 58 (Jan. 2009).
61. Svelto, O. *Principles of Lasers* 5th editio, 1–620 (Springer US, Boston, MA, 2010).
62. Purcell, E. M. *Spontaneous emission probabilities at radio frequencies. Physical Review* **69**, 681 (1946).
63. Hastie, T., Tibshirani, R. & Friedman, J. *The Elements of Statistical Learning* 2nd editio. *Springer Series in Statistics* **2**, 83–85 (Springer New York, New York, NY, 2009).
64. Bishop, C. M. *Pattern Recognition and Machine Learning* (Springer US, 2006).
65. Conway, D. & White, J. M. *Machine Learning for Hackers* (ed Steele, J.) 1–303 (O'Reilly, Sebastopol, CA, 2012).
66. Fisher, R. A. *The use of multiple measurements in taxonomic problems. Annals of Eugenics* **7**, 179–188 (Sept. 1936).
67. Pedregosa, F., Varoquaux, G., Gramfort, A., Michel, V., Thirion, B., Grisel, O., Blondel, M., Louppe, G., Prettenhofer, P., Weiss, R., Dubourg, V., Vanderplas, J., Passos, A., Cournapeau, D., Brucher, M., Perrot, M. & Duchesnay, É. *Scikit-learn: Machine Learning in Python.* **12**, 2825–2830 (2012).

68. Arthur, D. & Vassilvitskii, S. *K-Means++: the Advantages of Careful Seeding*. *Proceedings of the eighteenth annual ACM-SIAM symposium on Discrete algorithms* **8**, 1027–1025 (2007).
69. Dempster, A. P., Laird, N. M. & Rubin, D. B. *Maximum Likelihood from Incomplete Data via the EM Algorithm*. *Journal of the Royal Statistical Society Series B (Methodological)* **39**, 1–38 (1977).
70. McLachlan, G. J. & Krishnan, T. *Wiley Series in Probability and Statistics* 2nd editio (John Wiley & Sons, Inc., Hoboken, NJ, USA, 1997).
71. Rousseeuw, P. J. *Silhouettes: A graphical aid to the interpretation and validation of cluster analysis*. *Journal of Computational and Applied Mathematics* **20**, 53–65 (1987).
72. Farjadpour, a., Roundy, D., Rodriguez, A., Ibanescu, M., Bermel, P., Joannopoulos, J. D., Johnson, S. G. & Burr, G. W. *Improving accuracy by subpixel smoothing in the finite-difference time domain*. *Optics Letters* **31**, 2972 (2006).
73. Bischoff, J. *Improved diffraction computation with a hybrid C-RCWA-method*. *Proceedings of SPIE* **7272**, 72723Y (2009).
74. Demkowicz, L. *Computing with hp-ADAPTIVE FINITE ELEMENTS - Volume 1 - one and two dimensional elliptic and maxwell problems* (CRC Press, 2006).
75. Gutsche, P. *Convergence Study of the Fourier Modal Method for Nano-optical Scattering Problems in Comparison with the Finite Element Method*. Master Thesis (Eberhard Karls Universität Tübingen, 2014).
76. Monk, P. *Finite element methods for Maxwell's equations* (Oxford University Press, 2003).
77. Burger, S., Gutsche, P., Hammerschmidt, M., Herrmann, S., Pomplun, J., Schmidt, F., Wohlfeil, B. & Zschiedrich, L. *Hp-finite-elements for simulating electromagnetic fields in optical devices with rough textures*. in *Proceedings of SPIE* (eds Smith, D. G., Wyrowski, F. & Erdmann, A.) (Sept. 2015), 96300S. arXiv: 1510.02607.
78. Berenger, J.-P. *A perfectly matched layer for the absorption of electromagnetic waves*. *Journal of Computational Physics* **114**, 185–200 (Oct. 1994).
79. Zschiedrich, L., Burger, S., Kettner, B. & Schmidt, F. *Advanced finite element method for nano-resonators*. in *Proc. SPIE, Physics and Simulation of Optoelectronic Devices XIV* (eds Osinski, M., Henneberger, F. & Arakawa, Y.) (Feb. 2006), 611515. arXiv:0601025 [physics].
80. Monk, P. *On the p- and hp-extension of Nédélec's curl-conforming elements*. *Journal of Computational and Applied Mathematics* **53**, 117–137 (July 1994).

81. Cangellaris, A. *Frequency-domain finite element methods for electromagnetic field simulation: fundamentals, state of the art, and applications to EMI/EMC analysis*. in *Proceedings of Symposium on Electromagnetic Compatibility* **59** (IEEE, July 1985), 107–116.
82. Bayliss, A., Goldstein, C. & Turkel, E. *On accuracy conditions for the numerical computation of waves*. *Journal of Computational Physics* **59**, 396–404 (July 1985).
83. Shannon, C. *Communication in the Presence of Noise*. *Proceedings of the IRE* **37**, 10–21 (Jan. 1949).
84. Delaunay, B. *Sur la sphère vide. A la mémoire de Georges Voronoï*. *Bulletin of Academy of Sciences of the USSR* **7**, 793–800 (1934).
85. Foley, J. D., van Dam, A., Feiner, S. K. & Hughes, J. F. *Computer Graphics Principles and Practice* 2nd editio, 1–1175 (Addison-Wesley, Boston, 2010).
86. Aspnes, D. E. *Spectroscopic Analysis of the Interface Between Si and Its Thermally Grown Oxide*. *Journal of The Electrochemical Society* **127**, 1359 (1980).
87. Palik, E. D. *Handbook of Optical Constants of Solids* (Elsevier, June 1985).
88. Fritsch, F. N. & Carlson, R. E. *Monotone Piecewise Cubic Interpolation*. *SIAM Journal on Numerical Analysis* **17**, 238–246 (Apr. 1980).
89. Material. *Corning* × *EAGLE XG™ data sheet*. 2013.
90. Material. *Schott Optical Glass data sheets*. 2017.
91. Alivisatos, A. P. *Semiconductor Clusters, Nanocrystals, and Quantum Dots*. *Science* **271**, 933–937 (Feb. 1996).
92. Novotny, L. & Hecht, B. in *Principles of nano-optics* 2nd, 282–312 (Cambridge University Press, 2012).
93. Kraus, T., Malaquin, L., Schmid, H., Riess, W., Spencer, N. D. & Wolf, H. *Nanoparticle printing with single-particle resolution*. *Nature nanotechnology* **2**, 570–6 (2007).
94. Material. *Sopra material database*. 2017.
95. Craig, B. M. *REFRACTIVE INDICES OF SOME SATURATED AND MONOETHENOID FATTY ACIDS AND METHYL ESTERS*. *Canadian Journal of Chemistry* **31**, 499–504 (May 1953).
96. Van Nijnatten, P. *An automated directional reflectance/transmittance analyser for coating analysis*. *Thin Solid Films* **442**, 74–79 (Oct. 2003).
97. Jäger, K., Isabella, O., van Swaaij, R. A. C. M. M. & Zeman, M. *Angular resolved scattering measurements of nano-textured substrates in a broad wavelength range*. *Measurement Science and Technology* **22**, 105601 (Oct. 2011).

98. Roder, S. *Messung der Fluoreszenzerhöhung von Quantenpunkten durch Wechselwirkung mit photonischen Kristallen*. Master Thesis (Technische Universität Berlin, 2016).
99. Senn, T., Bischoff, J., Nüsse, N., Schoengen, M. & Löchel, B. *Fabrication of photonic crystals for applications in the visible range by Nanoimprint Lithography*. *Photonics and Nanostructures - Fundamentals and Applications* **9**, 248–254 (July 2011).
100. Merkel, J., Sontheimer, T., Rech, B. & Becker, C. *Directional growth and crystallization of silicon thin films prepared by electron-beam evaporation on oblique and textured surfaces*. *Journal of Crystal Growth* **367**, 126–130 (Mar. 2013).
101. Pardo, D., Demkowicz, L., Torres-Verdín, C. & Paszynski, M. *A self-adaptive goal-oriented hp-finite element method with electromagnetic applications. Part II: Electrodynamics*. *Computer Methods in Applied Mechanics and Engineering* **196**, 3585–3597 (2007).
102. Becker, R. & Rannacher, R. *An optimal control approach to a posteriori error estimation in finite element methods*. *Acta Numerica* **10** (2001).
103. Zschiedrich, L., Burger, S., Pomplun, J. & Schmidt, F. *Goal Oriented Adaptive Finite Element Method for the Precise Simulation of Optical Components*. **6475**, 9 (2007).
104. Bohren, C. F. & Huffman, D. R. *Absorption and Scattering of Light by Small Particles* (eds Bohren, C. F. & Huffman, D. R.) 530 (Wiley-VCH Verlag GmbH, Weinheim, Germany, Apr. 1998).
105. Miroschnichenko, A. E., Flach, S. & Kivshar, Y. S. *Fano resonances in nanoscale structures*. *Reviews of Modern Physics* **82**, 2257–2298 (2010).
106. Baba, T. *Slow light in photonic crystals*. *Nature Photonics* **2**, 465–473 (Aug. 2008).
107. Hammerschmidt, M., Barth, C., Pomplun, J., Burger, S., Becker, C. & Schmidt, F. *Reconstruction of photonic crystal geometries using a reduced basis method for nonlinear outputs*. *Proceedings of SPIE* **9756**, 97561R (2016).
108. Schulze, T. F., Czolk, J., Cheng, Y.-y., Fückel, B., MacQueen, R. W., Khoury, T., Crossley, M. J., Stannowski, B., Lips, K., Lemmer, U., Colsmann, A. & Schmidt, T. W. *Efficiency Enhancement of Organic and Thin-Film Silicon Solar Cells with Photochemical Upconversion*. *The Journal of Physical Chemistry C* **116**, 22794–22801 (Nov. 2012).
109. Pokhriyal, A., Lu, M., Schulz, S., Huang, C. S. & Cunningham, B. T. *Multi-color fluorescence enhancement from a photonics crystal surface*. in *2010 IEEE Sensors* (IEEE, Nov. 2010), 2287–2290.

110. Pokhriyal, A., Lu, M., Ge, C. & Cunningham, B. T. *Coupled external cavity photonic crystal enhanced fluorescence*. *Journal of Biophotonics* **7**, 332–340 (May 2014).
111. Altug, H. & Vučković, J. *Two-dimensional coupled photonic crystal resonator arrays*. *Applied Physics Letters* **84**, 161 (2004).
112. Hennessy, K., Badolato, a., Winger, M., Gerace, D., Atatüre, M., Gulde, S., Fält, S., Hu, E. L. & Imamoglu, a. *Quantum nature of a strongly coupled single quantum dot-cavity system*. *Nature* **445**, 896–9 (Mar. 2007).
113. Dal Negro, L. & Boriskina, S. *Deterministic aperiodic nanostructures for photonics and plasmonics applications*. *Laser & Photonics Reviews* **6**, 178–218 (Apr. 2012).
114. Xavier, J., Probst, J., Back, F., Wyss, P., Eisenhauer, D., Löchel, B., Rudigier-Voigt, E. & Becker, C. *Quasicrystalline-structured light harvesting nanophotonic silicon films on nanoimprinted glass for ultra-thin photovoltaics*. *Optical Materials Express* **4**, 2290 (Nov. 2014).
115. Xavier, J., Probst, J. & Becker, C. *Deterministic composite nanophotonic lattices in large area for broadband applications*. *Scientific Reports* **6**, 38744 (Dec. 2016).
116. Stiles, P. L., Dieringer, J. A., Shah, N. C. & Van Duyne, R. P. *Surface-Enhanced Raman Spectroscopy*. *Annual Review of Analytical Chemistry* **1**, 601–626 (2008).
117. Wu, M., Congreve, D. N., Wilson, M. W. B., Jean, J., Geva, N., Welborn, M., Van Voorhis, T., Bulović, V., Bawendi, M. G. & Baldo, M. A. *Solid-state infrared-to-visible upconversion sensitized by colloidal nanocrystals*. *Nature Photonics* **10**, 31–34 (2015).
118. Wu, T. C., Congreve, D. N. & Baldo, M. A. *Solid state photon upconversion utilizing thermally activated delayed fluorescence molecules as triplet sensitizer*. *Applied Physics Letters* **107** (2015).
119. Le, K. Q. & John, S. *Synergistic plasmonic and photonic crystal light-trapping: Architectures for optical up-conversion in thin-film solar cells*. *Optics Express* **22**, A1 (Jan. 2014).

List of Figures

1	Artistic illustration of excitation enhancement.	3
2	Illustration of the electromagnetic scattering problem.	10
3	Sketch of a photonic crystal slab and the two limiting cases: the dielectric slab waveguide and the 2D photonic crystal.	13
4	Symmetry properties of the hexagonal lattice.	20
5	Example of a band structure for a photonic crystal slab with hexagonal lattice.	23
6	Clustering of the iris data set.	29
7	Silhouette coefficients of the iris data k -means clustering.	37
8	Illustration of the finite element method principle.	43
9	Overview of the nanohole system's geometry and exemplary meshes.	49
10	Refractive index properties of silicon.	55
11	Lead sulfide (PbS) quantum dots and their absorption and fluorescence.	57
12	Sketch of the measurement configuration for the angular- and wavelength-resolved reflectance (angular-resolved reflectance (ARR)) measurements.	59
13	Experimental setup for the fluorescence enhancement measurement.	61
14	Fabrication process based on nanoimprint lithography (NIL).	62
15	Computational setup of the Fresnel refraction simulation.	67
16	Example meshes for the Fresnel refraction simulation as a function of the SLC/ λ -ratio.	69
17	Convergence study of the Fresnel refraction simulation.	70
18	Computational setup of the Mie scattering simulation.	71
19	Example meshes for the Mie scattering simulation as a function of SLC/ λ -ratio and circle refinements RAC.	74
20	Convergence study results of the Mie refraction simulation.	76
21	Calculated efficiencies and relative deviations using the performance optimized configuration.	78
22	3D Example meshes for the nanohole array simulation as a function of SLC/ λ -ratio, circle refinements RAC and maximum z-ratio.	80
23	Convergence study results of the nanohole array simulation.	82
24	Angle scan results for the nanohole system near a peak.	85
25	Overview of the sample geometry used for the anticrossing experiment and the considered numerical model.	89

26	Overview of experimental and numerical reflectance maps, and numerical field energy enhancement maps for the silicon PhC slab on glass.	91
27	Selected magnetic field strength distributions in the xy -plane.	93
28	Overview of the sample used for the fluorescence enhancement experiment.	96
29	Comparison of experimental and numerical reflectance of the photonic crystal without quantum dot coating.	98
30	Comparison of measured quantum dot fluorescence enhancement F_+ and simulated field energy enhancement E_+	100
31	Comparison of field energy enhancement E_+ and classification maps for the symmetric and asymmetric cases.	111
32	Silhouette analysis plots for the fitting and prediction steps of the symmetric case, and for the asymmetric case.	114
33	Magnetic field prototypes on the xy -plane obtained from the cluster centers.	116
34	Clustering results for the fluorescence enhancement experiment.	118
35	Silhouette analysis plots for the different direction/polarization combinations.	118
36	Prototype map for $\Gamma - K$, TM.	121
37	Prototype map for $\Gamma - K$, TE.	122
38	Prototype map for $\Gamma - M$, TM.	123
39	Prototype map for $\Gamma - M$, TE.	124
40	Full-3D volume renderings of selected modes for the $\Gamma - K$, TE case. . .	128
41	Examples for nanohole arrangements in silicon photonic crystal slabs. . .	136
42	Sketch of a possible photonic crystal enhanced upconversion system. . .	137

List of Acronyms

- ARR** angular-resolved reflectance 58, 59, 87, 90, 91, 151
- CC** cluster center 120
- FDTD** finite-difference time-domain 41
- FEM** finite element method 5, 6, 39, 40, 42–47, 49–52, 54, 78, 88–90, 92, 96, 98, 107, 130, 133, 134, 137
- FWHM** full width at half-maximum 103, 104
- GMM** Gaussian mixture model 33–35, 117, 119, 120, 131
- IMF** index-matching fluid 87, 89
- LED** light-emitting diode 2, 26, 96
- MPB** MIT Photonic Bands 23, 40
- NIL** nanoimprint lithography 55, 62, 88
- OA** oleic acid 56, 58, 97, 99, 101, 102, 104
- PbS** lead sulfide 54, 56–58, 60, 95–97, 99, 101, 102, 136, 151
- PhC** photonic crystal 7, 12–27, 30, 31, 39, 47, 48, 50, 53–56, 58, 60–63, 78, 80, 87–90, 92, 94–97, 99, 101, 102, 105, 107, 108, 119, 125, 126, 130, 131, 133–137
- PML** perfectly matched layer 44, 67, 71
- PVD** physical vapor deposition 62
- QD** quantum dot 39, 54, 56–58, 60, 61, 95–97, 99, 101, 102, 105, 107, 125–128, 133–137
- RAC** refine all circle 50, 73, 74, 76, 77, 80, 82, 84
- RAM** random-access memory 81, 82
- RCWA** rigorous coupled-wave analysis 41, 42
- SEM** scanning electron microscopy 88, 89, 97, 98
- Si** silicon 55
- SLC** side length constraint 50, 68
- TE** transverse-electric 23, 24, 51, 59, 60, 68, 92, 97–99, 101, 102, 104
- TM** transverse-magnetic 23, 24, 51, 59, 60, 68, 90, 92, 97–99, 102, 104
- TTA** triplet–triplet annihilation 136, 137